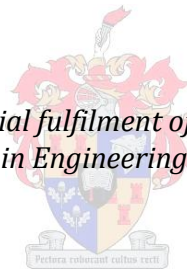


Autonomous Landing of a Fixed-Wing Unmanned Aerial Vehicle using Differential GPS

by
Samuel Jacobus Adriaan Smit

*Thesis presented in partial fulfilment of the requirements for the
degree Master of Science in Engineering at Stellenbosch University*



Supervisor: Mr JAA Engelbrecht
Department of Electrical & Electronic Engineering

March 2013

DECLARATION

By submitting this thesis electronically, I declare that the entirety of the work contained therein is my own, original work, that I am the sole author thereof (save to the extent explicitly otherwise stated), that reproduction and publication thereof by Stellenbosch University will not infringe any third party rights and that I have not previously in its entirety or in part submitted it for obtaining any qualification.

March 2013

Copyright © 2013 Stellenbosch University

All rights reserved

ABSTRACT

This dissertation presents the design and practical demonstration of a flight control system (FCS) that is capable of autonomously landing a fixed-wing, unmanned aerial vehicle (UAV) on a stationary platform aided by a high-precision differential global positioning system. This project forms part of on-going research with the end goal of landing a fixed-wing UAV on a moving platform (for example a ship's deck) in windy conditions.

The main aim of this project is to be able to land the UAV autonomously, safely and accurately on the runway. To this end, an airframe was selected and equipped with an avionics payload. The equipped airframe's stability derivatives were analysed via AVL and the moment of inertia was determined by the double pendulum method. The aircraft model was developed in such a way that the specific force and moment model (high bandwidth) is split from the point-mass dynamics of the aircraft (low bandwidth) [1]. The advantage of modelling the aircraft according to this unique method, results in a design that has simple decoupled linear controllers. The inner-loop controllers control the high-bandwidth specific accelerations and roll-rate, while the outer-loop controllers control the low-bandwidth point-mass dynamics.

The performance of the developed auto-landing flight control system was tested in software-in-the-loop (SIL) and hardware-in-the-loop (HIL) simulations. A Monte Carlo non-linear landing simulation analysis showed that the FCS is expected to land the aircraft 95% of the time within a circle with a diameter of 1.5 *m*. Practical flight tests verified the theoretical results of the developed controllers and the project was concluded with five autonomous landings. The aircraft landed within a circle with a 7.5 *m* radius with the aiming point at the centre of the circle. In the practical landings the longitudinal landing error dominated the landing performance of the autonomous landing system. The large longitudinal error resulted from a climb rate bias on the estimated climb rate and a shallow landing glide slope.

OPSOMMING

Hierdie skripsie stel die ontwikkeling en praktiese demonstrasie van 'n self-landdende onbemande vastevlerkvliegtuigstelsel voor, wat op 'n stilstaande platform te lande kan kom met behulp van 'n uiters akkurate globale posisionering stelsel. Die projek maak deel uit van 'n groter projek, waarvan die doel is om 'n onbemande vastevlerkvliegtuig op 'n bewegende platform te laat land (bv. op 'n boot se dek) in onstuimige windtoestande.

Die hoofdoel van die projek was om die vliegtuig so akkuraat as moontlik op die aanloopbaan te laat land. 'n Vliegtuigraamwerk is vir dié doel gekies wat met gepaste avionica uitgerus is. Die uitgeruste vliegtuig se aerodinamiese eienskappe was geanaliseer met AVL en die traagheidsmoment is deur die dubbelependulum metode bepaal. Die vliegtuigmodel is op so 'n manier ontwikkel om [1] die spesifieke krag en momentmodel (vinnige reaksie) te skei van die puntmassadinamiek (stadige reaksie). Die voordeel van hierdie wyse van modulering is dat eenvoudige ontkoppelde beheerders ontwerp kon word. Die binnelusbeheerders beheer die vinnige reaksie-spesifieke versnellings en die rol tempo van die vliegtuig. Die buitelusbeheerders beheer die stadige reaksie puntmassa dinamiek.

Die vliegbeheerstelsel is in sagteware-in-die-lus en hardeware-in-die-lus simulاسies getoets. Die vliegtuig se landingseienskappe is ondersoek deur die uitvoer van Monte Carlo simulاسies, die simulاسie resultate wys dat die vliegtuig 95% van die tyd binne in 'n sirkel met 'n diameter van 1.5 m geland het. Praktiese vlugtoetse het bevestig dat die teoretiese uitslae en die prakties uitslae ooreenstem. Die vliegtuig het twee suksesvolle outomatiese landings uitgevoer, waar dit binne 'n 7.5 m-radius sirkel geland het, waarvan die gewenste landingspunt die middelpunt was. In die outomatiese landings is die longitudinale landingsfout die grootse. Die groot longitudinale landingsfout is as gevolg van 'n afset op die afgeskatte afwaartse spoed en 'n lae landings gradiënt.

ACKNOWLEDGEMENTS

I would like to extend my gratitude to the following people for their support and guidance in making this project possible:

- Japie Engelbrecht: for your patience, guidance, ideas on how to solve problems and attending of flight tests. Your input to this project and the life lessons I learned from you are much appreciated.
- The Stellenbosch miracle workers at SED: Wessel Croukamp, Wynand van Eeden, Lincoln Saunders and Johan Arendse.
- To all of my friends in the ESL, especially: Rudi Gaum and Ruan de Hart for their time in supporting me in various aspects of this project, AM de Jager and Lionel Basson for assistance in flight tests, ideas and a ton of absurdity, Chris Jaquet for his company during late hours and a helping hand, and lastly but certainly not least, my office mate Konrad Friedrich, for more ridiculous humour and support from the beginning of this project to the end.
- Helderberg Radio Flyers Club (HRF) for the use of their airfield and especially to Michael Basson, our safety pilot, for looking after the aircraft during the flight tests.
- My family for their love and support over the long distance.
- My beautiful girlfriend Jessica Bolleurs, for all your love and support over an even longer distance during the course of this project.

TABLE OF CONTENTS

Declaration	ii
Abstract	iii
Opsomming	iv
Acknowledgements	v
Table of Contents	vi
List of Figures	xiii
List of Tables	xvii
Nomenclature	xviii
<i>Chapter 1.....</i>	<i>1</i>
Introduction.....	1
1.1 Overview	1
1.2 Background	2
1.3 Project Goals	3
1.4 Literature Study	3
1.5 Dissertation Layout.....	5
<i>Chapter 2.....</i>	<i>7</i>
Project Overview	7
2.1 Autonomous Landing System.....	7
2.2 Strategy for Autonomous Landing	8
2.2.1 Flight Control Architecture	8

2.2.2 Landing Trajectory.....	10
2.3 Project Execution	11
<i>Chapter 3</i>	<i>13</i>
Aircraft Modelling and Simulation.....	13
3.1 Axis System Definitions and Notations	13
3.1.1 Inertial Axes	13
3.1.2 Fixed Body Axes.....	14
3.1.3 Wind Axes.....	15
3.2 Aircraft Model Overview	16
3.3 Outer-Loop Model: Point-Mass Kinematics.....	17
3.3.1 Point-Mass Dynamics	17
3.3.2 Attitude Dynamics.....	19
3.4 Inner-Loop Model: Kinetics	20
3.4.1 Rigid-Body Rotational Dynamics.....	20
3.4.2 Specific Forces and Moments	22
3.4.2.1 Thrust Model.....	23
3.4.2.2 Aerodynamic Model	23
3.5 Summary	25
<i>Chapter 4</i>	<i>26</i>
Inner-Loop Controllers	26
4.1 Simplifying and Decoupling the Aircraft Model.....	26
4.2 Normal Specific Acceleration Controller	28
4.2.1 Design	29
4.2.2 Pole-Placement and Simulation.....	32

4.2.3 Effect of Flaps on the Closed-Loop Normal Specific Acceleration Dynamics.....	35
4.2.4 Normal Specific Acceleration Controller Practical Flight Test	36
4.2.4.1 Normal Specific Acceleration Step Response Test	36
4.2.4.2 Implicitly Testing the Normal Specific Acceleration Controller	38
4.3 Decoupling of Lateral Dynamics.....	39
4.4 Roll-Rate Controller	40
4.4.1 Design	40
4.4.2 Pole-Placement and Simulation.....	42
4.4.3 Roll-Rate Controller Practical Flight Test.....	43
4.5 Lateral Stability Augmentation Controller	44
4.5.1 Dutch Roll Damper Design	45
4.5.2 Lateral Specific Acceleration Controller Design	47
4.5.3 Lateral Stability Augmentation Controller Summary.....	50
4.5.4 Lateral Stability Augmentation Controller Practical Flight Test	51
4.5.4.1 Dutch Roll Damper Flight Test.....	51
4.5.4.2 Lateral Specific Acceleration Regulator Test	53
4.6 Review of the Inner-Loop Controllers.....	54
4.7 Summary	55
<i>Chapter 5.....</i>	<i>56</i>
Outer-Loop Flight Control System	56
5.1 Longitudinal Control Architecture.....	56
5.1.1 Airspeed and Climb-Rate Controller.....	56
5.1.1.1 Linear Quadratic Regulator Design	60
5.1.2 Altitude Controller.....	63

5.1.3 Airspeed Climb-Rate Controller Practical Flight Test.....	64
5.1.4 Airspeed Altitude Controller Practical Flight Test.....	66
5.2 Lateral Control Architecture.....	67
5.2.1 Normal Specific Acceleration Vector Direction Controller.....	69
5.2.2 Guidance Controller.....	70
5.2.3 Pole-Placement and Simulation.....	72
5.2.4 Guidance Controller and NSAVDC Practical Flight Test.....	75
5.3 Summary.....	75
<i>Chapter 6</i>	<i>77</i>
Hardware and Software.....	77
6.1 Airframe.....	77
6.2 Avionics.....	79
6.2.1 Avionics Box.....	80
6.2.2 On-Board Computer.....	81
6.2.3 Inertial Measurement Unit.....	83
6.2.4 GPS Module.....	83
6.2.5 Radio Frequency Communication Module.....	84
6.2.6 Pressure/Magnetometer Printed Circuit Board.....	84
6.2.7 Power Distribution.....	85
6.3 Ground Station.....	86
6.3.1 Ground Station Application.....	87
6.3.2 Landing and Navigation Setup (L and N Setup Tab).....	90
6.3.3 Estimator.....	91
6.3.4 Sensors Tab.....	92

6.3.5 Actuators, Actuator Setup and Diagnostics Tab	93
6.4 Summary	93
<i>Chapter 7</i>	<i>94</i>
Landing System Design.....	94
7.1 Autonomous Landing Strategy.....	94
7.2 Landing State Machine	96
7.3 Summary	102
<i>Chapter 8</i>	<i>103</i>
Non-Linear Landing Simulation.....	103
8.1 Overview of Simulation Environment.....	103
8.1.1 Software-in-the-Loop Simulation	103
8.1.2 Hardware-in-the-Loop Simulation.....	104
8.2 Non-Linear Landing Simulation	106
8.2.1 Ideal Non-Linear Landing Simulation.....	108
8.2.2 Constant Wind: Non-Linear Landing Simulation.....	112
8.2.3 Wind Gust: Non-Linear Landing Simulation	115
8.2.4 Windless day Landing Simulation	118
8.3 Summary	120
<i>Chapter 9</i>	<i>121</i>
Practical Flight Tests.....	121
9.1 System Identification	121
9.1.1 Stall Speed	121
9.1.2 Touchdown.....	122
9.1.3 First and Second Glide Slope.....	124

9.2 Autonomous Landing.....	124
9.2.1 Interpretation of Measured Landing Data	125
9.2.2 Airspeed and Climb Rate.....	126
9.2.3 Landing Accuracy.....	127
9.2.3.1 Climb-Rate Bias	131
9.2.3.2 Wind Condition	134
9.2.3.3 Ground effect.....	136
9.2.3.4 Origin of the Climb-Rate Bias	136
9.3 Summary	136
<i>Chapter 10.....</i>	<i>138</i>
Conclusion and Recommendations	138
10.1 Summary	138
10.2 Conclusion.....	139
10.3 Recommendations.....	140
<i>Appendix A</i>	<i>A-1</i>
Aircraft Specifications and Modelling.....	A-1
A.1 Physical Specifications	A-1
A.1.1 Aircraft’s Weight Budget	A-1
A.1.2 Moment of Inertia.....	A-2
A.1.3 Engine Thrust	A-3
A.2 Modelling Constants	A-3
A.2.1 Air Density	A-3
A.2.2 Gravitational Acceleration.....	A-3
A.3 Aerodynamic Model	A-3

A.3.1 Airfoil Specifications.....	A-3
A.3.2 Aircraft Trim Airspeed.....	A-4
A.3.3 Non-Dimensional Stability and Control Derivatives	A-4
A.3.4 Dimensional Stability and Control Derivatives Notation.....	A-6
<i>Appendix B</i>	<i>B-1</i>
Attitude Representation	B-1
B.1 Euler Angles	B-1
Bibliography	xxii

LIST OF FIGURES

Figure 1.1 Dissertation Layout	6
Figure 2.1 Autonomous Landing System Overview	7
Figure 2.2 Control System Block Diagram	9
Figure 2.3 Longitudinal Landing Path	10
Figure 2.4 Lateral Landing Path	11
Figure 3.1 Inertial Axis System [22]	14
Figure 3.2 Fixed Body Axis System [23]	14
Figure 3.3 Wind Axes [23]	15
Figure 3.4 Polar Velocity Coordinates	16
Figure 3.5 Aircraft Model Overview [1]	17
Figure 4.1 Open-Loop Pole-Zero Map of NSA Dynamics with Step Responses	30
Figure 4.2 Pole-Zero Map of the NSA Dynamics over the Velocity Range of Interest.....	33
Figure 4.3 Allowable Pole-Placement Region for the Closed-Loop NSA Dynamics	34
Figure 4.4 NSA HIL Simulation Non-Linear Step Response at 18 m/s	35
Figure 4.5 NSA Practical Step Response for the Clean Configuration	37
Figure 4.6 NSA Practical Step Response for the Flap Configuration	38
Figure 4.7 Outer-Loop and Normal Specific Acceleration Controller Practical Test Results	39
Figure 4.8 Roll-Rate Controller Linear Step Response at Trim Airspeed.....	42
Figure 4.9 Roll-Rate Controller Practical Test Result	43
Figure 4.10 Overview of the Lateral Stability Augmentation Control Architecture	44
Figure 4.11 Dutch Roll Damper Root Locus Design.....	46

Figure 4.12 Improved Damping of the Dutch Roll Mode.....	47
Figure 4.13 Aircraft Lateral Dynamics	48
Figure 4.14 Lateral Stability Augmentation Controller Response to a Step Disturbance.....	50
Figure 4.15 Open-Loop Practical Response of the Dutch Roll Mode	52
Figure 4.16 Closed-Loop Practical Response of the Dutch Roll Damper.....	52
Figure 4.17 Practical Unstable Response of the Lateral Specific Acceleration Regulator	53
Figure 4.18 Block Diagram Overview of the Flight Control System.....	55
Figure 5.1 Airspeed & Climb-Rate Controller.....	57
Figure 5.2 Airspeed Climb-Rate Controller Linear Step Responses	62
Figure 5.3 Airspeed Climb-Rate Controller Close-Loop Pole Locations at Trim Airspeed	62
Figure 5.4 Altitude Controller Block Diagram.....	63
Figure 5.5 Altitude Controller Design	64
Figure 5.6 Practical Airspeed Step Responses.....	66
Figure 5.7 Altitude and Airspeed Controller Practical Flight Test Result	67
Figure 5.8 Specific Acceleration Command Conversion from Inertial to Wind Axes.....	68
Figure 5.9 Park's Lateral Guidance Controller [21]	71
Figure 5.10 Linearising the Non-Linear Guidance Law [21]	71
Figure 5.11 NSAVDC Non-Linear Step Response.....	73
Figure 5.12 Lateral Position Step Response of the Guidance Controller	74
Figure 5.13 Lateral Control System Closed-Loop Pole Locations at Trim Airspeed	74
Figure 5.14 Guidance Controller and NSAVDC Practical Flight Test Results	76
Figure 6.1 The Airframe on Arrival from Banitz Hobbies.....	78
Figure 6.2 The Equipped Airframe on a Flight Test Day.....	78
Figure 6.3 Avionics and Ground Station Block Diagram Overview.....	79

Figure 6.4 Avionics Box Side View and Avionics.....	80
Figure 6.5 Avionics Box Mounted inside the Aircraft	81
Figure 6.6 OBC Software Routine [ESL]	82
Figure 6.7 Photograph of the Pressure/Magnetometer PCB Installed in the Wing	85
Figure 6.8 Ground Station Objects and Data Flow [ESL].....	87
Figure 6.9 Ground Station Application with Controller Tab Open	88
Figure 6.10 Controller Tab	89
Figure 6.11 L and N Setup Tab	90
Figure 6.12 Estimator Tab	91
Figure 6.13 Sensors Tab	92
Figure 6.14 Photo of the Aircraft and Ground Station after a Flight Test at HRF	93
Figure 7.1 Stabilised Landing Approach [30].....	96
Figure 7.2 Conventional Landing Pattern [30]	97
Figure 7.3 Landing Phases Flow	97
Figure 7.4 Detailed Longitudinal Landing Path	99
Figure 7.5 Lateral Landing Path	100
Figure 7.6 Landing State Machine	102
Figure 8.1 Non-Linear Simulation Environment.....	104
Figure 8.2 Hardware-in-the-Loop Setup Overview	106
Figure 8.3 Landing Transition Phases	108
Figure 8.4 Landing Phases.....	109
Figure 8.5 Aircraft Landing States.....	110
Figure 8.6 Landing Point Shift due to an Error in Altitude.....	111
Figure 8.7 Headwind During Landing	113

Figure 8.8 Tailwind During Landing	114
Figure 8.9 Tailwind Gust.....	116
Figure 8.10 Headwind Gust.....	117
Figure 8.11 Simulated Touchdown Point Landing Spread	120
Figure 9.1 Landing Spikes in the <i>ZB</i> -Axis Accelerometer.....	122
Figure 9.2 Measured Longitudinal Landing States During Actual Autonomous Landing	125
Figure 9.3 Touchdown Spike Measured by the <i>ZB</i> -Axis Accelerometer	126
Figure 9.4 Airspeed and Climb Rate during the Landing Approach	127
Figure 9.5 Practical Landing Altitude States on the Second Glide Slope.....	128
Figure 9.6 Practical Landing Climb Rate States Seconds before Touchdown	129
Figure 9.7 Practical Virtual Deck Landing Test	130
Figure 9.8 Virtual Deck Landing Airspeed and Climb-Rate States on the Second Glide Slope.....	131
Figure 9.9 Simulated Landing with a Climb-Rate Bias.....	132
Figure 9.10 Simulated Landing Seconds before Touchdown	133
Figure 9.11 Measured Longitudinal Landing States during Second Autonomous Landing.....	135
Figure 9.12 Second Autonomous Landing Airspeed and Climb-Rate States on the Second Glide Slope	135
Figure A.1 Moment of Inertia Measurement Setup	A-2
Figure A.2 AVL Geometry Plot of the Aircraft	A-5

LIST OF TABLES

Table 4.1 Longitudinal Stability Derivative's for the Aircraft in Clean and Flap Configuration	35
Table 7.1 Landing Parameters	100
Table 8.1 Windless Day: Sensor Noise Characteristics and Wind Effects	119
Table A.1: Aircraft Weight Budget	A-1
Table A.2 Measured Moment of Inertia	A-2
Table A.3 Airfoil Properties	A-3
Table A.4 Stability Derivatives for the Aircraft in Clean Configuration	A-5
Table A.5 Control Derivatives	A-6
Table A.6 Dimensional Stability and Control Derivatives (Forces)	A-6
Table A.7 Dimensional Stability and Control Derivatives (Moments)	A-7

NOMENCLATURE

Vectors and Matrixes

P, V, A	Position, Velocity and Acceleration vectors
F, M	Force and Moment vectors
H	Angular momentum vector
ω	Angular rate vector
DCM, S, T, I_B	Direction cosine matrix, cross product matrix, transformation matrix and moment of inertia matrix
K	Feedback gain matrix
Q, R	State-weighting matrix and actuator-weighting matrix

Subscripts and Superscripts

I_C^{AB}	Denotes vector I coordinated in axis system C with data about axis system A relative to B
I, B, W, R	Wind, inertial, body and reference axis system

Coordinate Vectors

A, B, C	Specific accelerations in the X, Y and Z-axis directions in the subscripted axis system
X, Y, Z	X, Y and Z-axis forces in the subscripted axis system
L, M, N	Roll, pitch and yaw moments in the subscripted axis system

P, Q, R	Roll, pitch and yaw rates in the subscripted axis system
ϕ, θ, ψ	Roll error angle, pitch and yaw angles
\bar{V}, α, β	Velocity magnitude, angle of attack and angle of sideslip
I_{xx}, I_{yy}, I_{zz}	Principal moments of inertial about the X, Y and Z-axes
P_x, P_y, P_z	Position coordinates in the inertial axis system

Aerodynamic Modelling Symbols

b	Wing span
c	Mean aerodynamic chord
S	Surface area
A	Aspect ratio
e	Efficiency
L, D, R_{LD}	Lift, drag and lift-to-drag ratio
m, I_Q	Mass moment of inertia parameter.
g	Gravitational acceleration
ρ	Air pressure
\bar{V}	Airspeed
T, T_C	Trust and commanded thrust
$\delta_A, \delta_E, \delta_R, \delta_F$	Aileron, elevator, rudder and flap control deflections

Aerodynamic Coefficients

C_{L0}, C_{m0}	Static lift and pitching moment coefficients
C_L, C_D, C_y	Aerodynamic lift, drag and side force coefficients

C_l, C_m, C_y Aerodynamic roll, pitch and yaw moment coefficients

Control

p, z Poles and zeros

ω_n, ζ, τ Natural frequency, damping and time constant

$K_{(\cdot)}$ Feedback gain

J Cost function

Abbreviations

ABC Acceleration-based flight control

ADC Analogue to digital converter

ATOL Automatic take-off and landing

AVL Athena vortex lattice

FCS Flight control system

DGPS Differential global position system

DCM Direction cosine matrix

DRD Dutch roll damper

DOF Degree of freedom

ECS Electronic speed controller

ESL Electronic systems laboratory

CG Centre of gravity

GUI Graphical user interface

GPS Global positioning system

IMU	Inertial measurement unit
LSA	Lateral specific acceleration
LQR	Linear quadratic regulator
MIMO	Multi-input, multi-output
MOI	Moment of inertia
NMP	Non-minimum phase
NSA	Normal specific acceleration
NSAVDC	Normal specific acceleration vector direction controller
OBC	On-board computer
PID	Proportional integral differential
RF	Radio frequency
RC	Remote control
SPM	Short-period mode
SISO	Single-input, single-output
SU	Stellenbosch University
TSS	Time-scale separation
UAV	Unmanned aerial vehicle

Chapter 1

Introduction

1.1 Overview

In today's ever-expanding world of technology, unmanned aerial vehicle (UAV) systems have developed into sophisticated, capable machines. These machines are used by military organisations worldwide for various strike and surveillance missions. UAVs are not limited to military use, however; they also have civil applications over land and sea [2], [3], [4], and [5].

The Predator and Global Hawk UAVs attained immense popularity in military operations in Afghanistan. The Predator UAV comes mainly in two configurations: one is used for surveillance, while the other is used to carry out strike missions [6]. The Global Hawk is used solely for long-distance reconnaissance and information-gathering missions. During the US occupation of Afghanistan, Jeff Schogol reported that the air force lost many more UAVs than the army did, in part because the army drones are capable of landing themselves [7]. The USA military is also expanding its UAV auto-landing capabilities to include carrier-deck landings, the X-47B UAV is scheduled to start practical carrier-deck landing tests in 2013 [8].

In civil applications, UAVs have a very wide range of applications. This is due to the fact that the mission profile of a UAV can easily be adjusted to a specific mission by changing its payload. Equipping a UAV with infrared sensors, for instance, allows the UAV to monitor/report wildfire in forests. Civil applications include, but are not limited to, search and rescue missions, pipeline inspection and border patrol missions. Fixed-wing UAVs can, for example, be used for search and rescue missions because they can cover vast distances very quickly to look for survivors from shipwrecks. Compared to helicopters, however, fixed-wing UAVs are at a disadvantage when returning from such missions since they have to land on the relatively small helipad on a ship's deck. This last part of the UAV's mission is by far the most complex and dangerous. By automating the landing aspect of the UAV, the risk of destroying/damaging the UAV is significantly reduced as noted by [7] in the previous paragraph.

This short introduction highlights the importance of the automated landing capability of UAVs. The project described in this dissertation focuses on developing an autopilot that is capable of autonomously landing a fixed-wing UAV accurately on a stationary platform.

1.2 Background

This project is the third generation of research into autonomous take-off and landing (ATOL) in the Electronic Systems Laboratory (ESL) at Stellenbosch University (SU). In the following paragraphs a brief overview is provided of previous fixed-wing UAV research into ATOL that led to the development of this project.

In 2005 Peddle successfully designed and demonstrated a conventional autopilot for a model aircraft [9]. This project used off-the-shelf components and a standard global positioning system (GPS) and achieved full autonomous navigation in three practical flight tests. In 2007 Roos [10] built on the platform that Peddle had developed. New take-off and landing controllers were designed and implemented. Roos successfully demonstrated autonomous take-off and landing of a fixed-wing UAV on a stationary platform. In the landing phase described in [10], a standard GPS was used to navigate the UAV onto the final approach of the runway, while an ultrasonic range finder was used to determine altitude. This sensor fusion was necessary since the standard GPS altitude measurement was not accurate enough for a safe landing.

In 2008 Peddle submitted his thesis for a Doctorate in Philosophy in engineering, with the title of "Acceleration-based manoeuvre flight control systems for unmanned aerial vehicles" [1]. This work became a cornerstone for many of the projects in the ESL, including this present project. The focus of Visser's master's dissertation [11] on the topic of ATOL is the autonomous precision landing of a UAV by incorporating research from [1] and vision-based sensors. Visser, like Roos, made use of a standard GPS to guide the UAV onto the final approach of the runway. During the landing phase, vision sensors were used to obtain accurate position and altitude data. The camera system relied on beacons that were placed near the landing target to obtain reliable data. The camera system that Visser developed was tested successfully. Unfortunately, a radio frequency (RF) failure on the UAV resulted in the destruction of the vehicle, preventing a successful landing. De Hart [12] used the same aircraft to extend Peddle's research by implementing advanced take-off and control algorithms for fixed-wing UAVs.

After the completion of Visser's project, the ATOL research group at Stellenbosch University decided to take a fresh approach to autonomous landing. The new approach would be less dependent on

the runway for a camera system and would instead rely on high-precision GPS measurements, thus not making use of any special markers on the runway. However, if the landing system were commanded to land on a different runway than the take-off runway, the landing system would require the new runway's heading and altitude, since high-precision GPS zero altitude is based on the initialisation point on the take-off runway. This new approach would also simplify the system's architecture and physical makeup. During landing the system would not have to switch between different sensor systems and fewer modifications would be required on the airframe since there would be no need to accommodate vision sensors.

1.3 Project Goals

The primary goal of this project is to design an autopilot that is capable of landing the UAV accurately. This implies that the aircraft must be capable of entering a desired landing pattern. Thereafter the aircraft will go through different landing phases in order to land accurately. The primary goal is achievable through several sub-goals that are listed below:

- Equip a new airframe with avionics.
- Develop the resulting autonomous vehicle platform hardware in such a way that it can be used as a basis for future projects and also be easily reconfigurable.
- Model the airframe's stability and control derivatives.
- Incorporate a differential GPS into the standard ESL avionics.
- Design the flight control system and verify its performance through flight tests.
- Practically demonstrate the autonomous landing system.

1.4 Literature Study

A survey on autopilot technologies for small fixed wing UAV's is described in [13]: this paper provides a summary of commercial, open source autopilots, as well as autopilots under development. The paper introduces the reader to a basic autopilot system and explains different software and hardware aspects of an autopilot system. This discussion is then followed by a comparison of off-the-shelf autopilot packages in terms of hardware, design strategy and controller strengths. The paper concludes with a consideration of possible future developments in autopilot

systems. A good indication is given of the different autopilot systems on the market, their capabilities and design approaches.

[14] analyses practical landing data of actions performed by a pilot and employs system identification techniques to validate the mathematical model of the aircraft. Based on the analysis of practical landing data, a classical PI altitude controller was designed for the approach and flare phase that minimises the error in altitude from the reference glide slope, based on the aircraft's current position. The landing simulation results show that the aircraft can land in simulation but do not specify the accuracy of the simulated landing. The landing state machine concepts in the mentioned paper provided a good starting basis to design the landing state machine used in this project.

When the aircraft transitions from the glide path to the flare path, the UAV tends to an unstable region [15]. This article investigates the instability that occurs during the change in landing phase. The article formulates a blending function to overcome instability during transition and concludes with simulation results that show a smooth stable transition from the glide slope to flare phase. Implementation of a blending function for a stable transition from glide slope to flare path was considered in this project.

[16] investigates the autonomous landing of a fixed-wing UAV on a ship's deck. This master's dissertation focuses on the communication between the UAV and the ground station and on the design of autonomous landing controllers. The project used fast inner-loop controllers (pitch-rate and roll-rate controllers) based on classical controller design theory and slower outer-loop point-mass controllers. In a HIL landing simulation scenario, the UAV is subjected to various wind and sensor noise characteristics. Under specific wind and sensor noise conditions the HIL simulation showed that the UAV landed with a mean of 0.35 m (after) in the longitudinal and -0.52 m (West) in the lateral direction from the intended touchdown point with a standard deviation of 0.27 m and 0.028 m . The method according to which the simulations were conducted and the design of the inner-loop controllers were of interest.

In [17] a non-linear dynamic inversion control approach is used to achieve autonomous landing of a fixed-wing UAV. In this article the different landing phases are scheduled as a function of the approach distance from the runway. The landing path is designed so that the transition from the glide slope to the flare phase is continuous. The article uses a high-fidelity non-linear six-DOF model which was developed from extensive wind tunnel testing to verify the design of the controllers and landing performance of the autonomous landing system. Simulation results showed that under

different initial conditions the UAV landed within a meter of the longitudinal touchdown point within sink-rate bounds of 0.1 m/s . The glide slope-to-flare-phase transition, different initial condition simulations and the controller design approach were of interest.

In [18] a fully automatic taxiing and take-off and landing UAV system is presented that only uses a single-antenna GPS receiver. In addition to the high precision GPS receiver, only an airspeed sensor is added. The landing system uses LQR controllers for automatic take-off and landing. The article shows via simulation and practical landing tests that a single GPS antenna can be used as a backup or low-cost control system for a UAV. The landing strategy and practical landing data were of interest in terms of the glide slope and distance from the runway that UAV started the autonomous landing process.

1.5 Dissertation Layout

The dissertation layout is shown in Figure 1.1. Chapter 2 presents a high-level system overview by conceptually discussing the autonomous landing system, flight control system architecture and landing trajectory.

Chapter 3 defines the different axis systems and outlines the development of the aircraft model based on rigid-body dynamics and aerodynamic modelling.

The design of the inner-loop controllers is presented in Chapter 4: this design is based on the linear models described in Chapter 3. Chapter 5 explains the designing of the outer-loop controllers, based on the inner-loop controllers via a successive loop closure strategy. Non-linear simulations and practical flight test results are presented after the theoretical design for each controller in Chapter 4 and Chapter 5.

Chapter 6 discusses the hardware and software of the autonomous landing system. The chapter is divided into three main sections namely the airframe, avionics and ground station.

Chapter 7 presents the autonomous landing strategy, landing trajectory and the different landing phases as well as the transition conditions between them, and concludes with a detailed landing state machine.

Chapter 8 starts with an overview of the simulation environment. The landing performance of the FCS and the control actions that the FCS executes are thoroughly evaluated under different wind conditions in the simulation environment. With a simulated statistical indication of the system's

auto-landing performance, the system is tested in the real world. The flight test results are presented and analysed in Chapter 9. The dissertation concludes in Chapter 10.

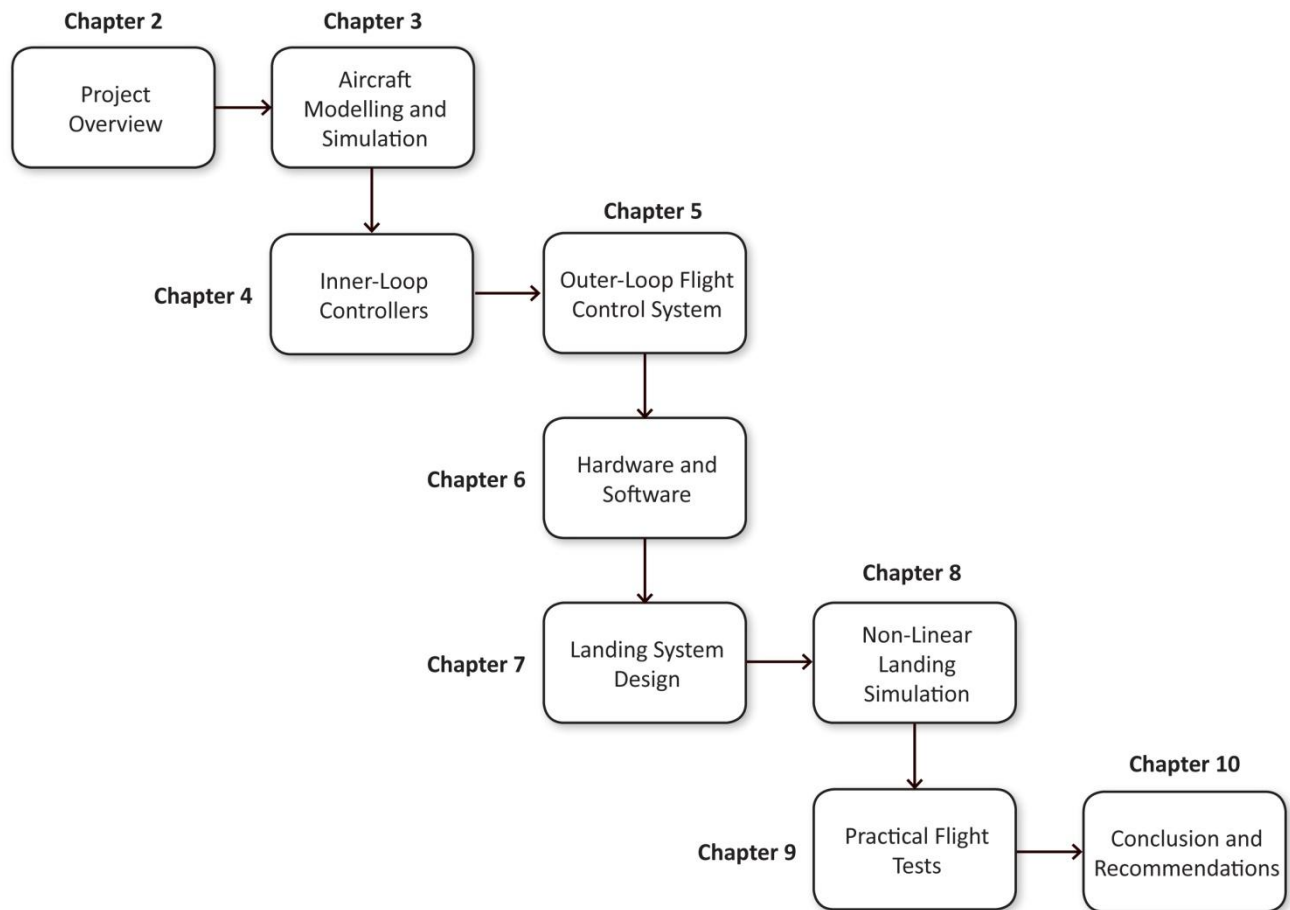


Figure 1.1 Dissertation Layout

Chapter 2

Project Overview

This chapter aims to provide the reader with a theoretical map of the project. A high-level block diagram of the autonomous landing system is discussed in Section 2.1. In Section 2.2 the strategy of autonomous landing is discussed by giving an overview of the flight control system architecture and landing trajectories. Section 2.3 concludes the chapter with a brief look at some of the bigger challenges encountered during this project.

2.1 Autonomous Landing System

The diagram in Figure 2.1 gives an overview of the autonomous landing system. The landing system consists of three components: the aircraft, the ground station and the avionics.

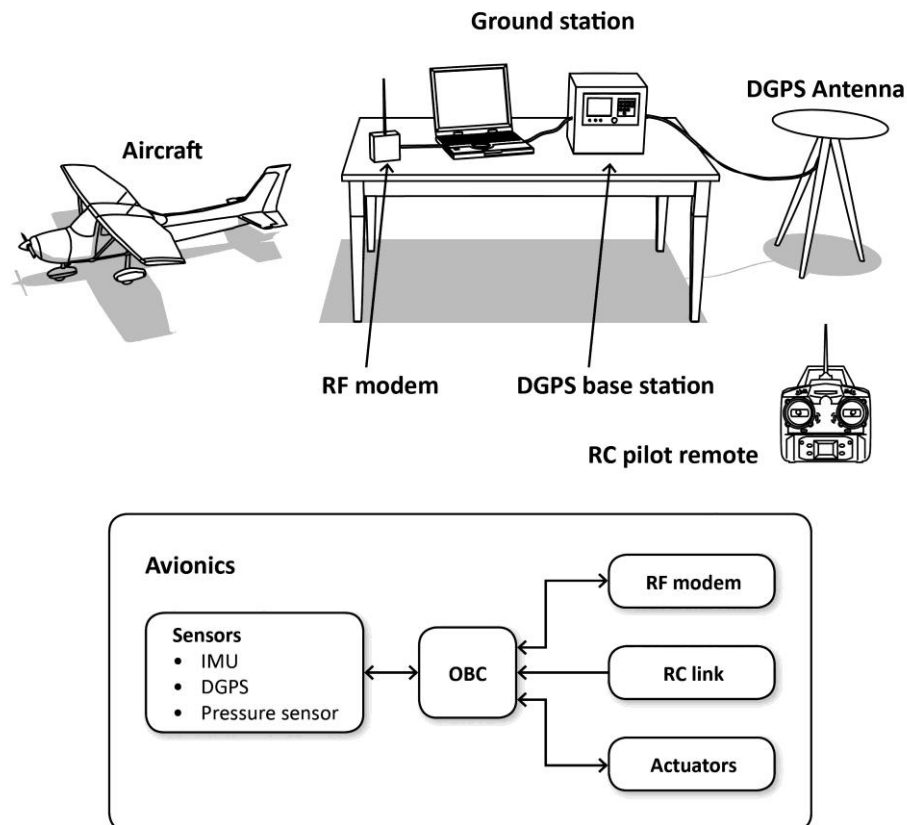


Figure 2.1 Autonomous Landing System Overview

The airframe is a modified Phoenix trainer 60 equipped with an avionics payload that consists of an on board computer (OBC), inertial measurement unit (IMU), DGPS, radio frequency (RF) modem, remote control (RC) receiver and a pressure sensor (airspeed and altitude). The ground station consists of a laptop, DGPS base station, RF modem and an RC transmitter. The laptop runs the ground station software and interfaces with the aircraft via the RF modem. From the ground station various controller commands and landing parameters can be updated on the OBC during flight.

2.2 Strategy for Autonomous Landing

2.2.1 Flight Control Architecture

The acceleration based flight control (ABC) architecture [1] and all the latest software and hardware developed in the ESL were incorporated into the reconfigurable aircraft project (the Meraka project). This project provides an excellent starting base since it provides a complete non-linear simulation environment and flight-tested OBC code. The software from the Meraka project was reused and the flight control system was modified for the specific airframe.

In autonomous landing, high demands are placed on the ability of the FCS to regulate the airspeed, altitude and lateral track. From the results of previous projects in the ESL ([19], [20], [12], [11]) that used the acceleration based control (ABC) architecture, it was found that the architecture yielded good results in regulating the position, velocity and acceleration of the aircraft. These results gave a good indication that the ABC architecture in conjunction with the landing command reference generator would be able to land the aircraft safely. Additionally, the ABC architecture provides an easy interface to the landing command reference generator that generates high-level references for airspeed, altitude and lateral track. These high-level commands are then translated by the ABC architecture to lower level control deflections.

The flight control system block diagram is illustrated below in Figure 2.2. The block diagram is colour-coded and analysed using a bottom-up strategy. The blue blocks represent the lowest level of control, the orange block represents the middle-loop controller and the green blocks represent the top level of control.

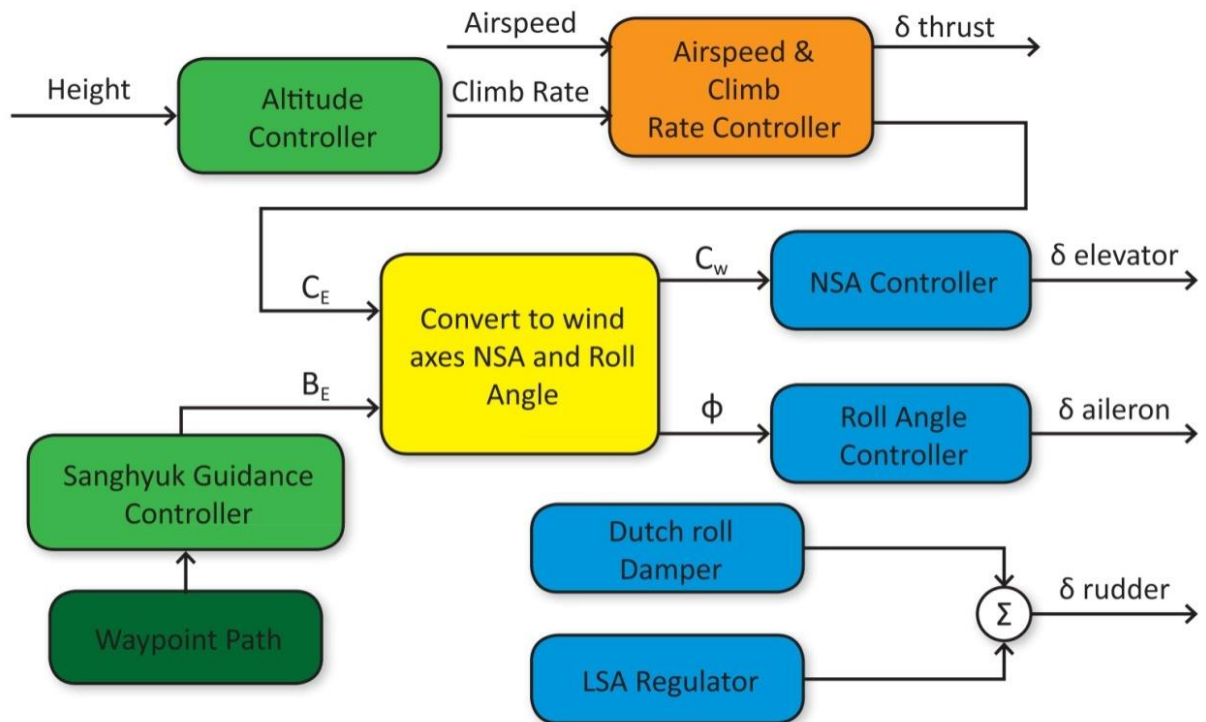


Figure 2.2 Control System Block Diagram

The *Normal Specific Acceleration* (NSA) Controller acts as a virtual actuator that translates a normal specific acceleration command into an elevator command, i.e. if a normal acceleration command of -9.81 m/s^2 were issued the aircraft would generate enough lift on the main wing to fly level.

The *Roll Angle Controller* (*Normal Specific Acceleration Vector Direction Controller*) steers the normal acceleration vector by directing the main wing's lift vector via the ailerons.

The *Dutch Roll Damper* and *Lateral Specific Acceleration* (LSA) regulator augments the lateral stability by using the aircraft's rudder. The *Dutch Roll Damper* increases the aircraft's Dutch roll damping and the LSA regulator aids in coordinating the aircraft's turns.

At the yellow block, the commanded horizontal (B_E) and vertical (C_E) specific accelerations in the inertial axis are converted to wind axis normal specific acceleration and roll-angle commands.

The *Airspeed and Climb Rate Controller* is a MIMO LQR strategy that generates thrust and normal specific acceleration commands (C_E) from an airspeed and climb-rate reference.

The *Altitude Controller* is a proportional feedback controller that multiplies a feedback gain with an altitude error signal to generate a climb-rate command.

A *Guidance Controller* developed by Dr Sanghyuk Park [21] is used in this project to guide the aircraft on the landing circuit. The guidance controller guides the aircraft onto the path by generating a lateral specific acceleration (B_E) that translates into a reference roll-angle that steers the aircraft's lift vector via the ailerons.

2.2.2 Landing Trajectory

The longitudinal landing and lateral landing trajectories are illustrated in Figure 2.3 and Figure 2.4 respectively. The longitudinal landing trajectory is based on a stabilised landing approach and the lateral landing trajectory is based on a conventional landing pattern.

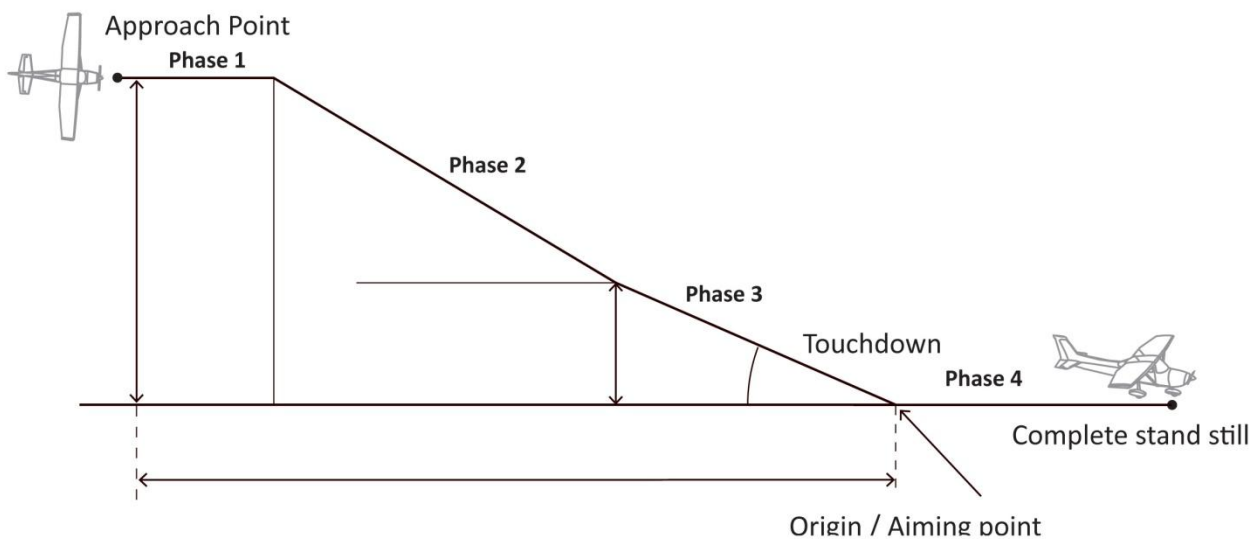


Figure 2.3 Longitudinal Landing Path

The longitudinal landing trajectory consists of four phases. During Phase 1 the FCS regulates the aircraft's states (airspeed, altitude and lateral track) to predetermined values in preparation to descend on the first glide path and extends the flaps. In Phase 2 the FCS captures the first glide path and starts its constant descent by controlling the altitude based on distance from the touchdown point (downrange). In Phase 3, similar to Phase 2, the FCS captures the second glide path and prepares the aircraft for touchdown at the end of Phase 3. On touchdown, the start of Phase 4, the safety pilot retakes control for the ground roll until the aircraft comes to a complete standstill.

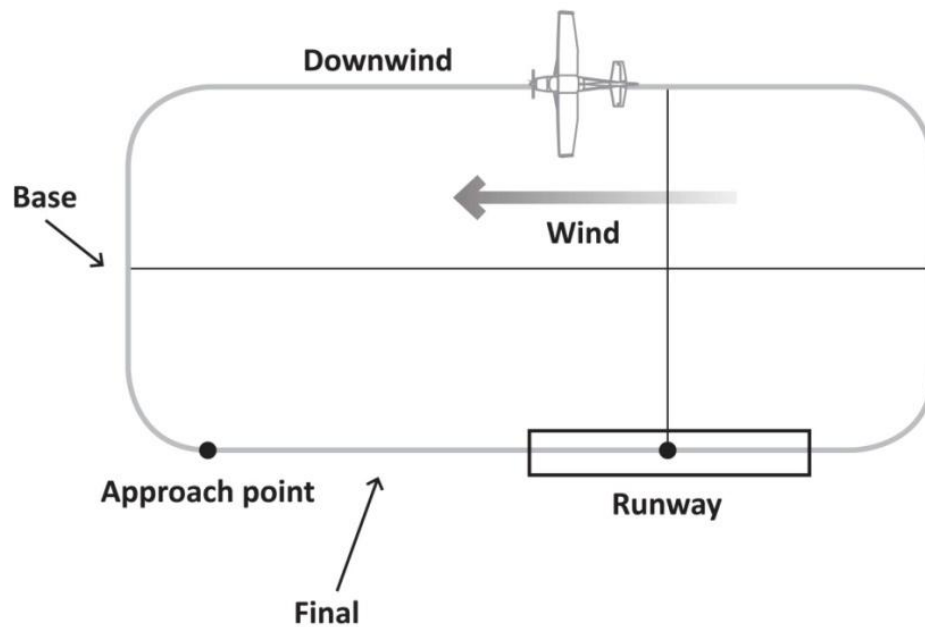


Figure 2.4 Lateral Landing Path

The aiming point on the runway in Figure 2.4 represents a user-programmable aiming point. The lateral trajectory parameters are also programmed via the ground station. The autonomous landing state machine is started on the downwind leg. In autonomous landing tests the safety pilot would fly the aircraft via remote control and arm the autopilot parallel to the runway near the downwind leg. The autopilot guides the aircraft onto the downwind leg from the initialisation point (point where autopilot was armed) onto the final leg, while maintaining altitude, airspeed and regulating the cross-track error to zero.

2.3 Project Execution

The points listed below give a brief overview of the skills that had to be developed, the challenges faced and the effort required:

- Control system design, aerodynamics, programming, system integration and troubleshooting had to be mastered.
- As there was no starting platform, a new platform had to be ordered and equipped. Considerable planning went into the placing of various sensors in the aircraft's fuselage and wings while keeping the aircraft's centre of gravity in a desirable position. The avionics box was custom-designed for the selected airframe to be easily inserted and removed from the

airframe. The IMU inside the avionics box had to be calibrated against temperature variations and the IMU's axis was aligned with the body axis of the aircraft. The magnetometer was calibrated to determine the aircraft's yaw angle as accurately as possible.

- The aircraft's moment of inertia was practically determined and the aerodynamic modelling was done in AVL (Athena Vortex Lattice). Furthermore a series of system identification flight tests were performed to gain insight on how the pilot flies and lands the aircraft and to confirm modelled parameters.
- Initially a low-cost GPS was used for flight tests. This GPS came standard with the ESL avionics stack. After enough trust was gained in the flight control system, the DGPS software (developed by the ESL engineers, AM de Jager and Lionel Basson) was integrated into the OBC code and the hardware was integrated into the avionics box and airframe. The new DGPS system was thoroughly tested on the ground and in the air before it was used in the autopilot.
- Preparation of a practical flight test entailed: the detailed planning of the flight test procedure which specified what was going to be tested as well as the test procedure; HIL simulations were used to verify the operation of the OBC and to mimic the actual flight test to ensure that everyone in the flight test crew knew what to expect during the flight test; preparation and moving the aircraft and flight test equipment. Finally the weather also placed a limit on the number (and frequency) of the flight tests; on some flight test occasions the weather changed so rapidly that the flight test had to be aborted; in other words, "pack up and go home at 7 in the morning!"

Chapter 3

Aircraft Modelling and Simulation

This chapter describes the aircraft model that serves as the basis for the design of the flight control system. The aircraft model was developed by [1] and uses a unique approach that splits the aircraft model into a fast and a slow set of aircraft dynamics. To derive the aircraft model, the chapter starts off with a definition of the various axis systems and notations used in the aircraft modelling process. With a firm grip on the modelling environment, the aircraft modelling process is started by describing the aircraft as a point-mass translating and rotating in the inertial frame. Thereafter, the forces and moments acting on the aircraft are described by developing a kinetic model. The slow set of dynamics (kinematics) is referred to as the outer-loop model and the fast set of dynamics (kinetics) as the inner-loop model. With the aircraft model derived, individual inner- and outer-loop controllers are designed separately to control different aspects of the aircraft in the chapters that follow.

3.1 Axis System Definitions and Notations

Three reference frames were used when modelling the dynamics of the aircraft: the inertial axis system, the wind axis system, and the body axis system.

3.1.1 Inertial Axes

The inertial axis system constitutes a reference frame in which Newton's laws can be applied. For short range UAV applications the standard North-East-Down (NED) axis system as shown in Figure 3.1 approximates an inertial axis system. The origin of the axis is conveniently chosen as the aircraft's starting point on a runway before take-off. The X_E -axis points in the north direction, the Y_E -axis points in the east direction and the Z_E -axis completes the right handed, orthogonal axis and points downwards towards the centre of the earth.

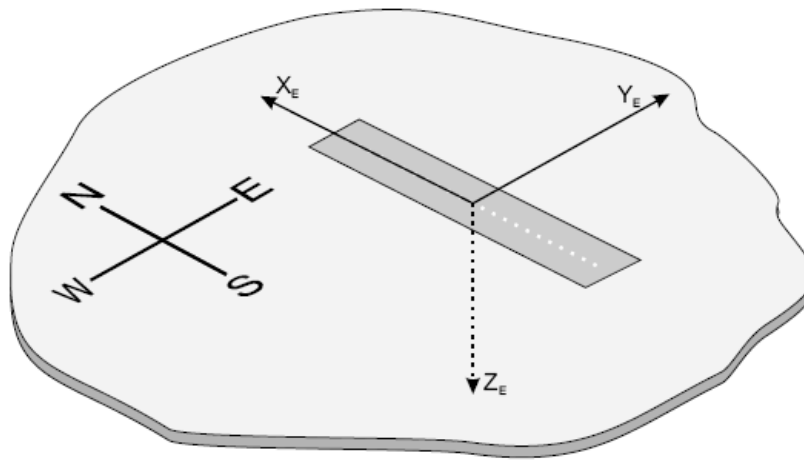


Figure 3.1 Inertial Axis System [22]

3.1.2 Fixed Body Axes

The origin of the fixed body axis system coincides with the aircraft's centre of mass. The X_B -axis lies in the aircraft's plane of symmetry and parallel to the fuselage reference line. The Y_B -axis lies perpendicular to the plane of symmetry and points towards the right-hand wing. The Z_B -axis completes the right-handed orthogonal axis system and points downwards relative to the cockpit. Figure 3.2 defines the notation for the forces, velocities, moments and rates used throughout this dissertation.

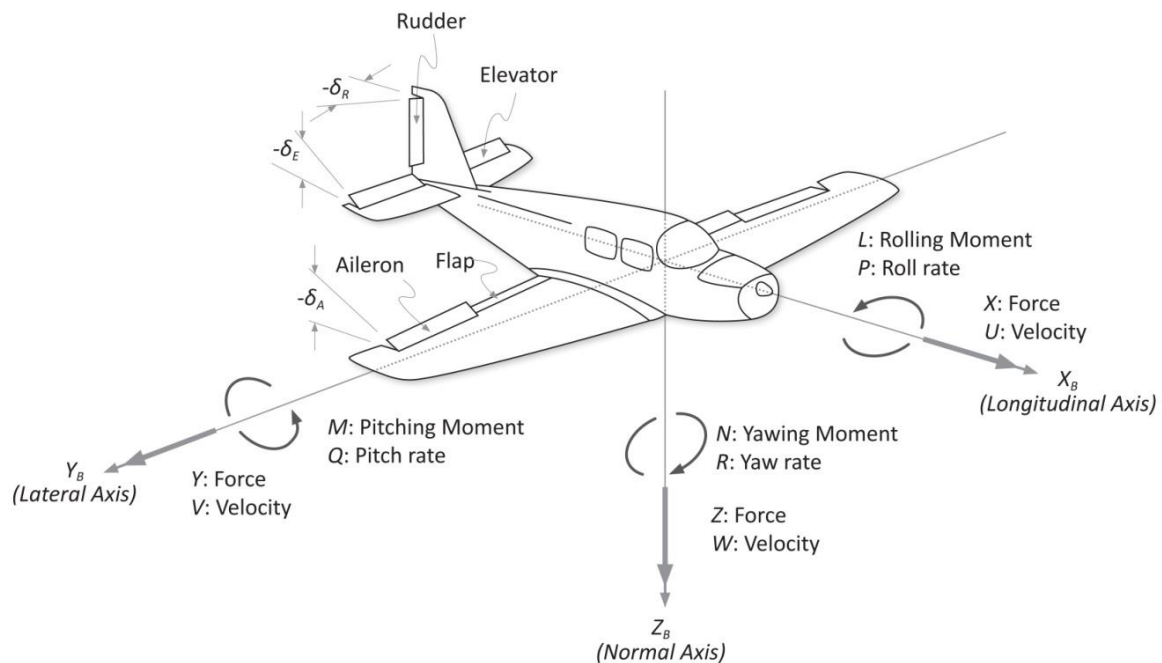


Figure 3.2 Fixed Body Axis System [23]

With reference to Figure 3.2, the conventional aerodynamic control surface deflections are defined below:

- δ_A – Aileron control surface deflection
Positive deflection causes a negative rolling moment.
- δ_E – Elevator control surface deflection
Positive deflection causes a negative pitching moment.
- δ_F – Flap control surface deflection
A large positive deflection causes a positive pitching moment.
- δ_R – Rudder control surface deflection
Positive deflection causes a negative yawing moment.

3.1.3 Wind Axes

The wind axis origin coincides with that of the body fixed axes, though its orientation is different. It is defined so that the X_W -axis points directly into the direction of the velocity vector. The Z_W -axis remains in the aircraft's plane of symmetry and points downwards relative to the cockpit. The Y_W -axis completes the right-hand axis system and points in the direction of the right-hand wing. With reference to Figure 3.3, the body axes can be transformed to wind axes by pitching the body axis negatively through the angle of attack (AoA), α , and then positively yawing around the Z_W -axis by the side-slip angle, β .

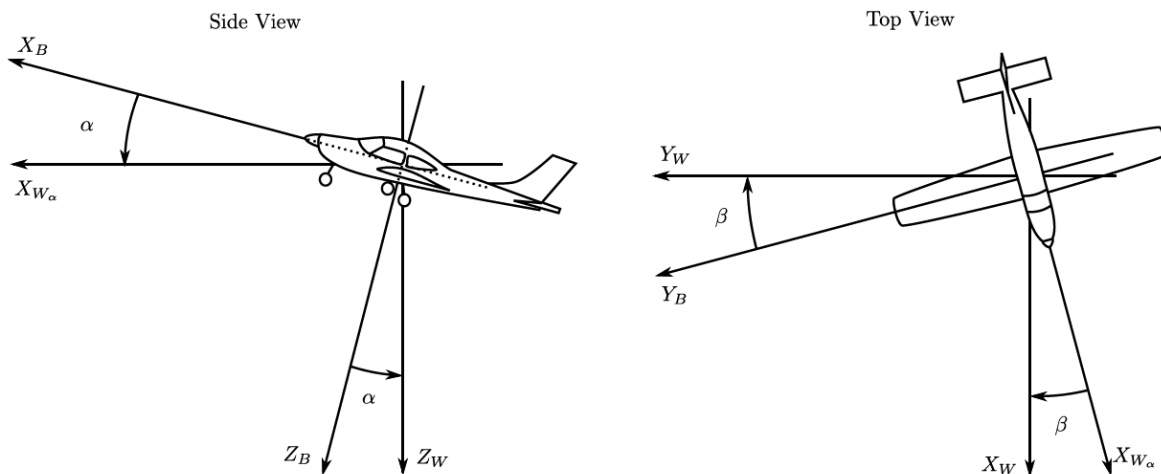


Figure 3.3 Wind Axes [23]

One of the best-known reasons for using the wind axes is that they are more convenient for describing aerodynamic forces. For instance, lift is perpendicular to the X_W -axis whereas drag is parallel to the X_W -axis. Referring to Figure 3.4, the definitions of the velocity magnitude \bar{V} , α and β can be written as

$$\bar{V} = \sqrt{U^2 + V^2 + W^2} \quad (3.1)$$

$$\alpha = \tan^{-1}\left(\frac{W}{U}\right) \quad (3.2)$$

$$\beta = \sin^{-1}\left(\frac{V}{\bar{V}}\right) \quad (3.3)$$

The inverse relationships are

$$U = \bar{V} \cos \alpha \cos \beta \quad (3.4)$$

$$V = \bar{V} \sin \beta \quad (3.5)$$

$$W = \bar{V} \sin \alpha \cos \beta \quad (3.6)$$

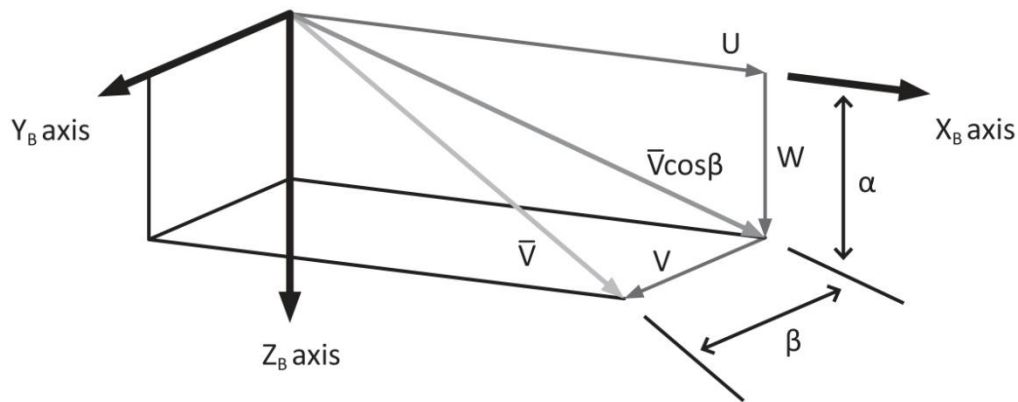


Figure 3.4 Polar Velocity Coordinates

3.2 Aircraft Model Overview

The aircraft's dynamics can be split into two sets of dynamics via the time-scale separation principle. Figure 3.5 graphically illustrates the concept for a faster and a slower set of aircraft dynamics. In Figure 3.5 the air density, ρ , is considered constant since the aircraft's flight altitude is constrained, with \mathbf{G}_I and \mathbf{G}_W representing the gravitational acceleration vectors coordinated in the inertial axes and wind axes respectively. As noted previously, the fast set of aircraft dynamics form the inner-loops (kinetics) and the slower set of dynamics form the outer-loops (kinematics).

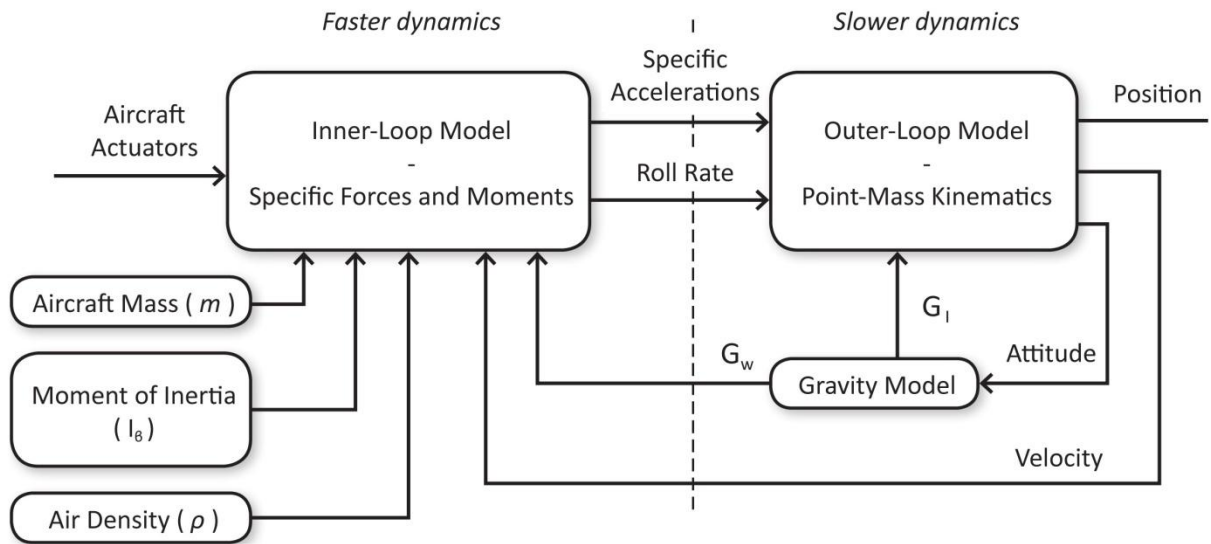


Figure 3.5 Aircraft Model Overview [1]

The outer and inner-loop controllers are derived in the remainder of this chapter. The aim in Chapter 4 and Chapter 5 is to design aircraft-dependent inner-loop controllers and independent outer-loop controllers.

3.3 Outer-Loop Model: Point-Mass Kinematics

This model describes the position, velocity and attitude of a point-mass that is able to rotate and translate in three-dimensional space. In the development of the outer-loop model the motion of the aircraft's wind axes is described relative to the inertial frame. In the two subsections below, the following topics are discussed: the point-mass dynamics and the attitude dynamics. Here the specific accelerations (A_W, B_W, C_W) and roll-rate (P_W) are inputs to the system.

3.3.1 Point-Mass Dynamics

In this project the aircraft is considered to be a rigid body with a static centre of mass. There exists a kinematic relationship between the position, velocity and acceleration of the aircraft's centre of mass with respect to inertial space (I). Based on the definition that the origin of the wind axes corresponds to the aircraft's centre of mass, the kinematic relationship can be expressed as

$$\frac{d}{dt} \mathbf{P}^{WI} \Big|_I = \mathbf{V}^{WI} \quad (3.7)$$

$$\frac{d}{dt} \mathbf{V}^{WI} \Big|_I = \mathbf{A}^{WI} \quad (3.8)$$

where \mathbf{P}^{WI} , \mathbf{V}^{WI} and \mathbf{A}^{WI} are the position, velocity and acceleration vectors of the wind axis system with respect to inertial space respectively. Equation (3.8) can be rewritten as the sum of the specific acceleration, Σ , and gravity vector, \mathbf{G} ,

$$\mathbf{A}^{WI} = \Sigma + \mathbf{G} \quad (3.9)$$

To relate to Equation (3.9), the mass of the aircraft is assumed to be a time-invariant parameter. By using Newton's second law the effect of a resultant force vector, \mathbf{F} , on the aircraft can be written as

$$\mathbf{F}^{WI} = m\mathbf{A}^{WI} \quad (3.10)$$

For the purpose of understanding the outer-loop control architecture, the velocity vector is described as the velocity magnitude and the attitude of the wind axis system. With this aim, the time derivative of the velocity vector in Equation (3.8) is transformed to the aircraft's wind axes by making use of the Coriolis equation. This equation transforms the time derivative of a vector X coordinated in a reference frame A to reference frame B , where ω is the angular velocity between B and A .

$$\left. \frac{d}{dt} \mathbf{V}^{WI} \right|_I = \left. \frac{d}{dt} \mathbf{V}^{WI} \right|_W + \boldsymbol{\omega}^{WI} \times \mathbf{V}^{WI} = \mathbf{A}^{WI} \quad (3.11)$$

Coordinating the Equation (3.11) in the wind axis system yields

$$\dot{\mathbf{V}}_W^{WI} + \mathbf{S}_W^{WI} \mathbf{V}^{WI} = \mathbf{A}_W^{WI} \quad (3.12)$$

where \mathbf{S}_W^{WI} is a skew symmetric matrix that implements the cross-product in Equation (3.12) and is defined as

$$\mathbf{S}_W^{WI} = \begin{bmatrix} 0 & -R_W & Q_W \\ R_W & 0 & -P_W \\ -Q_W & P_W & 0 \end{bmatrix} \quad (3.13)$$

In Equation (3.13), P_W , Q_W , R_W represent the roll, pitch and yaw rates of the wind axes with respect to inertial space. The equation describing the velocity vector of the aircraft coordinated in the wind axis system with respect to the inertial axis system is obtained by rearranging Equation (3.12) and substituting Equation (3.9) which results in

$$\dot{\mathbf{V}}_W^{WI} = -\mathbf{S}_W^{WI} \mathbf{V}^{WI} + \Sigma_W + \mathbf{DCM}^{WI} \mathbf{G} \quad (3.14)$$

which, after expanding, becomes

$$\begin{bmatrix} \dot{\bar{V}} \\ 0 \\ 0 \end{bmatrix} = - \begin{bmatrix} 0 & -R_W & Q_W \\ R_W & 0 & -P_W \\ -Q_W & P_W & 0 \end{bmatrix} \begin{bmatrix} \bar{V} \\ 0 \\ 0 \end{bmatrix} + \begin{bmatrix} A_W \\ B_W \\ C_W \end{bmatrix} + \mathbf{DCM}^{WI} \begin{bmatrix} 0 \\ 0 \\ g \end{bmatrix} \quad (3.15)$$

where \bar{V} is the velocity magnitude in the wind axes, and A_W , B_W and C_W are the components of the specific acceleration vector coordinated in wind axes. The \mathbf{DCM}^{WI} coordinates the gravity vector in the inertial axis to the wind axis system. The magnitude of the gravity vector in the inertial axis system is given by g . Equation (3.15) is rewritten as three equations: the first equation is the dynamic equation for the velocity magnitude in the wind axis and the other two are algebraic constraint equations.

$$\dot{\bar{V}} = A_W + g e_{12}^{WI} \quad (3.16)$$

$$\begin{bmatrix} R_W \\ Q_W \end{bmatrix} = \frac{1}{\bar{V}} \begin{bmatrix} e_{23}^{WI} \\ -e_{33}^{WI} \end{bmatrix} + \frac{1}{\bar{V}} \begin{bmatrix} B_W \\ -C_W \end{bmatrix} \quad (3.17)$$

In Equations (3.16) and (3.17), e_{xy}^{WI} corresponds to a row x and column y of the \mathbf{DCM}^{WI} matrix. Two additional algebraic constraint equations are generated by a similar derivation as above: by substituting the acceleration vector in the wind axis system of Equation (3.10) into Equation (3.12) and rearranging yields

$$\begin{bmatrix} R_W \\ Q_W \end{bmatrix} = \frac{1}{\bar{V}m} \begin{bmatrix} Y_W \\ -Z_W \end{bmatrix} \quad (3.18)$$

where Y_W and Z_W are elements of the total force vector coordinated in the wind axes. The result in Equation (3.18) will be used later in the development of the inner-loop model.

Equation (3.15) shows how acceleration propagates into velocity over time. The aim now is to describe the aircraft's position by integrating the velocity vector over time in Equation (3.7). Since the velocity vector coordinated in the wind axes is known, the \mathbf{DCM} is used to convert the velocity vector into inertial space. With this aim Equation (3.7) is rewritten as follows:

$$\dot{P}_I^{WI} = [\mathbf{DCM}^{WI}]^T \mathbf{V}_W^{WI} \quad (3.19)$$

Simplifying and expanding Equation (3.19) results in

$$\begin{bmatrix} \dot{P}_x \\ \dot{P}_y \\ \dot{P}_z \end{bmatrix} = \begin{bmatrix} \cos \psi_W \cos \theta_W \\ \sin \psi_W \cos \theta_W \\ -\sin \theta_W \end{bmatrix} \bar{V} \quad (3.20)$$

where P_x , P_y and P_z denote the aircraft's position in inertial space in the X , Y and Z directions.

3.3.2 Attitude Dynamics

Various methods exist to represent an aircraft's attitude. With the aim of autonomous landing for this project and knowing that the aircraft's flight envelope is of a conventional nature, the Euler 321 representation is chosen to describe the aircraft's attitude in the wind axis system. The aircraft's

attitude is described by the yaw (ψ_W) pitch (θ_W) and roll (ϕ_W) angles. The attitude dynamics are presented below in Equation (3.21):

$$\begin{bmatrix} \dot{\phi}_W \\ \dot{\theta}_W \\ \dot{\psi}_W \end{bmatrix}_{321} = \begin{bmatrix} 1 & \sin \phi_W \tan \theta_W & \cos \phi_W \tan \theta_W \\ 0 & \cos \phi_W & -\sin \phi_W \\ 0 & \sin \phi_W \sec \theta_W & \cos \phi_W \sec \theta_W \end{bmatrix}_{321} \begin{bmatrix} P_W \\ Q_W \\ R_W \end{bmatrix} \quad (3.21)$$

Equation (3.21) calculates the attitude of the aircraft's wind axis system with respect to the inertial axis system by using the yaw, pitch and roll-rates coordinated in the wind axis system as inputs.

3.4 Inner-Loop Model: Kinetics

The kinematic equation developed in the previous section maintains the motion of the wind axis system over time by using the specific accelerations and roll-rate as inputs. The inner-loop model investigates the rotational motion of the body axes relative to the wind axes. This section, in combination with the point-mass dynamics, aims to completely describe the six degree of freedom motion of the aircraft.

3.4.1 Rigid-Body Rotational Dynamics

Rotational motion arises from a force vector applied to a rigid body which does not align with the centre of mass of the object. Euler's second law regarding moments for a rigid body states that the rate of change in angular momentum (\mathbf{H}) about the objects centre of mass relative to the inertial reference frame, is equal to the external applied moment (\mathbf{M}), [24]:

$$\mathbf{M} = \frac{d}{dt} \mathbf{H} \Big|_I \quad (3.22)$$

The aim of the equation above is to describe the dynamics of the angular velocity of the body axes system relative to the wind axis. The time derivative in Equation (3.22) is transformed into the aircraft's body axis by making use of the Coriolis equation with $\boldsymbol{\omega}^{BI}$ being the angular velocity of the body axis system with respect to the inertial system. (A similar transformation was done for Equation (3.11).)

$$\mathbf{M} = \frac{d}{dt} \mathbf{H} \Big|_B + \boldsymbol{\omega}^{BI} \times \mathbf{H} \quad (3.23)$$

The angular momentum vector is in its simplest form when it is coordinated into body axes. In this axis system all moment arms to all mass elements are fixed and independent of the aircraft's motion. The angular momentum vector coordinated in body axes is given in [25] as

$$\mathbf{H}_B = \mathbf{I}_B \boldsymbol{\omega}_B^{BI} \quad (3.24)$$

where \mathbf{I}_B is the moment of inertia matrix of the aircraft coordinated in body axes. To obtain an equation that describes the change in angular velocity of the body axes relative to wind axes, Equation (3.24) is substituted into Equation (3.23) and coordinated into body axis:

$$\dot{\boldsymbol{\omega}}_B^{BI} = \mathbf{I}_B^{-1} (-\mathbf{S}_B^{BI} \mathbf{I}_B \boldsymbol{\omega}_B^{BI} + \mathbf{M}_B) \quad (3.25)$$

In the equation above \mathbf{S}_B^{BI} is a skew symmetric matrix that represents the cross-product. The angular velocity of the body axis system with respect to the inertial axis system is mathematically expressed as

$$\boldsymbol{\omega}^{BI} = \boldsymbol{\omega}^{BW} + \boldsymbol{\omega}^{WI} \quad (3.26)$$

The angular velocity of the wind axes relative to the body axes, $\boldsymbol{\omega}^{WB}$, can be obtained by two subsequent rotations. These rotations follow from the definition of the wind axis system covered in Section 3.1.3, where the body axes are transformed to wind axes by pitching the body axes negatively through α around the Y_B -axis and then positively yawing around the new Z_W -axis by β . The angular rate vector, $\boldsymbol{\omega}^{WB}$, is given by the respective angular rates ($\dot{\alpha}$ and $\dot{\beta}$) about their respective unit vectors:

$$\boldsymbol{\omega}^{WB} = -\dot{\alpha} \mathbf{j}^B + \dot{\beta} \mathbf{k}^W \quad (3.27)$$

Substituting Equation (3.27) into Equation (3.26) and by coordinating all the vectors into the aircraft's body axes yields

$$\boldsymbol{\omega}_B^{BI} = \dot{\alpha} \mathbf{j}_B^B - \dot{\beta} \mathbf{k}_B^W + \boldsymbol{\omega}_B^{WI} \quad (3.28)$$

which is now rewritten using the wind-to-body axes transformation matrices:

$$\boldsymbol{\omega}_B^{BI} = \dot{\alpha} \mathbf{j}_B^B - \dot{\beta} [\mathbf{DCM}^{BW}] \mathbf{k}_W^W + [\mathbf{DCM}^{BW}] \boldsymbol{\omega}_W^{WI} \quad (3.29)$$

Expanding and rearranging the equation above yields

$$\begin{bmatrix} P \\ Q \\ R \end{bmatrix} = \begin{bmatrix} 0 & \sin \alpha \\ 1 & 0 \\ 0 & -\cos \alpha \end{bmatrix} \begin{bmatrix} \dot{\alpha} \\ \dot{\beta} \end{bmatrix} + \begin{bmatrix} \cos \alpha \cos \beta & -\cos \alpha \sin \beta & -\sin \alpha \\ \sin \beta & \cos \beta & 0 \\ \sin \alpha \cos \beta & -\sin \alpha \sin \beta & \cos \alpha \end{bmatrix} \begin{bmatrix} P_W \\ Q_W \\ R_W \end{bmatrix} \quad (3.30)$$

where P , Q and R represent the roll, pitch and yaw rates of the body axis system with respect to the inertial axis system. By rearranging Equation (3.30) so that the vector containing $\dot{\alpha}$, $\dot{\beta}$ and P_W

becomes the subject of the equation, and substituting the two algebraic constraints from Equation (3.18) for Q_W and R_W yields

$$\begin{bmatrix} \dot{\alpha} \\ \dot{\beta} \\ P_W \end{bmatrix} = \begin{bmatrix} -\cos \alpha \cos \beta & 1 & -\sin \alpha \tan \beta \\ \sin \alpha & 0 & -\cos \alpha \\ \cos \alpha \sec \beta & 0 & \sin \alpha \sec \beta \end{bmatrix} \begin{bmatrix} P \\ Q \\ R \end{bmatrix} + \frac{1}{m\bar{V}} \begin{bmatrix} \sec \beta & 0 \\ 0 & 1 \\ -\tan \beta & 0 \end{bmatrix} \begin{bmatrix} Z_W \\ Y_W \end{bmatrix} \quad (3.31)$$

The two dynamic equations for $\dot{\alpha}$ and $\dot{\beta}$ above provide the attitude dynamics of the wind axis system relative to the body axis system, with the body axis angular rates and wind axis forces as inputs. The third component of Equation (3.31) is a constraint on P_W that ensures that the wind axes' normal vector remains in the aircraft's plane of symmetry. The complete rigid-body rotational dynamic equations are formed below by expanding Equation (3.25) and combining with Equation (3.31):

$$\begin{bmatrix} \dot{\alpha} \\ \dot{\beta} \end{bmatrix} = \begin{bmatrix} -\cos \alpha \cos \beta & 1 & -\sin \alpha \tan \beta \\ \sin \alpha & 0 & -\cos \alpha \end{bmatrix} \begin{bmatrix} P \\ Q \\ R \end{bmatrix} + \frac{1}{m\bar{V}} \begin{bmatrix} \sec \beta & 0 \\ 0 & 1 \end{bmatrix} \begin{bmatrix} Z_W \\ Y_W \end{bmatrix} \quad (3.32)$$

$$\begin{bmatrix} \dot{P} \\ \dot{Q} \\ \dot{R} \end{bmatrix} = \mathbf{I}_B^{-1} \left(- \begin{bmatrix} 0 & -R & Q \\ R & 0 & -P \\ -Q & P & 0 \end{bmatrix} \mathbf{I}_B \begin{bmatrix} P \\ Q \\ R \end{bmatrix} + \begin{bmatrix} L \\ M \\ N \end{bmatrix} \right) \quad (3.33)$$

with constraint

$$P_W = [\cos \alpha \sec \beta \quad 0 \quad \sin \alpha \sec \beta] \begin{bmatrix} P \\ Q \\ R \end{bmatrix} + \frac{1}{m\bar{V}} [-\tan \beta \quad 0] \begin{bmatrix} Z_W \\ Y_W \end{bmatrix} \quad (3.34)$$

The dynamics above describe the attitude of the body axis system with respect to the wind axis system over time as a function of the applied moment vector coordinated in body axes and the lateral and normal force vectors in wind axes.

3.4.2 Specific Forces and Moments

The previous sections modelled the aircraft as a six-degree-of-freedom rigid body with specific forces and moments acting on the aircraft. The specific forces consist of propulsion and aerodynamic forces. The aim of this section is to describe the propulsion and aerodynamic models with the end goal of describing the complete aircraft model in Chapter 4.

3.4.2.1 Thrust Model

In this project the aircraft was equipped with a Hyperion Zs-4025-10 brushless DC motor. The motor was mounted in such a way that the thrust vector coincided with the aircraft's X_B axis. Although there is an undesirable coupling between the thrust and the pitch rate dynamics, this coupling can be ignored for most aircraft since the thrust moment arm is often negligibly small. This assumption is made here and additionally the normal specific acceleration controller's bandwidth can also be designed larger than the thrust bandwidth so that the small pitch rate coupling can be treated as a disturbance.

The DC motor was tested on the thrust test jig that was developed in the ESL. The thrust step response test results are summarised in A.1.3. The response is extremely fast as would be expected from a DC motor, thus the engine can be adequately represented by a first order differential equation of:

$$\dot{T} = -\frac{1}{\tau_T}T + \frac{1}{\tau_T}T_c \quad (3.35)$$

where T is the thrust, T_c the commanded thrust and τ_T is the time constant defined in A.1.3. Note the dynamic effect that the velocity magnitude has on the thrust output is also ignored in this thrust model, since the effect is often negligible for control system design [1].

3.4.2.2 Aerodynamic Model

The small incidence angle aerodynamic model, for the specific forces (X_W, Y_W, Z_W) and moments (L_W, M_W, N_W) acting on the aircraft, modelled in wind axis system, is stated below [26]:

$$\begin{bmatrix} X_W \\ Y_W \\ Z_W \end{bmatrix} = qS \begin{bmatrix} -C_D \\ C_y \\ -C_L \end{bmatrix} + \begin{bmatrix} 1 \\ 0 \\ 0 \end{bmatrix} T \quad (3.36)$$

$$\begin{bmatrix} L_W \\ M_W \\ N_W \end{bmatrix} = qS \begin{bmatrix} b & 0 & 0 \\ 0 & c & 0 \\ 0 & 0 & b \end{bmatrix} \begin{bmatrix} C_l \\ C_m \\ C_n \end{bmatrix} \quad (3.37)$$

where

$$q = \frac{1}{2} \rho \bar{V}_a^2 \quad (3.38)$$

Here q is the dynamic pressure, ρ the air density, \bar{V}_a the airspeed, S the wing reference area, T the magnitude of the thrust vector, b the wing span and c the mean aerodynamic chord. The dimensionless aerodynamics coefficients C_D, C_y, C_L are the *drag*, *side force* and *lift* coefficients

respectively and the *roll*, *pitch* and *yaw* moment coefficients are denoted by C_l , C_m and C_n respectively. The dimensionless aerodynamics coefficients are expanded below by dimensionless stability and control derivatives. These dimensionless derivatives are mathematical descriptions that relate the change in specific forces and moments to changes in trim values:

$$C_D = C_{D_0} + \frac{C_L^2}{\pi A e} \quad (3.39)$$

$$\begin{aligned} \begin{bmatrix} C_y \\ C_L \end{bmatrix} &= \begin{bmatrix} 0 \\ C_{L_0} \end{bmatrix} + \begin{bmatrix} 0 & C_{y\beta} & \frac{b}{2\bar{V}_a} C_{yP} & 0 & \frac{b}{2\bar{V}_a} C_{yR} \\ C_{L\alpha} & 0 & 0 & \frac{c}{2\bar{V}_a} C_{LQ} & 0 \end{bmatrix} \begin{bmatrix} \alpha \\ \beta \\ P \\ Q \\ R \end{bmatrix} \\ &+ \begin{bmatrix} C_{y\delta_A} & 0 & C_{y\delta_R} & 0 \\ 0 & C_{L\delta_E} & 0 & C_{L\delta_F} \end{bmatrix} \begin{bmatrix} \delta_A \\ \delta_E \\ \delta_R \\ \delta_F \end{bmatrix} \end{aligned} \quad (3.40)$$

$$\begin{aligned} \begin{bmatrix} C_l \\ C_m \\ C_n \end{bmatrix} &= \begin{bmatrix} 0 \\ C_{m_0} \\ 0 \end{bmatrix} + \begin{bmatrix} 0 & C_{l\beta} & \frac{b}{2\bar{V}_a} C_{lP} & 0 & \frac{b}{2\bar{V}_a} C_{lR} \\ C_{m\alpha} & 0 & 0 & \frac{c}{2\bar{V}_a} C_{mQ} & 0 \\ 0 & C_{n\beta} & \frac{b}{2\bar{V}_a} C_{nP} & 0 & \frac{b}{2\bar{V}_a} C_{nR} \end{bmatrix} \begin{bmatrix} \alpha \\ \beta \\ P \\ Q \\ R \end{bmatrix} \\ &+ \begin{bmatrix} C_{l\delta_A} & 0 & C_{l\delta_R} & 0 \\ 0 & C_{m\delta_E} & 0 & C_{m\delta_F} \\ C_{n\delta_A} & 0 & C_{n\delta_R} & 0 \end{bmatrix} \begin{bmatrix} \delta_A \\ \delta_E \\ \delta_R \\ \delta_F \end{bmatrix} \end{aligned} \quad (3.41)$$

In Equation (3.39), C_{D_0} is defined as the parasitic drag coefficient, e is the Oswald efficiency factor and A is the wing's aspect ratio. The static lift and pitching moment coefficients in Equation (3.40) and (3.41) are defined by C_{L_0} and C_{m_0} respectively. The terms of the form

$$C_{Ax} = \frac{\partial C_A}{\partial x'} \quad (3.42)$$

with

$$x' = nx \quad (3.43)$$

are the non-dimensional stability and control derivatives where n is the appropriate normalising coefficient for x . For the derivatives with respect to pitch rate, the appropriate normalising coefficient is $c/2\bar{V}_a$ and for roll and yaw rate it is $b/2\bar{V}_a$. The normalising coefficient is unity for incidence and control deflection angles.

In the aerodynamic model above, the derivatives concerning main wing downwash lag [27] on the horizontal tail $C_{m\dot{\alpha}}$ and the added mass effect $C_{L\dot{\alpha}}$ [26] are often negligibly small for conventional airframes. Furthermore the assumption is made that the stability and control derivatives are not a function of the rigid-body rotational parameters. This assumption is valid for the aircraft operating in per-stall flight conditions with small incidence angles.

Note that the rigid-body rotational dynamics presented in this section provide the forces and moments coordinated in wind axes. The rigid-body rotational dynamics derived in Section 3.4.1 require the moment vector coordinated in body axes. The DCM^{BW} transformation matrix is applied to the moment vector coordinated in wind axes and yields the desired result:

$$\mathbf{M}_B = DCM^{BW} \mathbf{M}_W \quad (3.44)$$

3.5 Summary

The different axis systems in which the aircraft is modelled were introduced in this chapter. The outer-loop model was derived based on the aircraft's point-mass kinematics and is therefore aircraft-independent. The inner-loop controllers were also derived and are aircraft-dependant, they act as virtual actuators that are used by the outer-loop controllers to regulate the aircraft on its track. With the aircraft model derived, the next step is to design the inner-loop and outer-loop controllers.

Chapter 4

Inner-Loop Controllers

Chapter 3 presented the derivation of the inner- and outer-loop models of the aircraft. This chapter starts by simplifying and decoupling the aircraft's inner-loop model to specific axial, normal and lateral models. These models are then used to design three separate specific acceleration controllers and a roll-rate controller. The main idea in the design of each of the controllers is to create high-bandwidth feedback controller to compensate for model uncertainty and fast disturbance rejection. These controllers are also augmented with integrators to remove steady-state disturbances. With the inner-loop controllers designed, an interface to the outer-loop controllers is established that encapsulates all the aircraft's model uncertainties. In each of the controller design sections, the theoretical design process will be outlined, followed by practical pole-placement considerations, simulation results, and will conclude with practical flight test results. In the practical flight test section of each controller, the flight testing approach is stated, followed by the expected outcome, followed by the flight test data analysis and conclusion.

4.1 Simplifying and Decoupling the Aircraft Model

In order to simplify inner-loop models, the first step is to make use of standard small-angle trigonometric assumptions. The small angles of interest are the two incidence angles α and β . Furthermore the product of the two small angles is also assumed to be negligible. As an additional assumption the side-slip angle is assumed to be near zero. This assumption is based on the coordinated nature of normal flight. To aid in the validity that the side-slip angle is near zero an additional controller is designed later in this chapter that regulates the side-slip angle to zero via the rudder.

The inertial cross-coupling terms in Equation (3.33) can be ignored for most autopilot applications since the cross-coupling terms are only present when the aircraft is in a state such that it experiences large angular velocities around two of its axes simultaneously. With a non-aerobatic flight envelope, the aircraft will never deliberately enter this state. By applying the simplifications discussed above to the rigid-body rotational dynamics developed in Chapter 3, the dynamic equations can be rewritten as follows:

$$\begin{bmatrix} \dot{\alpha} \\ \dot{\beta} \end{bmatrix} = \begin{bmatrix} 0 & 1 & 0 \\ 0 & 0 & -1 \end{bmatrix} \begin{bmatrix} P \\ Q \\ R \end{bmatrix} + \frac{1}{m\bar{V}} \begin{bmatrix} 1 & 0 \\ 0 & 1 \end{bmatrix} \begin{bmatrix} Z_W \\ Y_W \end{bmatrix} \quad (4.1)$$

$$\begin{bmatrix} \dot{P} \\ \dot{Q} \\ \dot{R} \end{bmatrix} = I_B^{-1} \begin{bmatrix} L \\ M \\ N \end{bmatrix} \quad (4.2)$$

with

$$\begin{bmatrix} X_W \\ Y_W \\ Z_W \end{bmatrix} = qS \begin{bmatrix} -C_D \\ C_y \\ -C_L \end{bmatrix} + \begin{bmatrix} 1 \\ 0 \\ 0 \end{bmatrix} T \quad (4.3)$$

$$\begin{bmatrix} L_W \\ M_W \\ N_W \end{bmatrix} = qS \begin{bmatrix} b & 0 & 0 \\ 0 & c & 0 \\ 0 & 0 & b \end{bmatrix} \begin{bmatrix} C_l \\ C_m \\ C_n \end{bmatrix} \quad (4.4)$$

$$[P_W] = [1 \quad 0 \quad 0] \begin{bmatrix} P \\ Q \\ R \end{bmatrix} \quad (4.5)$$

The three linear decoupled inner-loop models are obtained by substituting the specific forces and moments coordinated in the wind axis system, Equations (4.3) and (4.4) into Equations (4.1) and (4.2). In the substitution above, the moments coordinated in the wind axes system are not transformed to moments in the body axes. This simplification is based on the argument given in [1] that the aerodynamic model's uncertainty is far greater than the added inaccuracy. The three sets of linear decoupled inner-loop models resulting from the substitution are given below.

Axial:

$$\dot{T} = -\frac{1}{\tau_T} T + \frac{1}{\tau_T} T_C \quad (4.6)$$

$$A_W = \frac{1}{m} T - \frac{qS}{m} C_D \quad (4.7)$$

Normal:

$$\begin{bmatrix} \dot{\alpha} \\ \dot{Q} \end{bmatrix} = \begin{bmatrix} -\frac{L_\alpha}{m\bar{V}} & 1 - \frac{L_Q}{m\bar{V}} \\ \frac{M_\alpha}{I_y} & \frac{M_Q}{I_y} \end{bmatrix} \begin{bmatrix} \alpha \\ Q \end{bmatrix} + \begin{bmatrix} -\frac{L_{\delta_E}}{m\bar{V}} \\ \frac{M_{\delta_E}}{I_y} \end{bmatrix} \delta_E + \begin{bmatrix} \frac{g}{\bar{V}} e_{33}^{WI} \\ 0 \end{bmatrix} \quad (4.8)$$

$$[C_W] = \begin{bmatrix} -\frac{L_\alpha}{m} & \frac{L_Q}{m} \end{bmatrix} [\alpha] + \begin{bmatrix} -\frac{L_{\delta_E}}{m} \end{bmatrix} \delta_E \quad (4.9)$$

Lateral:

$$\begin{bmatrix} \dot{\beta} \\ \dot{P} \\ \dot{R} \end{bmatrix} = \begin{bmatrix} \frac{Y_\beta}{mV} & 0 & \frac{Y_R}{mV} - 1 \\ \frac{L_\beta}{I_x} & \frac{L_p}{I_x} & \frac{L_R}{I_x} \\ \frac{N_\beta}{I_z} & \frac{N_p}{I_z} & \frac{N_R}{I_z} \end{bmatrix} \begin{bmatrix} \beta \\ P \\ R \end{bmatrix} + \begin{bmatrix} 0 & \frac{Y_R}{mV} \\ \frac{L_{\delta_A}}{I_x} & \frac{L_{\delta_R}}{I_x} \\ \frac{N_{\delta_A}}{I_z} & \frac{N_{\delta_R}}{I_z} \end{bmatrix} \begin{bmatrix} \delta_A \\ \delta_R \end{bmatrix} + \begin{bmatrix} \frac{g}{V} e_{23}^{WI} \\ 0 \\ 0 \end{bmatrix} \quad (4.10)$$

$$\begin{bmatrix} B_W \\ P_W \end{bmatrix} = \begin{bmatrix} \frac{Y_\beta}{V} & 0 & \frac{Y_R}{m} \\ 0 & 1 & 0 \end{bmatrix} \begin{bmatrix} \beta \\ P \\ R \end{bmatrix} + \begin{bmatrix} \frac{Y_R}{m} \end{bmatrix} \delta_R \quad (4.11)$$

In the notation above Y_β represents the side force due to side-slip angle, L_β represents the roll moment due to side-slip angle etc. This dimensional derivative notation is used to simplify the representation of the inner-loop model and is defined in A.3.4. The velocity magnitude in the normal and lateral models above acts as a parameter while in the outer-loop point-mass kinematics it is a dynamic variable. In [1] the aim is to remove the dynamic coupling of the velocity magnitude into the rigid-body rotational dynamics making the dynamics independent of the point-mass kinematics by employing a time-scale separation strategy between the inner-loop and outer control loop. Figure 3.5 illustrates this coupling graphically. If the outer-loop dynamics is kept slower than the inner-loop, the velocity magnitude can be considered constant in the inner-loops. The aim in the remainder of this chapter is to design high-bandwidth inner-loop controllers that can be time-scale separated to slower outer-loop controllers.

4.2 Normal Specific Acceleration Controller

The controller designed in this section uses the aircraft's elevator to control the aircraft's normal specific acceleration (NSA) by controlling the amount of lift generated by the main wing. The controller architecture provides a full pole-placement strategy for the NSA dynamics.

In this document when a reference is made to the "clean configuration" it means that the aircraft's flaps are deflected to 0° . When it is stated that the aircraft is in "flaps configuration" the flaps are deflected downwards to 22° . The effect that the flaps have on the closed-loop NSA dynamics for the aircraft in clean configuration is investigated in Section 4.2.3.

4.2.1 Design

In the NSA model restated below from Equations (4.8) and (4.9), gravity acts as an unwanted flight path angle coupling input to the NSA dynamics. By removing gravity an attitude-independent NSA controller can be created. Since the NSA model describes accurately how the gravity term enters the NSA dynamics its effect can be removed from the system by using feedback linearisation.

$$\begin{bmatrix} \dot{\alpha} \\ \dot{Q} \end{bmatrix} = \begin{bmatrix} -\frac{L_\alpha}{mV} & 1 - \frac{L_Q}{mV} \\ \frac{M_\alpha}{I_y} & \frac{M_Q}{I_y} \end{bmatrix} \begin{bmatrix} \alpha \\ Q \end{bmatrix} + \begin{bmatrix} -\frac{L_{\delta_E}}{mV} \\ \frac{M_{\delta_E}}{I_y} \end{bmatrix} \delta_E + \begin{bmatrix} \frac{g}{V} e_{33}^{WI} \\ 0 \end{bmatrix} \quad (4.12)$$

$$[C_W] = \begin{bmatrix} -\frac{L_\alpha}{m} & \frac{L_Q}{m} \end{bmatrix} \begin{bmatrix} \alpha \\ Q \end{bmatrix} + \begin{bmatrix} -\frac{L_{\delta_E}}{m} \end{bmatrix} \delta_E \quad (4.13)$$

Feedback linearisation is a method for transforming non-linear models into linear ones. One of its constraints is that the system should not have any non-minimum phase (NMP) zeros. With this constraint in mind, the open-loop NSA dynamics are analysed in Figure 4.1 at the aircraft's trim airspeed. In Figure 4.1 the short-period mode poles can be seen along with an NMP zero and left-hand plane zero. A natural frequency range of the NSA dynamics in which the NMP nature can be ignored has been defined in [1]. By adhering to the frequency constraints, the NSA controller can be designed independently of the LHP zero and NMP nature, which also allows for dynamic inverting the effect of the flight path angle coupling. The upper bound of the natural frequency of the NSA dynamics is given by Equation (4.14).

$$\omega_n < \frac{1}{3} Z_{\text{NMP}} \quad (4.14)$$

where the NMP zero can be approximated by

$$Z_{\text{NMP}} \approx \sqrt{\frac{L_\alpha}{I_y} \left(\frac{M_\alpha}{L_\alpha} - \frac{M_{\delta_E}}{L_{\delta_E}} \right)} \quad (4.15)$$

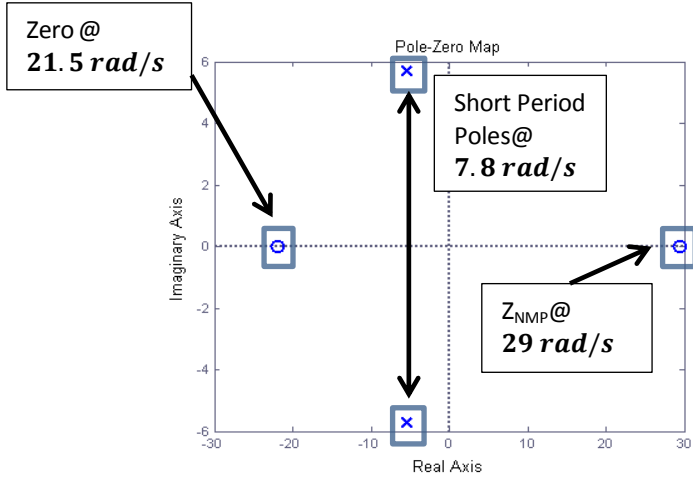
With the upper bound of the natural frequency of the NSA dynamics defined, the next step is to investigate the LHP zero and the NMP nature of the NSA dynamics with the aim of removing the effects that these zeros have on the dynamics.

The NMP nature of the NSA dynamics arises from a small lift force induced on the tailplane when the elevator is perturbed, and it places a zero in the right half-plane. The NMP nature is ignored by setting the lift force due to elevator equal to zero.

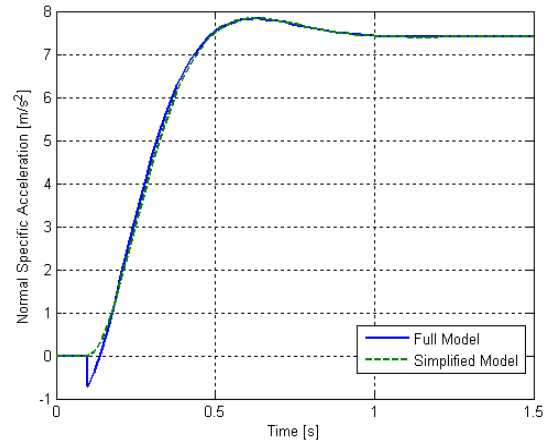
$$L_{\delta_E} = 0 \quad (4.16)$$

The left-hand plane zero in Figure 4.1 is caused by lift force generated by an induced angle of incidence on the tailplane when the aircraft experiences a pitch rate. The left-hand plane zero is located at a high frequency and by adhering to Equation (4.14) it has no real impact on the dynamics. It is removed from the NSA dynamics by assuming that

$$L_{\delta_E} = 0 \quad (4.17)$$



(a) Open-loop Pole-zero Map



(b) Step Responses of the Full and Simplified Models

Figure 4.1 Open-Loop Pole-Zero Map of NSA Dynamics with Step Responses

After simplification, the NSA dynamic equations become

$$\begin{bmatrix} \dot{\alpha} \\ \dot{Q} \end{bmatrix} = \begin{bmatrix} -\frac{L_\alpha}{mV} & 1 \\ \frac{M_\alpha}{I_y} & \frac{M_Q}{I_y} \end{bmatrix} \begin{bmatrix} \alpha \\ Q \end{bmatrix} + \begin{bmatrix} 0 \\ \frac{M_{\delta_E}}{I_y} \end{bmatrix} \delta_E + \begin{bmatrix} \frac{g}{V} e_{33}^{WI} \\ 0 \end{bmatrix} \quad (4.18)$$

$$[C_W] = \begin{bmatrix} -\frac{L_\alpha}{m} \end{bmatrix} [\alpha] \quad (4.19)$$

The NSA dynamics is augmented with an integrator to remove steady-state errors

$$\dot{E}_C = C_W - C_{WR} \quad (4.20)$$

By differentiating Equation (4.19) and substituting $\dot{\alpha}$ from (4.18) the NSA dynamics can be written in terms of NSA, pitch rate and the augmented error integrator:

$$\begin{bmatrix} \dot{C}_W \\ \dot{Q} \\ \dot{E}_C \end{bmatrix} = \begin{bmatrix} -\frac{L_\alpha}{mV} & -\frac{L_\alpha}{m} & 0 \\ \frac{mM_\alpha}{I_y L_\alpha} & \frac{M_Q}{I_y} & 0 \\ 1 & 0 & 0 \end{bmatrix} \begin{bmatrix} C_W \\ Q \\ E_C \end{bmatrix} + \begin{bmatrix} 0 \\ M_{\delta_E} \\ I_y \\ 0 \end{bmatrix} \delta_E + \begin{bmatrix} 0 \\ 0 \\ -1 \end{bmatrix} C_{W_R} + \begin{bmatrix} -\frac{L_\alpha g}{mV} e_{33}^{WI} \\ 0 \\ 0 \end{bmatrix} \quad (4.21)$$

The elevator control law defined in Equation (4.22) allows for full pole-placement as well as a feed-forward term from the reference input to place a closed-loop zero.

$$\delta_E = K_Q Q - K_C C_W - K_E E_C + N_C C_{W_R} + \delta_{EG} \quad (4.22)$$

In the equation above δ_{EG} is the feedback linearisation term that removes the unwanted flight path angle coupling by creating an effect opposite to the unwanted gravity coupling in the control input. The feedback linearisation control law derived in [1] to cancel flight path angle coupling is given by

$$\delta_{EG} = \frac{gI_y}{VM_{\delta_E}} \left[\left(\frac{M_Q}{I_y} - \frac{M_{\delta_E}}{I_y} K_Q \right) e_{33}^{WI} + \left(\alpha_2 - \frac{L_\alpha}{mV} + \frac{M_Q}{I_y} \right) e_{13}^{WI} + P_W e_{23}^{WI} \right] \quad (4.23)$$

By substituting the elevator control law into the NSA dynamics the closed-loop system becomes

$$\begin{bmatrix} \dot{C}_W \\ \dot{Q} \\ \dot{E}_C \end{bmatrix} = \begin{bmatrix} -\frac{L_\alpha}{mV} & -\frac{L_\alpha}{m} & 0 \\ -\frac{mM_\alpha}{I_y L_\alpha} - \frac{M_{\delta_E}}{I_y} K_C & \frac{M_Q}{I_y} - \frac{M_{\delta_E}}{I_y} K_Q & -\frac{M_{\delta_E}}{I_y} K_E \\ 1 & 0 & 0 \end{bmatrix} \begin{bmatrix} C_W \\ Q \\ E_C \end{bmatrix} + \begin{bmatrix} 0 \\ M_{\delta_E} N_C \\ -1 \end{bmatrix} C_{W_R} \quad (4.24)$$

Note from the above substitution that the feedback linearisation term δ_{EG} removed the gravity coupling. By calculating the characteristic equation of the closed-loop system above

$$\begin{aligned} \alpha_c(s) = & s^3 + s^2 \left(\frac{M_{\delta_E}}{I_y} K_Q + \frac{L_\alpha}{mV} - \frac{M_Q}{I_y} \right) \\ & + s \left(\frac{L_\alpha M_{\delta_E}}{mV I_y} (K_Q - V K_C) - \frac{L_\alpha M_Q}{mV I_y} - \frac{M_\alpha}{I_y} \right) - \frac{L_\alpha M_{\delta_E}}{m I_y} K_E \end{aligned} \quad (4.25)$$

and matching the coefficients to the desired closed-loop characteristic equation below

$$\alpha_c(s) = s^3 + \alpha_2 s^2 + \alpha_1 s + \alpha_0 \quad (4.26)$$

the control law gains can be calculated

$$K_Q = \frac{I_y}{M_{\delta_E}} \left(\alpha_2 - \frac{L_\alpha}{mV} + \frac{M_Q}{I_y} \right) \quad (4.27)$$

$$K_C = \frac{mI_y}{L_\alpha M_{\delta_E}} \left(\alpha_2 + \frac{M_Q}{I_y} - \frac{L_\alpha}{mV} \alpha_2 + \left(\frac{L_\alpha}{mV} \right)^2 \right) \quad (4.28)$$

$$K_E = \frac{mI_y}{L_\alpha M_{\delta_E}} \alpha_0 \quad (4.29)$$

The feed-forward zero is placed by N_C

$$N_C = \frac{K_E}{z_f} \quad (4.30)$$

where z_f is the location of the desired zero.

4.2.2 Pole-Placement and Simulation

The OBC used in this project introduces one sample period delay of 0.02 s in the system. This implies that the control will only be applied on the cycle following that during which the sensor measurements are taken. Limiting factors for pole-placement of the NSA dynamics are listed below:

1. The lower bound constraint on the position of the closed-loop poles exists to implement a time-scale separation between the inner- and outer-loop controllers. This lower bound constraint requires the inner-loop controller's slowest dynamics (ideally) to be five times faster than the outer-loop controller's fastest dynamics.
2. The upper bound on pole positions is enforced by the NMP zero that has been ignored to simplify the NSA dynamics. If the closed-loop poles of the system are at least three times slower in frequency than the NMP zero, its effects on the dynamics of the aircraft becomes negligibly small.
3. A limit is placed on the control effort to move the open-loop poles by the single sample period delay that the OBC introduces. A Z-plane analysis in [19] and [20] showed that by significantly increasing the control effort to move the open-loop short period mode poles and integrator pole far from their open-loop locations, resulted in entirely different undesirable closed-loop pole locations. The Z-plane analysis concluded that if the open-loop poles are close to their closed-loop pole counterparts with their damping factor changed, the control system delay can be ignored. This limiting factor for closed-loop pole-placement is considered for all inner-loop controllers.

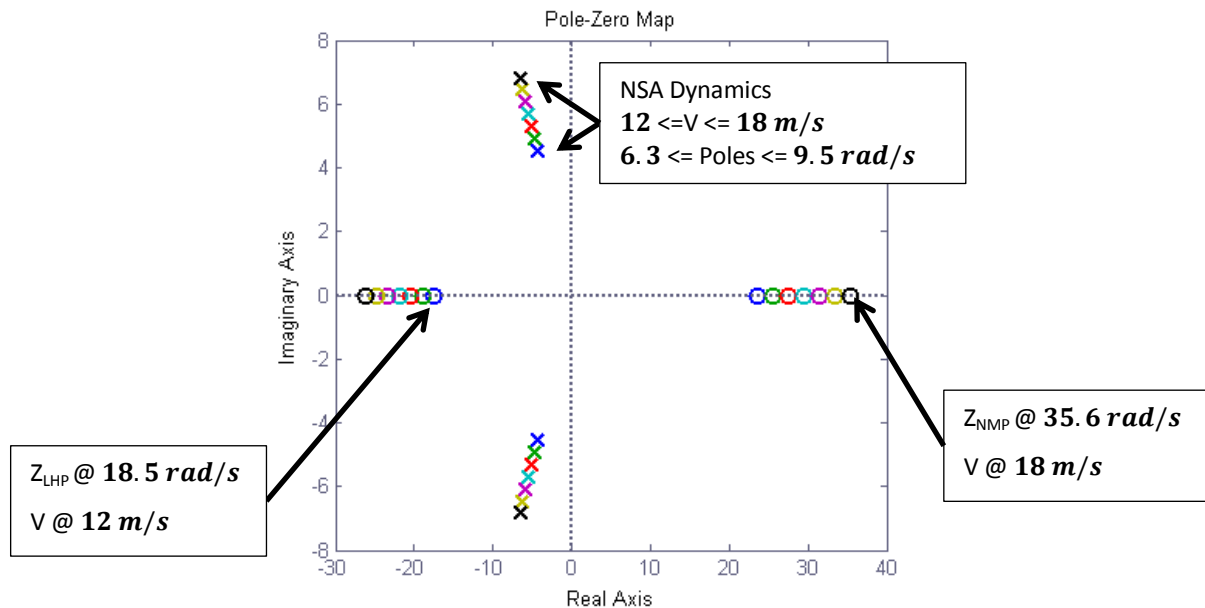


Figure 4.2 Pole-Zero Map of the NSA Dynamics over the Velocity Range of Interest

With these limiting factors in mind, the NSA dynamics are analysed to select closed-loop pole locations for the velocity range of operation. The velocity range of operation for this project is chosen in the range from 14 m/s to 18 m/s , with the lower velocity bound based on the practical flight test data to ensure that the aircraft remains in a pre-stall flight condition during landing. Figure 4.2 presents the open-loop poles and zeros over a velocity range from 12 m/s to 18 m/s . Referring to Figure 4.2, it can be seen that velocity acts as a scaling factor for the poles and the zeros. With this result in mind the upper bound of the natural frequency of the NSA dynamics can now be defined. The NMP zero is located at 35 rad/s thus the upper bound for the closed-loop NSA dynamics is set to a third of this frequency at 11.88 rad/s . The lower bound for time-scale separation from the slower outer-loop controller is determined by the augmented integrator.

The integrator pole frequency is chosen slightly lower than the short-period poles located at 7.4 rad/s on the pole-zero map at 14 m/s at the end of the flight operating range. The integrator pole was placed at 6 rad/s . The integrator pole could also have been placed at a higher frequency. This however creates a more aggressive control system that rejects wind gusts and unmodelled dynamics more quickly. A slower integrator pole does the opposite and results in a more practically manageable (less sensitive) control system which is desirable in the final stage of landing. The closed-loop pole-placement region for the NSA dynamics is illustrated in Figure 4.3.

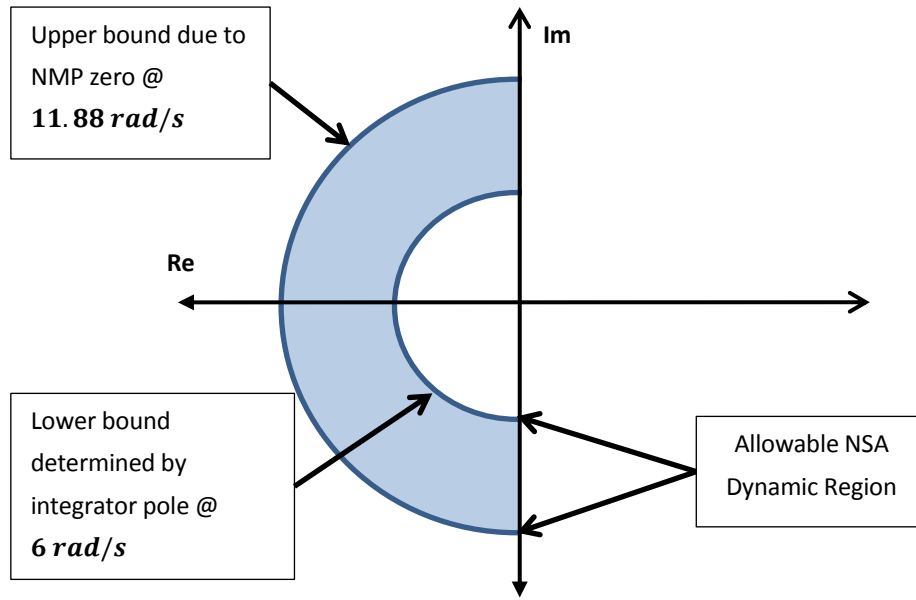


Figure 4.3 Allowable Pole-Placement Region for the Closed-Loop NSA Dynamics

The feed-forward zero is placed at a frequency 70% higher than that of the fixed integrator pole. At this frequency the feed-forward zero will remove some of the integrator dynamics and avoid providing too much feed-forward from low frequency noise in the reference. Finally the short-period poles are placed at the same frequency as their open-loop counterparts with a damping ratio of $\zeta = 0.707$ for the entire velocity range of operation.

With the controller designed, the HIL simulated step response is illustrated in Figure 4.4. Note that the step response is sampled four times slower than the OBC sample frequency. The step response is fast and well damped with a 0 to 100% rise time of 0.38 s and 7% overshoot. Right at the start of the step response a very small amount of undershoot can be seen which results from the NMP nature of the short-period mode. The remainder of the step response results from a combination of the short-period poles, feed-forward zero and the augmented integrator. The simulation was performed at 18 m/s and not at the aircraft trim speed in order to compare with the NSA practical step response test which was performed at approximately 18 m/s. The simulation was concluded shortly after the transient response but before effects due to divergence from outer kinematic states could take effect.

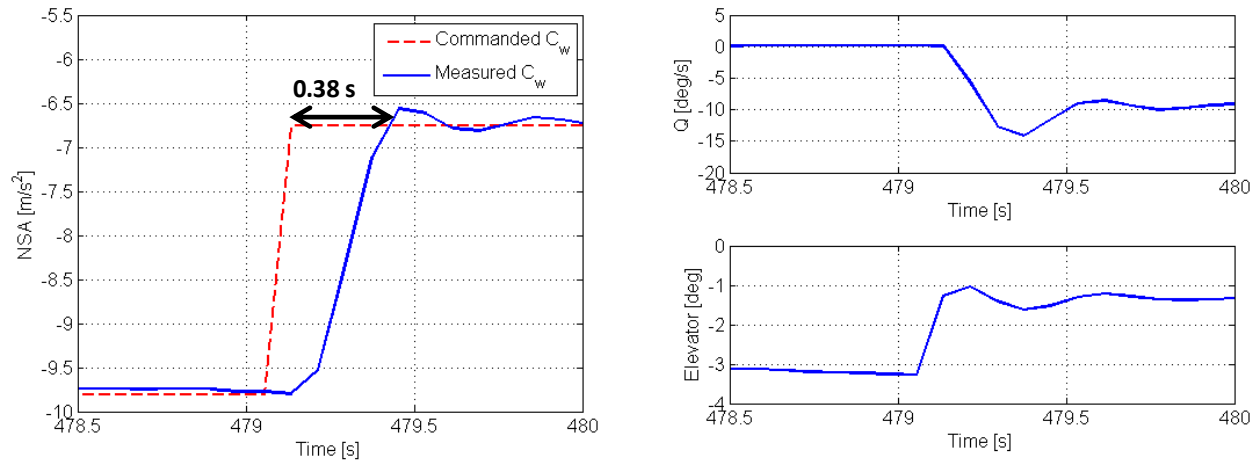


Figure 4.4 NSA HIL Simulation Non-Linear Step Response at 18 m/s

4.2.3 Effect of Flaps on the Closed-Loop Normal Specific Acceleration Dynamics

Two different sets of aircraft model coefficients were obtained via AVL for the aircraft in both the clean and flap configurations. By comparing the two sets of aircraft coefficients, it was found that the magnitude of the longitudinal parameters changed by less than 10%. Table 4.1 shows the stability derivatives for the aircraft in clean and flap configurations. An AVL analysis also showed that the aircraft is expected to experience a positive pitching moment when the flaps are deflected. An AVL trim analysis for the aircraft in flap configuration calculated a trim elevator command of 3° , which cancels the positive pitching moment caused by the flaps.

Table 4.1 Longitudinal Stability Derivatives for the Aircraft in Clean and Flap Configurations

Longitudinal stability derivative	Clean configuration	Flap configuration
$C_{L\alpha}$	4.591	4.65
$C_{m\alpha}$	-0.660	-0.626
C_{m_q}	-7.619	-7.654

If the assumption is made that the aircraft model for the clean and flap configurations obtained from AVL are relatively accurate, then the small shift in open-loop pole locations of the NSA dynamics for the clean and flap configurations are small and can be ignored.

4.2.4 Normal Specific Acceleration Controller Practical Flight Test

The goal of this test was to evaluate the NSA controller's practical response for the aircraft in clean and flap configurations to verify the simplifications and assumptions made in the theoretical design. In this project a safe approach was adopted to minimise the risk of testing a fast controller that has direct control over the elevator by placing bounds on the maximum/minimum elevator deflection and normal specific acceleration that the NSA controller can command. To this end the NSA controller was first tested implicitly via the outer-loop controller to verify NSA controller stability, and then tested directly. Section 4.2.4.1 investigates the NSA controller's step response. Section 4.2.4.2 investigates the outer-loop controller's performance at a specific time-scale separation distance between NSA controller and outer-loop controller.

4.2.4.1 Normal Specific Acceleration Step Response Test

In this test the safety pilot has control over all the aircraft's actuators except for the elevator, which will be commanded by the NSA controller during the flight test. The aircraft is expected to enter a steep climb for a few seconds, after which the safety pilot retakes full control.

The safety pilot was instructed to keep the throttle at a constant setting during the NSA step response test. For this test the safety pilot trimmed the aircraft at a safe altitude of 150 m, then the NSA controller was armed with an initial command of -9.81 m/s^2 . Once the aircraft's normal specific acceleration settled at -9.81 m/s^2 , a normal specific acceleration step command of -13.81 m/s^2 was issued, after which the aircraft entered a steep climb. A few seconds after completion of the transient response resulting from the step command, effects from divergent outer kinematic states were observed. Figure 4.5 and Figure 4.6 illustrate the NSA step response for the aircraft in clean and flap configurations respectively. The same NSA feedback gains were used in both cases. On this particular flight test day wind-finder (online weather tool) reported approximated wind gusts with a maximum magnitude of 4 m/s. On a flight test day it is difficult to compare the actual wind/gust magnitude with wind-finder readings, since wind/gust magnitudes differ on the ground and in the air. By looking at a tree top across the runway and analysing data of a similar flight test performed on different days, an indication of wind/gust magnitudes is obtainable.

The step response result shown in Figure 4.5 is well damped and shows a 0 – 100% rise time of 0.4 s which correlates very well with the simulated step response of 0.38 s. The NSA controller had difficulty regulating the desired acceleration level before and after the step. This is possibly as a result of the wind conditions on the flight test day. This conclusion follows from comparing Figure 4.5 and Figure 4.7 on page 39. Figure 4.7 displays the ability of the NSA controller to track the NSA command generated by the outer-loop controller which has less noise than Figure 4.5. The results in Figure 4.5 and Figure 4.7 were captured on different flight testing days. On the flight test occasion in Figure 4.7 wind-finder reported wind gust with a magnitude of 0 m/s. Note that it is unclear as to whether this was the actual wind condition for the recorded flight test data in Figure 4.7. Additionally, the flight tests were performed at different altitudes, which also plays a role. The NSA controllers had the same parameters except that the integrator pole for Figure 4.5 was 1 rad/s faster.

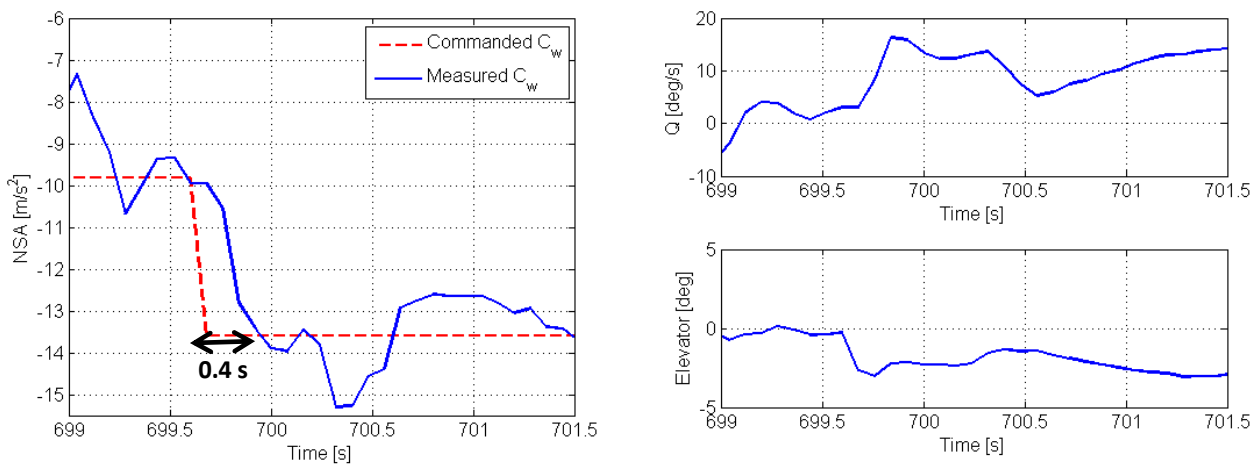


Figure 4.5 NSA Practical Step Response for the Clean Configuration

Figure 4.6 shows a satisfactory step response when considering the wind conditions. The 0 – 100% rise time is 0.46 s which correlates with the simulated step response of 0.38 s. The two step responses for the aircraft in clean and flap configurations are similar and verify the assumptions made during the design of the NSA controller.

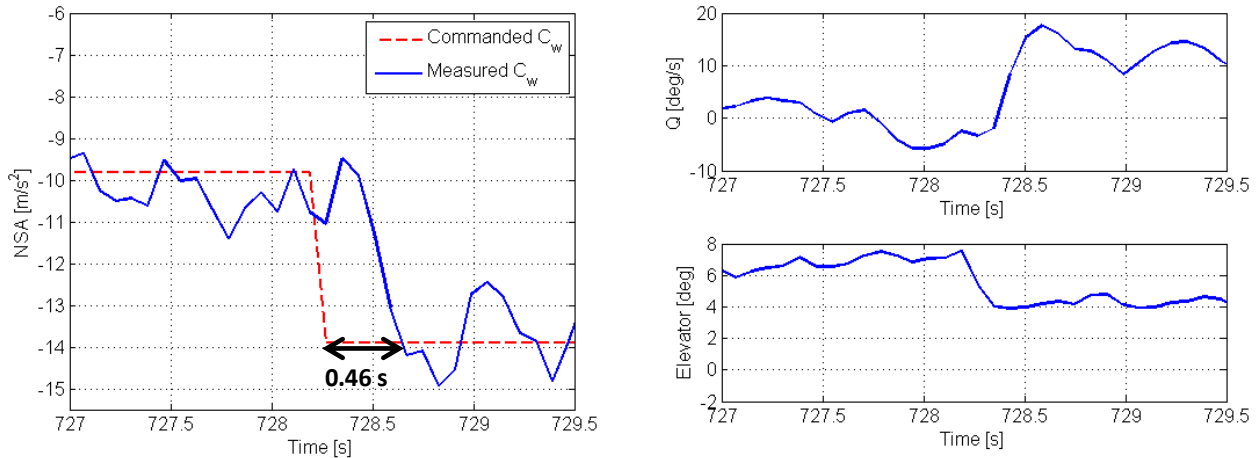


Figure 4.6 NSA Practical Step Response for the Flap Configuration

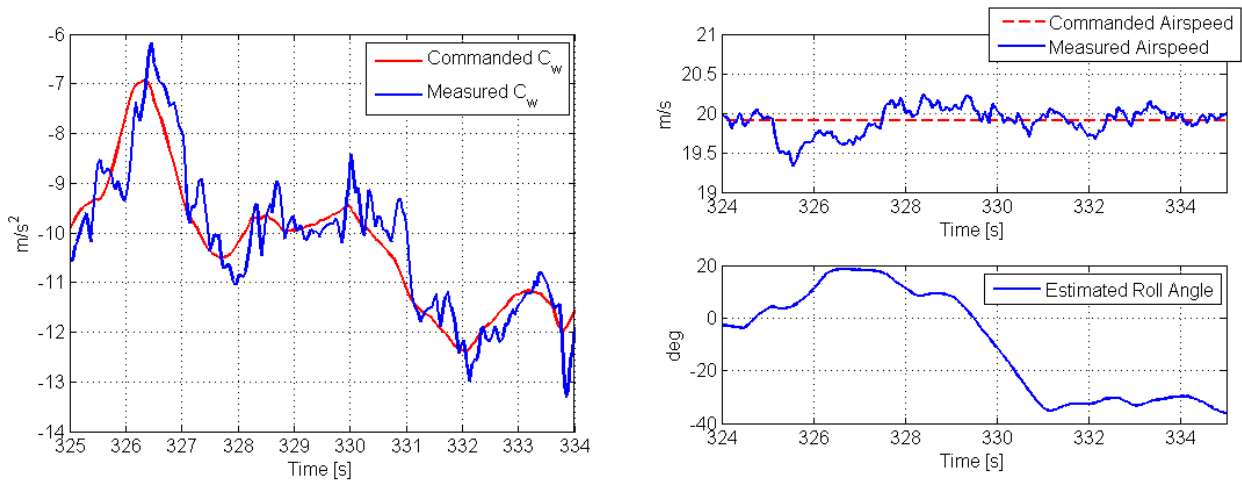
4.2.4.2 Implicitly Testing the Normal Specific Acceleration Controller

In this test the safety pilot is given control over all the aircraft's actuators except for throttle and elevator, which are commanded by the airspeed climb-rate controller during the test. Since the NSA controller is not tested directly, the aircraft is not expected to climb or descend rapidly when a climb-rate step is commanded. After manual take-off the pilot trimmed the aircraft at an altitude of 60 m. The airspeed climb-rate controller was then armed with an airspeed command of 20 m/s and a zero climb-rate command. After the aircraft stabilised a climb-rate command of -2.88 m/s was issued. The climb-rate command for this test was derived from the current climb rate minus a three meter a second climb-rate step.

For this flight test the expected 10 – 90% rise time for climb-rate command was 1.65 s, the NSA closed-loop integrator was placed at 5 rad/s and a time-scale separation distance of 2.5 existed between the two controllers. The satisfactory result, illustrated in Figure 4.7, shows that the 10 – 90% rise time of climb-rate command is 1.3 s and the peak time is 2.1 s. At 330 s the safety pilot entered a constant bank of -33° to turn the aircraft back. The outer-loop controller compensated for the disturbance in lift by increasing the lift on the main wing using the NSA controller.

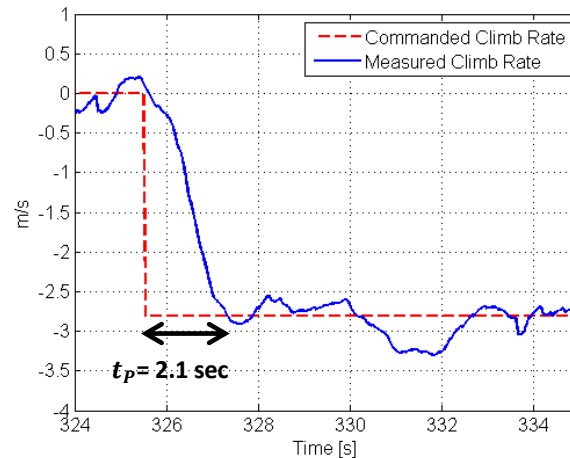
Even though there were disturbances in lift, the practical result obtained compares with the expected theoretical result. The climb-rate step was achieved with minimal perturbations in airspeed. These flight test results also show that the NSA controller tracks the reference command generated by the airspeed climb-rate controller. By increasing the time-scale separation distance

between the two controllers the closed-loop poles of the airspeed climb-rate controller are expected to become more dominant and less overshoot is expected in the NSA controller.



(a) Normal Specific Acceleration

(b) Airspeed and Estimated Roll Angle



(c) Climb Rate

Figure 4.7 Outer-Loop and Normal Specific Acceleration Controller Practical Test Results

4.3 Decoupling of Lateral Dynamics

The aircraft's lateral model in Equation (4.10) consists of the directional and roll-mode dynamics. The coupling between the directional and roll-rate dynamics are quite weak for conventional airframes and can be decoupled if the following conditions hold [1]:

$$\left| \frac{C_{n_P}}{C_{l_P}} \right| \ll \left| \frac{C_{n_R}}{C_{l_R}} \right| \quad (4.31)$$

$$\left| \frac{C_{n_P}}{C_{l_P}} \right| \ll \left| \frac{C_{n_\beta}}{C_{l_\beta}} \right| \quad (4.32)$$

$$\left| \frac{C_{n_P}}{C_{l_P}} \right| \ll \left| \frac{C_{n_{\delta_R}}}{C_{l_{\delta_R}}} \right| \quad (4.33)$$

$$\left| \frac{C_{n_{\delta_A}}}{C_{l_{\delta_A}}} \right| \ll \left| \frac{C_{n_R}}{C_{l_R}} \right| \quad (4.34)$$

$$\left| \frac{C_{n_{\delta_A}}}{C_{l_{\delta_A}}} \right| \ll \left| \frac{C_{n_\beta}}{C_{l_\beta}} \right| \quad (4.35)$$

The airframe in clean configuration satisfies the decoupling conditions listed above by a factor of more than 100 times. In the flap configuration, only the coupling lateral parameters C_{l_R} , C_{n_P} increase significantly (20 times and 30 times respectively) due to the increased lift on the main wing. The remainder of the lateral parameters in the flap configuration are of the same magnitude as the lateral parameters in the clean configuration. The aircraft in flap configuration satisfies the decoupling conditions by a factor of more than 30 times. A decoupling factor of 10 times is considered sufficient. The lateral dynamics can thus be decoupled into roll-rate and lateral-specific acceleration models. This greatly simplifies controller design since two independent controllers can be designed to regulate the roll-rate and lateral-specific acceleration. Thus in the design of the two separate controllers an assumption is made that feedback from the ailerons only affects roll-rate and feedback from the rudder affects the lateral specific acceleration.

4.4 Roll-Rate Controller

An aircraft changes its direction of travel by directing the lift of the main wing via the ailerons (in conjunction with a small change in elevator command). With this concept in mind the aim in this section is to design the roll-rate controller to regulate the aircraft's roll-rate about the velocity vector. In the next Chapter the normal specific acceleration vector direction controller (type of roll-angle controller) is designed by using a successive loop closure strategy to control the bank angle.

4.4.1 Design

The decoupled roll-rate dynamics after simplifying the lateral model in Section 4.1 are given below:

$$\dot{P} = \left[\frac{L_p}{I_x} \right] P + \left[\frac{L_{\delta_A}}{I_x} \right] \delta_A \quad (4.36)$$

$$P_W = P \quad (4.37)$$

where P is the roll-rate in body axes and P_W the roll-rate in wind axes. From the dynamics above it is clear that the simplified roll-rate dynamics consist of a single real pole. The system above is augmented with an integrator to provide infinite steady-state gain to remove steady-state errors.

$$\dot{E}_P = P_W - P_{WR} \quad (4.38)$$

The aileron control law defined below allows for full pole-placement:

$$\delta_A = -K_P P_W - K_E E_P + N_P P_{WR} \quad (4.39)$$

By substituting the aileron control law into the augmented roll-rate dynamics the resulting closed-loop system is given by

$$\begin{bmatrix} \dot{P}_W \\ \dot{E}_P \end{bmatrix} = \begin{bmatrix} \frac{L_p}{I_x} - \frac{L_{\delta_A}}{I_x} K_P & \frac{L_{\delta_A}}{I_x} K_E \\ 1 & 0 \end{bmatrix} \begin{bmatrix} P_W \\ E_P \end{bmatrix} + \begin{bmatrix} \frac{L_{\delta_A}}{I_x} N_P \\ -1 \end{bmatrix} P_{WR} \quad (4.40)$$

By calculating the characteristic equation of the closed-loop system above

$$\alpha_C(s) = s^2 + \left(\frac{L_{\delta_A}}{I_x} K_P - \frac{L_p}{I_x} \right) s + \frac{L_{\delta_A}}{I_x} K_E \quad (4.41)$$

and matching the coefficients to the desired closed-loop characteristic equation below

$$\alpha_C(s) = s^2 + \alpha_1 s + \alpha_0 \quad (4.42)$$

the control law gains can be calculated using

$$K_P = \frac{\alpha_1 I_x + L_p}{L_{\delta_A}} \quad (4.43)$$

$$K_E = \frac{\alpha_0 I_x}{L_{\delta_A}} \quad (4.44)$$

The feed-forward zero is placed by N_C

$$N_C = \frac{K_E}{z_f} \quad (4.45)$$

where z_f is the location of the desired zero.

4.4.2 Pole-Placement and Simulation

By analysing the open-loop roll-rate dynamics of Equation (4.36) over the velocity range of interest 12 to 18 m/s , the natural frequency range of the open-loop roll-rate pole was found to be between 5.62 and 8.44 rad/s . The closed-loop roll-rate pole is placed at its open-loop counterpart frequency. This design choice follows from the limitation introduced by the single sample delay of the OBC discussed in Section 4.2.2. The augmented integrator pole is also placed at a frequency slower than the open-loop roll-rate pole, based on similar arguments during the integrator pole-placement during NSA controller design:

$$p_{int} = 4.5 \text{ rad/s} \quad (4.46)$$

Based on the current integrator pole location, the remaining bandwidth for an ideal (five times) time-scale separation to an outer control loop system is not sufficient. Thus the integrator pole must be taken into account during the design of the outer-loop controller. The feed-forward zero is placed 50% higher than the integrator pole, for similar reasons to those in the design of the NSA controller in Section 4.2.2.

A linear simulated step response of the roll-rate controller is given in Figure 4.8. The resulting step response has a 10 – 90% rise time of 0.48 s and is a combination of two real poles and a feed-forward zero.

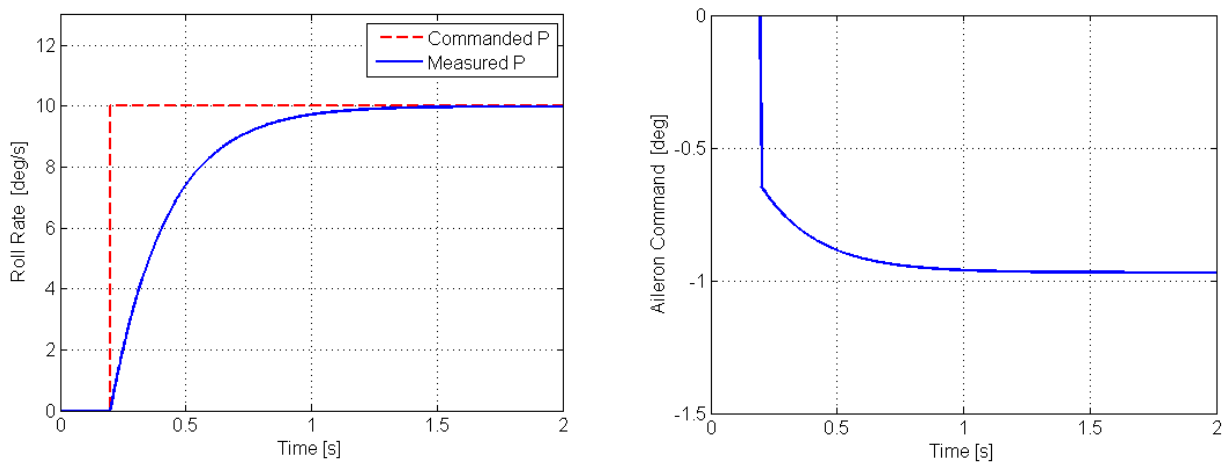


Figure 4.8 Roll-Rate Controller Linear Step Response at Trim Airspeed

4.4.3 Roll-Rate Controller Practical Flight Test

In this project the aircraft's flight envelope is non-aerobatic and the roll-rate controller is based around a well-described single real pole. With these properties of the roll-rate controller in mind, the testing approach shifted to testing the roll-rate controller implicitly. The roll-rate controller is tested implicitly via the outer-loop roll-angle controller. By implicitly testing the roll-rate controller, more flight test time can be allocated to test more important aspects of the flight control system.

For this test the safety pilot was given control over all the aircraft's actuators except for the ailerons, which were commanded by the roll-angle controller. The aircraft was expected to enter a banked turn until the safety pilot was signalled to retake full control.

The safety pilot levelled the aircraft at an altitude of 50 m. The roll-angle controller was engaged with an initial roll-angle command of 0° . After the roll-angle controller regulated the aircraft's roll-angle to zero degrees, a roll-angle step command of 10° was issued from the ground station, followed by a step command to 20° . The satisfactory result of the practical flight test is presented in Figure 4.9.

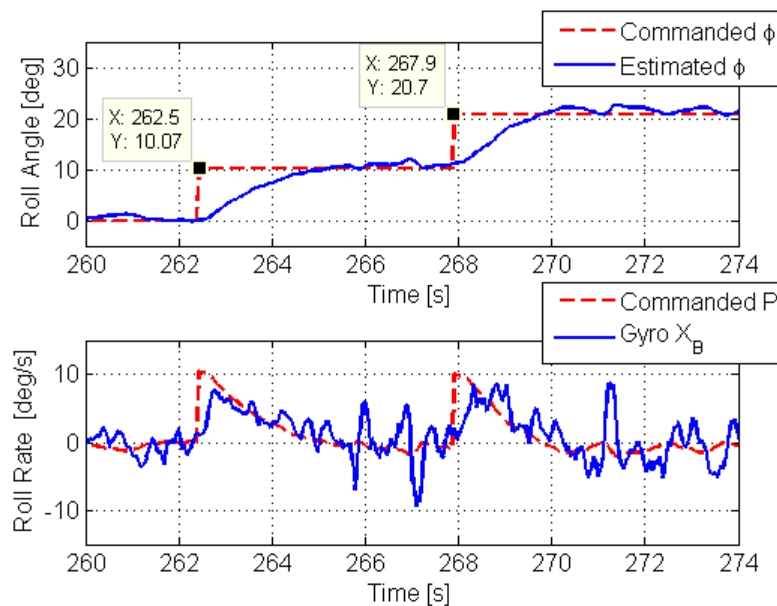


Figure 4.9 Roll-Rate Controller Practical Test Result

For this flight test the roll-rate integrator pole was placed at 3.5 rad/s , the error angle pole at 1.5 rad/s and the feed-forward zero in the design of the roll-rate controller was placed at a high frequency, effectively removing its dynamics from the closed-loop system. The outer-loop control

system is discussed in detail in Chapter 5. The roll-rate controller's analysis focuses on the expected and practical rise time results of the outer-loop controller and the ability of the roll-rate controller to track the roll-rate reference command.

The theoretical roll-angle 10 – 90% rise time is 1.7 s and the practical 10 – 90% rise is 1.8 s. The roll-rate controller tracks the generated roll-rate command relatively well, which results in a well-damped roll-angle step response. From the roll-rate response it is evident that the roll-rate controller's rise time can be reduced by placing the feed-forward zero closer to the integrator pole.

In conclusion, from an outer-loop controller perspective the inner-loop controller design is acceptable even though the step response of the inner-loop controller is not fully known. In the design of the outer-loop controller, the dynamics of the inner-loop controller were taken into account.

4.5 Lateral Stability Augmentation Controller

In flight it is desired that the Dutch roll mode of the aircraft be damped and that the aircraft fly in a coordinated manner. These two goals can be achieved by designing two separate controllers. Both of the controllers will make use of the rudder of the aircraft. The Dutch roll damper increases the damping of the Dutch roll mode and the lateral specific acceleration controller regulates the sideslip angle, β to zero. The lateral stability augmentation control architecture was used by [20], and is reused in this project.

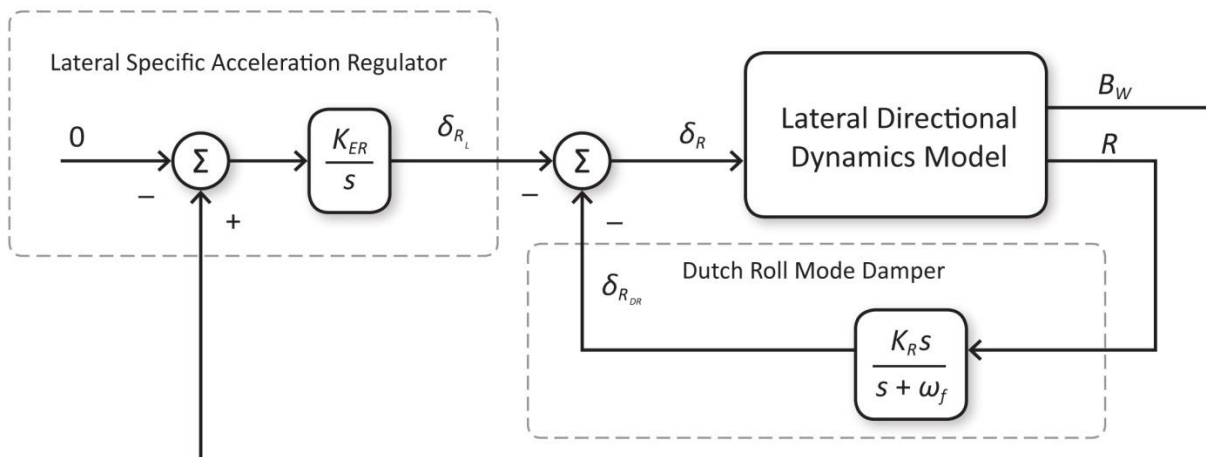


Figure 4.10 Overview of the Lateral Stability Augmentation Control Architecture

In this control architecture the Dutch roll damper supplies the high-frequency portion of the rudder control command and the LSA regulator adds the lower-frequency component of the command signal. The Dutch roll damper operates at a much higher frequency than the LSA regulator so that these two controllers are also time-scale separated. The rudder command signal in Figure 4.10 is given by

$$\delta_R = \delta_{R_{DR}} + \delta_{R_L} \quad (4.47)$$

where $\delta_{R_{DR}}$ is the high-frequency command generated by the Dutch roll damper and δ_{R_L} is the low-frequency command generated by the LSA regulator.

4.5.1 Dutch Roll Damper Design

The aim in this section is to design a Dutch roll damper that can operate separately or in conjunction with the LSA regulator. It is designed so that it uses yaw rate feedback to increase the damping of the Dutch roll mode. A high-pass filter for the yaw rate is used in the design so that the Dutch roll damper does not counter any constant turn rate motions. This conventional approach which was adapted in [20] is based on work in [27]. The transfer function for the high pass filter with the feedback gain is given by

$$D(s) = \frac{K_R s}{s + \omega_f} \quad (4.48)$$

where ω_f is the filter cut-off frequency and K_R is the feedback gain. The natural frequency and open-loop damping of the Dutch roll mode at trim airspeed is given by

$$\omega_{DR_{OL}} = 3.21 \text{ rad/s} \quad (4.49)$$

$$\zeta_{OL} = 0.157 \quad (4.50)$$

The open-loop damping of the airframe is clearly very lightly damped. The cut-off frequency must be chosen low enough so that the high frequency effects of the Dutch roll mode lies within its pass band and high enough not to counter constant turn rate motions. The cut-off frequency of the filter was chosen at a third of the natural open-loop frequency of the Dutch roll mode. A root locus plot with the filter dynamics included is shown in Figure 4.11 for a variation in the feedback gain K_R .

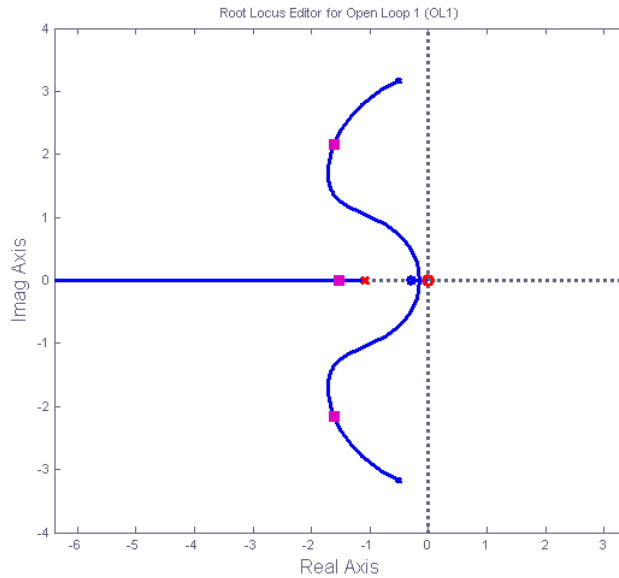


Figure 4.11 Dutch Roll Damper Root Locus Design

The feedback gain is selected so that the closed-loop damping of the Dutch roll mode is equivalent to

$$\zeta_{CL} = 0.6 \quad (4.51)$$

The transfer function of the high-pass filter with the feedback gain is given by

$$D(s) = \frac{-0.3s}{s + 1.0715} \quad (4.52)$$

In the aircraft's flight envelope, the aircraft's control system will experience a range of velocities. Since velocity acts as a global scaling factor, the poles and zeros of the lateral dynamics will also scale upwards and downwards in frequency in a similar manner to the short-period mode poles of the aircraft. As the aircraft reduces its airspeed for a landing, the fixed pole-placement strategy, as designed above, would attempt to make the aircraft respond with the same dynamics in damping the Dutch roll mode as at the aircraft's trim airspeed. A variable pole-placement strategy is thus adopted that adjusts the control gain based on the open-loop frequency of the Dutch roll mode.

$$D(s) = \frac{K'_R}{\eta_d \omega_{DR_{OL}}} \frac{s}{s + \eta_d \omega_{DR}} \quad (4.53)$$

In the transfer function above, $\omega_{DR_{OL}}$ represents the open-loop Dutch roll mode frequency, η_d is a fraction of the open-loop frequency and determines the high-pass filter's cut-off frequency and K'_R

is the normalised feedback gain. The coefficients for the transfer function above are obtained by a root locus design at the aircraft's trim velocity:

$$\dot{K}_R = -0.321 \quad (4.54)$$

$$\eta_d = 1/3 \quad (4.55)$$

The open-loop frequency for the Dutch roll mode can be determined from the characteristic equation of the decoupled LSA dynamics. The open-loop natural frequency is given by

$$\omega_{DROL} = \sqrt{\frac{1}{I_z} \left[\frac{Y_\beta}{mV} N_R + N_B - N_B \frac{Y_R}{mV} \right]} \quad (4.56)$$

Next the improvement of the stability augmentation controller is analysed in a non-linear simulation where the Dutch roll dynamics are excited by superimposing a step on the rudder control signal. Figure 4.12 illustrates the open-loop damping of the airframe and the closed-loop damping with the augmented stability controller activated. The improvement in damping with the stability controller activated can be clearly seen.

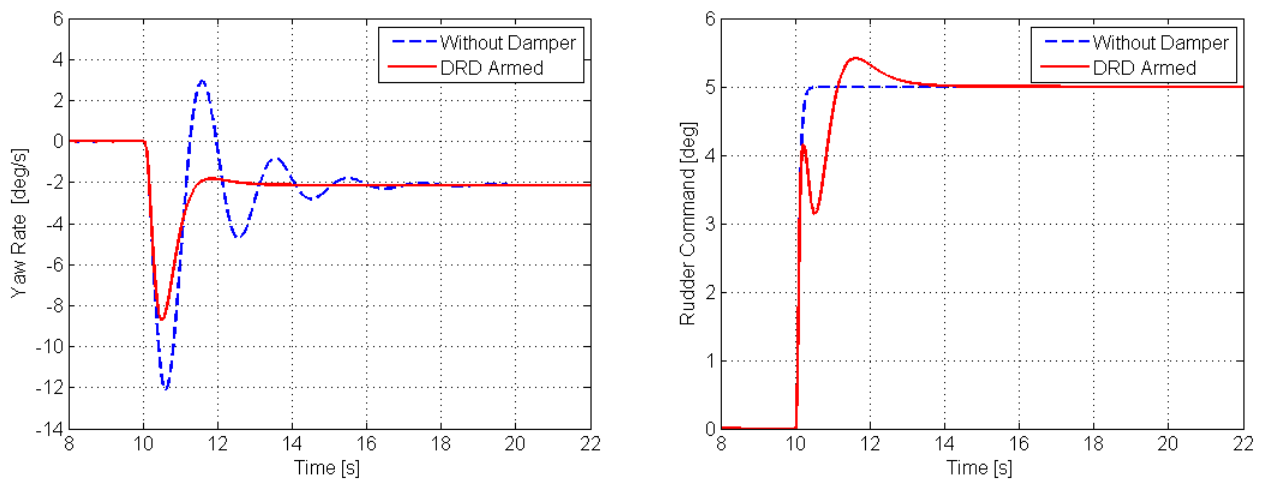


Figure 4.12 Improved Damping of the Dutch Roll Mode

4.5.2 Lateral Specific Acceleration Controller Design

The controller designed in this section regulates the side-slip angle β to zero in steady-state to aid in coordinating the aircraft's turns. Figure 4.13 illustrates a typical pole-zero map of a conventional aircraft's lateral dynamics.

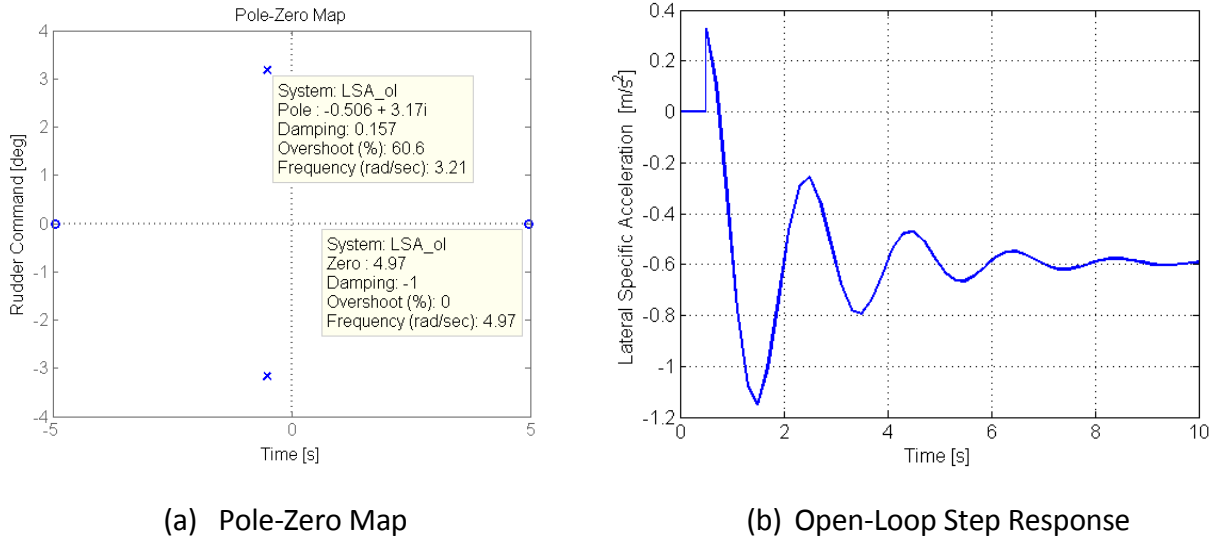


Figure 4.13 Aircraft Lateral Dynamics

From the open-loop step response above it is clear that the NMP zero has a far greater effect on the lateral dynamics than in the longitudinal dynamics. Since there is no primary lateral lifting surface, the longitudinal stability derivative $C_{L\alpha}$ is much greater in magnitude than the lateral stability derivative $C_{Y\beta}$. Thus the induced lateral force due to rudder deflection is far greater than the lift produced by an elevator deflection.

Since the NMP zero is at a slightly higher frequency than the Dutch roll mode poles, the design approach to ignore the NMP effect that was used in the design of the NSA controller is not valid in the design of the LSA regulator since the natural frequency is not three times slower than the NMP zero. Consequently [1] proposes a time-scaled separated LSA controller that operates with a far lower bandwidth than the Dutch roll damper. With the time-scale separation in place, the full dynamic model from rudder to lateral specific acceleration can be approximated by a steady-state gain.

$$B_W \approx K_{SS} \delta_{RR} \quad (4.57)$$

where δ_{RR} is the rudder deflection commanded by the LSA regulator. The steady-state gain is determined from the transfer function of the rudder to lateral specific acceleration given in [1] as

$$K_{SS} = \frac{Y_{\delta_R} Y_{\beta}}{m I_Z} \left(\frac{N_{\beta}}{Y_{\beta}} - \frac{N_{\delta_R}}{Y_{\delta_R}} \right) \frac{1}{(\omega_{DR})^2} \quad (4.58)$$

The design of the LSA controller consists of a single slow integrator pole. This strategy ensures that the closed-loop system is less sensitive to parameter uncertainty in Equation (4.58) and that it dominates the response of the LSA controller. The integrator pole is augmented to the lateral dynamics:

$$\dot{E}_B = B_W - B_{WR} \quad (4.59)$$

where B_{WR} is the lateral specific acceleration command, the control law is defined as

$$\delta_{RR} = -K_E E_B \quad (4.60)$$

The closed-loop dynamics are obtained by substituting (4.60) into (4.59)

$$\dot{E}_B = [-K_{SS}K_E]E_B - B_{WR} \quad (4.61)$$

With the closed-loop and desired characteristic equations given as

$$s + K_{SS}K_E = 0 \quad (4.62)$$

and

$$\alpha_c(s) = s + \alpha_0 \quad (4.63)$$

respectively, the integrator pole can be placed by solving for the feedback gain as follows:

$$K_E = \frac{\alpha_0}{K_{SS}} \quad (4.64)$$

The integrator pole is placed as a function of the open-loop Dutch roll natural frequency to enforce a constant time-scale separation between the Dutch roll damper the LSA controller:

$$p_i = -n_i \omega_{DR} \quad (4.65)$$

with n_i specifying the separation distance and chosen to be

$$n_i = 1/10 \quad (4.66)$$

With the stability augmentation controller designed the response to a disturbance can be analysed. The same rudder disturbance that was superimposed on the rudder control signal to analyse the Dutch roll damper is reused. Figure 4.14 shows how the lateral stability augmentation controller damps the Dutch roll mode and regulates the lateral specific acceleration to zero. With reference to the yaw rate graph, it can be seen that the damping of the Dutch roll controller has slightly decreased. This is due to a shift in closed-loop pole locations by adding the LSA regulator and is caused by inaccuracies introduced by the time-scale separation between the Dutch roll damper and LSA regulator. Lastly, the fast Dutch roll response and the slow LSA controller response are also visible.

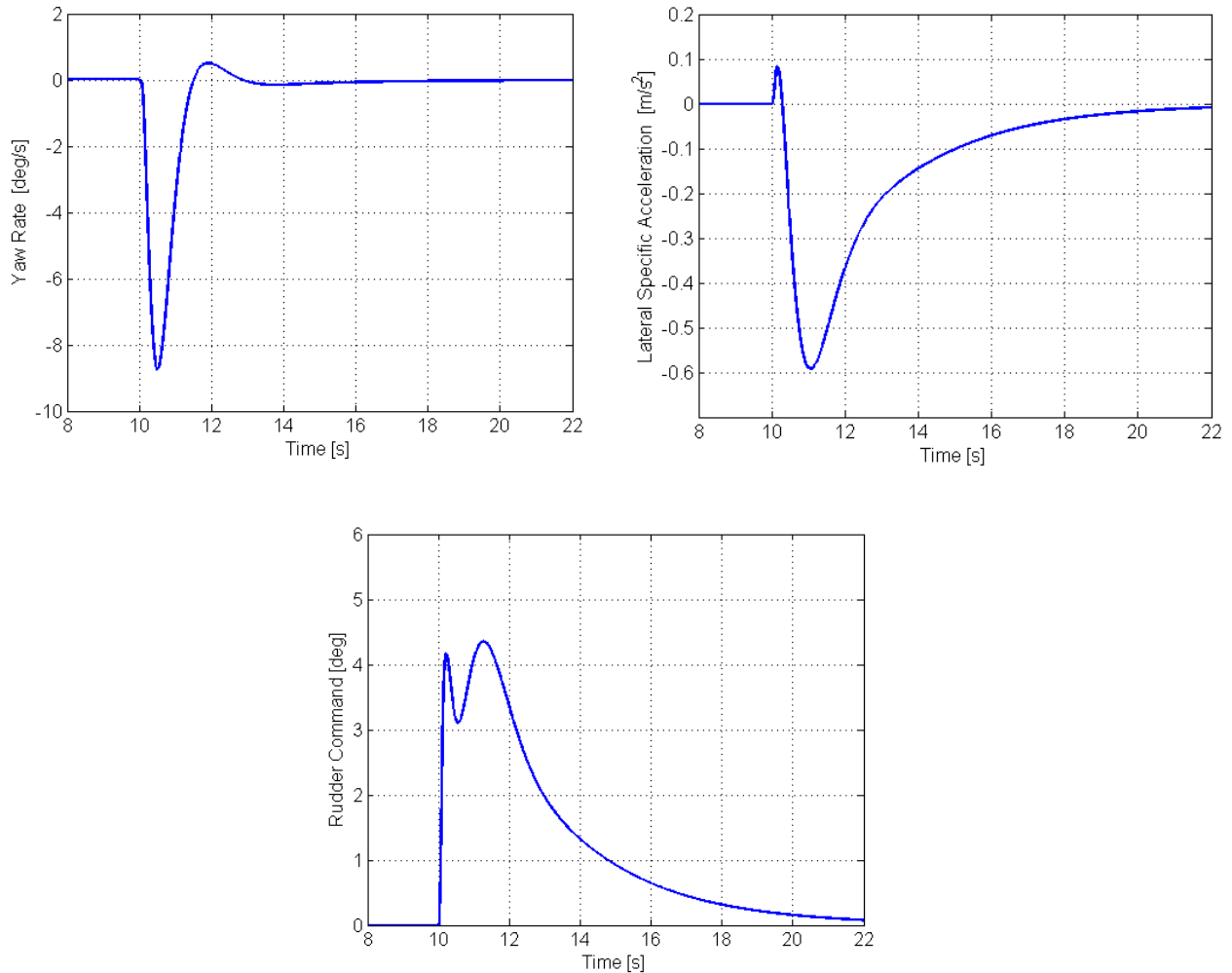


Figure 4.14 Lateral Stability Augmentation Controller Response to a Step Disturbance

4.5.3 Lateral Stability Augmentation Controller Summary

In the non-acrobatic flight envelope of this project the rudder would only be used for side-slip manoeuvres in a crosswind landing. During flight tests it was noticed that the pilot rarely used the rudder, since the aircraft will naturally weathervane into the incoming wind and flies turns that are very close to coordinated as a result of the relatively big fin.

In the analysis of the lateral stability augmentation controller, where the Dutch roll damper and the LSA regulator worked together to reject a disturbance, it was found that the LSA regulator removed some of the damping of the Dutch roll mode. Thus it is better to use either only the full lateral stability augmentation controller or only the Dutch roll damper.

The natural damping of the Dutch roll mode is lightly damped, but stable; thus the aircraft is still flyable without enabling the Dutch roll damper or the LSA controller.

4.5.4 Lateral Stability Augmentation Controller Practical Flight Test

4.5.4.1 Dutch Roll Damper Flight Test

The Dutch roll damper was verified in a flight test by exciting the Dutch roll mode by perturbing the rudder and by observing the resulting yaw rate. The flight test procedure outlined in the next paragraph was used to obtain the results presented in Figure 4.15 and Figure 4.16.

In this flight test the safety pilot had complete control over the aircraft. The rudder signal of the pilot was added to the Dutch roll damper control signal. Thus the pilot could issue rudder commands while the controller actively damped any unwanted Dutch roll effects. At a low altitude of 25 *m* the pilot was instructed to “perturb” the rudder on two separate fly-bys until the Dutch roll mode could be seen visually. In this particular test case an altitude of 25 *m* is considered safe since the Dutch roll mode of the aircraft is lightly damped and not unstable and the pilot has full control. Additionally, it was also important to be able to see the Dutch roll mode of the aircraft so the test altitude chosen could not be too high. On the first fly-by the aircraft’s Dutch roll mode was excited without any control and on the second fly-by the Dutch roll damper was activated.

Figure 4.15 shows the first fly-by result, where the lightly damped Dutch roll mode of the aircraft can be seen clearly in the yaw rate. Special attention should be given to the section after the broken line in Figure 4.15 where the pilot gives a zero rudder command. In this section the characteristic damping damps out the Dutch roll mode oscillations. The result of the second fly-by with the Dutch roll damper armed is illustrated in Figure 4.16. It can be clearly seen that the yaw rate is reduced even though the pilot is using the maximum rudder deflections. When the pilot gives a zero rudder command the controller damps out the unwanted oscillations much faster than in the open-loop case. Additionally, the lateral specific acceleration resulting from rudder deflections is lower than in the open-loop case. The practical result obtained verifies the functionality of the controller.

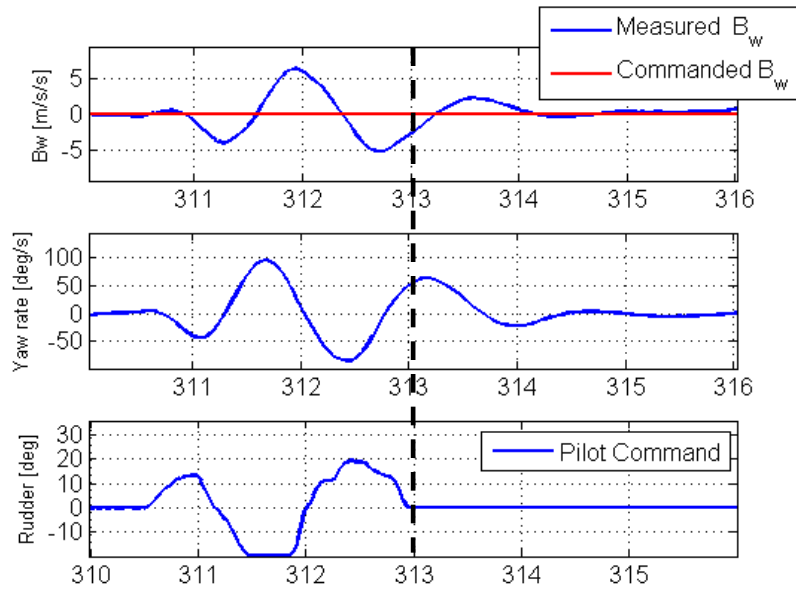


Figure 4.15 Open-Loop Practical Response of the Dutch Roll Mode

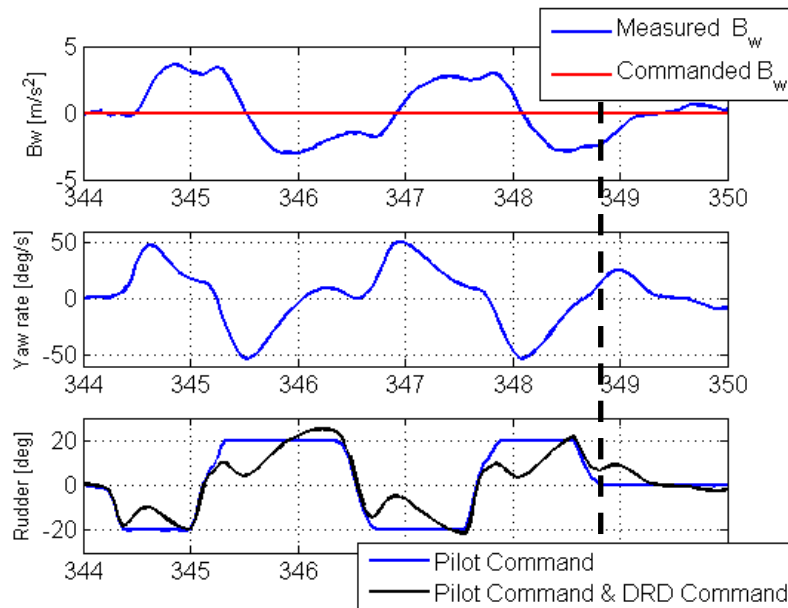


Figure 4.16 Closed-Loop Practical Response of the Dutch Roll Damper

4.5.4.2 Lateral Specific Acceleration Regulator Test

For the lateral specific acceleration controller test, the pilot had full control over the aircraft except for the rudder. Since the aircraft was already flying in a coordinated manner, a test where the LSA regulator would only regulate the aircraft side-slip to zero would yield no practical result, except to show that the controller was stable. One way of testing the LSA controller is to command a small step in lateral specific acceleration that would purposefully enter the aircraft in a side-slip manoeuvre.

With this test approach in mind, during the flight test the safety pilot levelled the aircraft at an altitude of 25 m as in the DRD damper test, and then on the first fly-by the LSA regulator was armed. Seconds after the flight test commenced the aircraft started oscillating slowly and these oscillations grew larger over time. This result is illustrated below in Figure 4.17. Note that the LSA regulator also excites the Dutch roll mode.

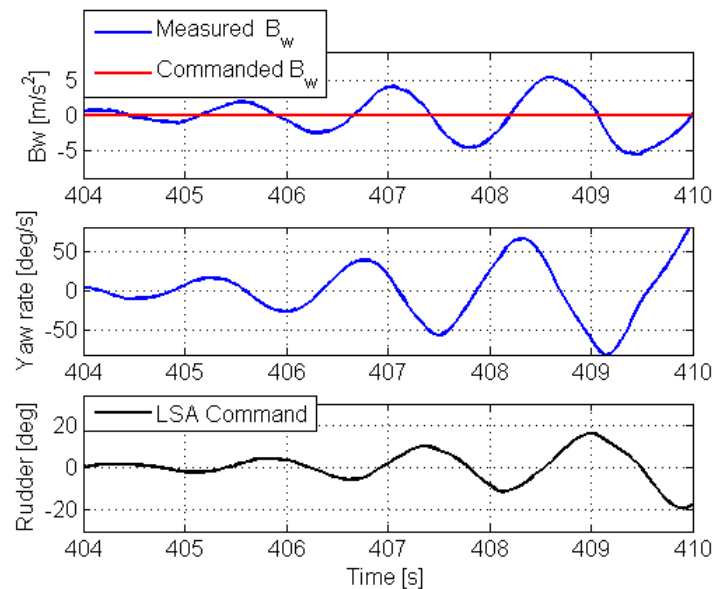


Figure 4.17 Practical Unstable Response of the Lateral Specific Acceleration Regulator

This exact flight test was performed in an HIL simulation with a satisfactory outcome. In finding the difference between the real world and the simulation environment, the focus was shifted from looking for an error in the design of the controller to looking for an error in the lateral parameters of the aircraft. The lateral aerodynamic model of the aircraft was compared to existing aerodynamic models used in the ESL for aircraft of similar size and build. The $C_{Y\beta}$ parameter that AVL calculated for the aircraft used in this project was found to be four times smaller than that of a similar aircraft.

This aircraft was used in a previous ATOL project. An HIL simulation was performed with the controller gains exactly the same as on flight test day, and in the non-linear simulation environment the aircraft's $C_{Y\beta}$ was made four times larger. The simulation results were similar to the actual flight test data presented in Figure 4.17. The HIL simulation results can be interpreted as follows:

During the practical flight test the LSA regulator deflected the rudder to regulate the lateral specific acceleration which caused an unmodelled side force. This resulted in an unwanted acceleration that the LSA regulator tried to regulate to zero by generating an opposite lateral specific acceleration via the rudder. The controller succeeded in generating an opposite acceleration; however the resulting counter-acceleration was bigger in magnitude than the original acceleration being countered. Now the LSA controller realised that the aircraft was accelerating in the wrong direction and generating another acceleration via the rudder to counter the excessive counter-acceleration.

Due to limited flight test time the LSA controller was not re-tested to determine its performance. Even though the LSA regulator was not used in an autonomous landing test, this was an excellent control exercise!

4.6 Review of the Inner-Loop Controllers

In the next chapter the slower outer-loop controllers are designed based on the fast inner-loop controllers via the time-scale separation strategy. The design concept is illustrated in Figure 4.18. The next paragraph gives a brief summary of the inner-loop closed-loop pole locations and design considerations for the outer-loop controllers.

During the design of the NSA controller the bandwidth remaining after placing the closed-loop integrator pole at 6 rad/s allows for the fastest outer-loop controller dynamics to be placed at 1.2 rad/s . This ideal time-scale separation margin of five times constrains the performance outer-loop controller. To increase the outer-loop controller's performance, two strategies can be employed: in the first strategy a lower time-scale separation distance between the NSA controller and outer-loop controller can be used, and in the second strategy the dynamics of the NSA controller can be taken into account in the design of the outer-loop controller. The first and simplest strategy, investigated in Section 4.2.4, was employed. In the design of the roll-rate controller a time-scale separation would severely constrain the outer-loop controller's performance, thus the roll-rate dynamics were taken into account during the design of the outer-loop controller.

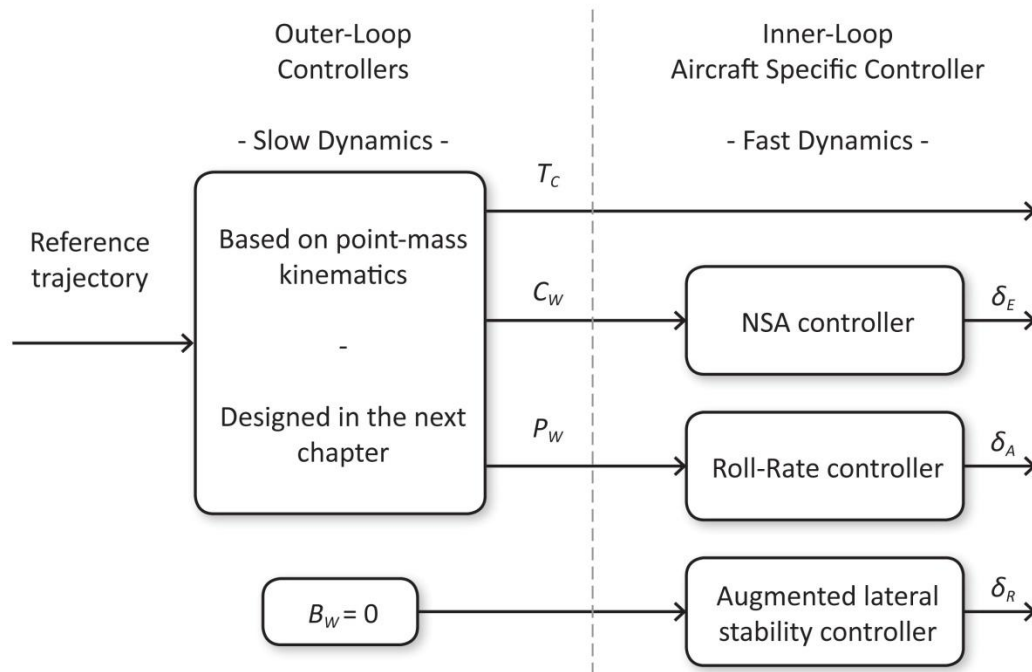


Figure 4.18 Block Diagram Overview of the Flight Control System

4.7 Summary

In this chapter the fast dynamics of the aircraft were investigated and inner-loop controllers were designed. The inner-loop controllers simplify the aircraft to a point-mass that is controlled by specifying a normal acceleration and a roll-rate. An additional stability controller was also designed to damp the Dutch roll mode of the aircraft and to regulate the side-slip angle to zero.

The flight test results are similar to the non-linear simulation results which verifies the non-linear model of the aircraft developed through the course of this project. Additionally, these results also indicate that the simulation environment describes the real world with sufficient accuracy for controller testing.

A time-scale separation distance of 2.5 times between the NSA controller and outer-loop controller was found to yield acceptable performance. A satisfactory performance was also obtained for the roll-rate controller and Dutch roll damper. With the LSA controller only partially verified and not a necessity, only the Dutch roll damper was used throughout the remainder of flight tests.

Chapter 5

Outer-Loop Flight Control System

In Chapter 4, an interface was established that encapsulates all the aircraft's model uncertainties and that also reduced the aircraft to a point-mass with a velocity vector and a roll-rate. In this chapter the aim is to design outer-loop controllers to control the point-mass dynamics of the aircraft. The outer-loop control architecture controls the longitudinal and lateral motion of the point-mass separately.

The longitudinal control architecture regulates the aircraft's airspeed and altitude. This control architecture makes use of a multiple-input/multiple-output (MIMO) airspeed climb-rate controller and a proportional altitude controller. The main aim of the lateral control architecture is to navigate the airplane to selected waypoints. This architecture employs a normal specific acceleration vector direction controller (NSAVDC) to regulate the aircraft's bank angle. The guidance controller uses the NSAVDC to steer the aircraft on the desired flight trajectory.

In the practical flight test section after the theoretical design of each controller, the flight testing approach is stated, followed by the expected outcome, followed by the flight test data analysis and the conclusion.

5.1 Longitudinal Control Architecture

5.1.1 Airspeed and Climb-Rate Controller

The pitch attitude of the aircraft is regulated by controlling the airspeed and climb rate via the elevator and engine power. In the longitudinal aircraft motion of the aircraft there exists a well-known coupling between airspeed and climb rate. A simple control strategy would be to divide the controller design into separate airspeed and climb-rate controllers. This control strategy would effectively use the throttle to control the airspeed, and the elevator to control the climb-rate. This SISO strategy ignores the coupling between the airspeed and climb rate. Intuition leads one to expect that this approach will not perform well, so a multivariable linear quadratic regulator (LQR) control system was employed in this project. The LQR is additionally suited to this project since all

the aircraft states are either measured or estimated which enables full-state feedback. The airspeed climb-rate control system is conceptually illustrated in the block diagram shown in Figure 5.1.

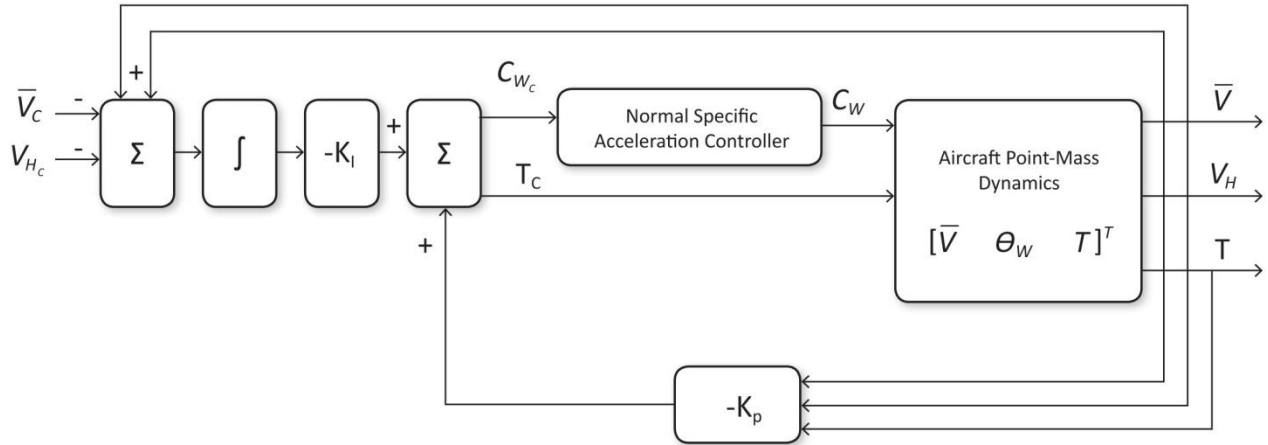


Figure 5.1 Airspeed & Climb-Rate Controller

Here \bar{V}_C is the commanded airspeed, \bar{V} the airspeed, V_{Hc} the commanded climb rate, V_H the measured climb rate, T_C the commanded thrust command, C_{Wc} the commanded normal specific acceleration and C_W the measured normal specific acceleration. The LQR controller uses integrator and proportional feedback gain matrixes K_I and K_P respectively to regulate the state vector. In the block diagram above, the NSA controller is used as a virtual actuator. To simplify the design of the LQR controller, it is assumed that after the LQR controller issues an NSA command, the NSA controller will respond immediately and attain the desired normal specific acceleration. This assumption was initially verified by simulation through various time-scale separation frequencies (five times being ideal). In a practical sense, good results were obtained as shown in Chapter 4, with a time-scale separation distance of 2.5 times. The NSA controller is thus modelled as a unity gain function in Figure 5.1. With the goal of this section abstracted in Figure 5.1, the derivation of the MIMO controller follows. The aircraft's point-mass dynamics are restated below from Section 3.3 along with the axial acceleration equation from Section 4.1.

$$\dot{\bar{V}} = A_W - g \sin \theta_W \quad (5.1)$$

$$\dot{\theta}_W = -\left(\frac{C_W + g \cos \theta_W}{\bar{V}}\right) \quad (5.2)$$

$$\dot{N} = \bar{V} \cos \theta_W \quad (5.3)$$

$$\dot{D} = -\bar{V} \sin \theta_W \quad (5.4)$$

$$A_W = \frac{1}{m} T - \frac{qS}{m} C_D \quad (5.5)$$

Equation (5.1) relates the change in airspeed to the axial acceleration of the aircraft and a gravity coupling term. Equation (5.2) relates the change in the aircraft's pitch angle coordinated in the wind axis as a function of the aircraft's normal acceleration, airspeed and a gravity coupling term. By substituting the axial acceleration Equation (5.5) into Equation (5.1) the resulting velocity dynamic equation can be written as

$$\dot{\bar{V}} = \frac{T - qSC_D}{m} - g \sin \theta_W \approx \frac{T}{m} - g \sin \theta_W \quad (5.6)$$

Aerodynamic drag is typically difficult to model. A simplification is made in Equation (5.6) to treat drag as a disturbance force by modelling it directly. For this simplification the low-frequency drag disturbance force is removed by the control system by using an augmented integrator. The high frequency drag component (dynamic drag) due to a change in the aircraft lift force and will be naturally filtered through the integration process from axial acceleration to velocity magnitude [1].

To form a linear plant model, the point-mass Equations of (5.6) and (5.2) are linearised about a straight-and-level flight condition. The result is stated below and augmented with the first order propulsion model defined in Equation (4.6).

$$\begin{bmatrix} \dot{\bar{V}} \\ \dot{\theta}_W \\ \dot{T} \end{bmatrix} = \overbrace{\begin{bmatrix} 0 & -g & \frac{1}{m} \\ \frac{2g}{\bar{V}_0^2} & 0 & 0 \\ 0 & 0 & -\frac{1}{\tau_T} \end{bmatrix}}^{A_c} \begin{bmatrix} \bar{V} \\ \theta_W \\ T \end{bmatrix} + \overbrace{\begin{bmatrix} 0 & 0 \\ -\frac{1}{\bar{V}_0} & 0 \\ 0 & \frac{1}{\tau_T} \end{bmatrix}}^{B_c} \begin{bmatrix} C_{WC} \\ T_C \end{bmatrix} \quad (5.7)$$

In straight-and-level flight the trim pitch angle θ_{W_0} is zero and the cruising airspeed is \bar{V}_0 . With reference to Figure 5.1, the aim is to design an LQR controller with a state vector \mathbf{x} that consists of the aircraft's airspeed, climb rate and thrust states, $[\bar{V} \ V_H \ T]^T$. The current state \mathbf{x}_c vector consists of $[\bar{V} \ \theta_W \ T]^T$. The key to transform θ_W to V_H is given in Equations (5.3) and (5.4). The following transformation matrix can be constructed by rewriting and linearising Equations (5.3) and (5.4) and by augmenting the thrust state:

$$\begin{bmatrix} \overline{V} \\ V_H \\ T \end{bmatrix} = \begin{bmatrix} 1 & 0 & 0 \\ 0 & -\overline{V}_0 & 0 \\ 0 & 0 & 1 \end{bmatrix} \begin{bmatrix} \overline{V} \\ \theta_W \\ T \end{bmatrix} \quad (5.8)$$

$$\mathbf{x} = \mathbf{T}\mathbf{x}_c \rightarrow \dot{\mathbf{x}} = \mathbf{T}\dot{\mathbf{x}}_c \quad (5.9)$$

With the transformation matrix defined in Equation (5.8) and the transformation method defined in Equation (5.9), the state-space representation of Equation (5.7) is transformed to the desired state space representation as follows:

$$\dot{\mathbf{x}} = \mathbf{T}\mathbf{A}_c\mathbf{T}^{-1}\mathbf{x} + \mathbf{T}\mathbf{B}_c\mathbf{u} \quad (5.10)$$

$$\mathbf{y} = \mathbf{C}\mathbf{T}^{-1}\mathbf{x} \quad (5.11)$$

The system resulting in Equation (5.10) is augmented with integrators for airspeed and climb rate. The augmented states are stated below:

$$\dot{E}_{\overline{V}} = \overline{V} - \overline{V}_C \quad (5.12)$$

$$\dot{E}_H = V_H - V_{H_C} \quad (5.13)$$

The complete augmented system resulting from state transformation and integrator augmentation is given below:

$$\begin{bmatrix} \dot{\overline{V}} \\ \dot{V}_H \\ \dot{T} \\ \dot{E}_{\overline{V}} \\ \dot{E}_H \end{bmatrix} = \begin{bmatrix} 0 & -\frac{g}{\overline{V}_0} & \frac{1}{m} & 0 & 0 \\ \frac{2g}{\overline{V}_0} & 0 & 0 & 0 & 0 \\ 0 & 0 & -\frac{1}{\tau_T} & 0 & 0 \\ 1 & 0 & 0 & 0 & 0 \\ 0 & 1 & 0 & 0 & 0 \end{bmatrix} \begin{bmatrix} \overline{V} \\ V_H \\ T \\ E_{\overline{V}} \\ E_H \end{bmatrix} + \begin{bmatrix} 0 & 0 \\ -\frac{1}{\overline{V}_0} & 0 \\ 0 & \frac{1}{\tau_T} \\ 0 & 0 \\ 0 & 0 \end{bmatrix} \begin{bmatrix} C_{W_C} \\ T_C \end{bmatrix} \quad (5.14)$$

$$+ \begin{bmatrix} 0 & 0 \\ 0 & 0 \\ 0 & 0 \\ -1 & 0 \\ 0 & -1 \end{bmatrix} \begin{bmatrix} \overline{V}_C \\ V_{H_C} \end{bmatrix}$$

5.1.1.1 Linear Quadratic Regulator Design

In the previous section the linearised aircraft equations were derived. This section covers the LQR controller design. LQR is an optimal control strategy which attempts to find a controller that offers the best performance with a given measure of performance [28]. The LQR algorithm achieves this goal by trying to find a balance between the amount of energy in the state error (the system states) and energy in the control signal. For example: by decreasing the energy in the state error a large control signal is required and by decreasing the control signal energy a larger state error will result. The LQR design is performed by minimising the following cost function

$$J = \int_0^{\infty} [x^T Q x + u^T R u] dt \quad (5.15)$$

In the cost function above, Q is an $l \times l$ symmetric positive definite state weighting matrix, and R is an $n \times n$ symmetric positive definite control weighting matrix. Bryson's rule provides a good starting point for the design matrices Q and R . Increasing a state's weighting via Q it is considered expensive in the cost function; the LQR algorithm calculates feedback gains to control the state more aggressively to reduce the state's cost in the performance index. Bryson's rule uses diagonal design matrices with the following form:

$$Q = \text{diag}[Q_{\bar{v}} \quad Q_{V_H} \quad Q_T \quad Q_{E\bar{v}} \quad Q_{E_{V_H}}] \quad (5.16)$$

$$R = \text{diag}[Q_{C_W} \quad Q_{T_C}] \quad (5.17)$$

The elements in the design matrices are chosen as the square of the inverse of the maximum desired deviation from the steady-state value. The elements in the design matrix have the following form:

$$Q_x = \frac{1}{(\text{max deviation in } x \text{ from steady state})^2} \quad (5.18)$$

As mentioned earlier, Bryson's rule is used as a starting point. Initial variances are entered into the design matrices and the LQR algorithm returns a set of optimal feedback gains for the specified Q and R matrices. Even though the closed-loop dynamic response is stable, the resulting response is not as desired. The design of the LQR thus becomes a trial-and-error design in Matlab using the `lqr.m` function. For the Q matrix the following maximum deviations in airspeed, climb rate, thrust and error in airspeed and climb rate from steady-state were chosen to be 0.6 m/s , 0.25 m/s , 1 N , 0.2 m/s and 0.1 m/s respectively. For the R design matrix the maximum deviations in normal

specific acceleration and thrust were chosen to be 0.3 m/s^2 and 0.6 N respectively. During the design of the \mathbf{Q} and \mathbf{R} matrices the following limitations were kept mind:

- In the landing phase of the aircraft, climb-rate regulation was considered more important than airspeed regulation. This design choice is based on tight altitude regulation during the landing phases which also indirectly regulates the sink rate of the aircraft for a gentle touchdown.
- By decreasing the maximum deviation in airspeed and climb rate and/or by increasing the maximum deviation in normal specific acceleration and thrust, the LQR algorithm returns closed-loop poles allocated at higher frequencies. The ideal time-scale separation (five times) allows the outer-loop controller to be designed independently of the inner-loop controller's dynamics. Practical flight tests in Section 4.2.4.2 showed that a time-scale distance of 2.5 results in overshoot in the NSA controller and faster than expected outer-loop controller performance. To reduce overshoot in the NSA controller and to make the LQR controller poles more dominant, the maximum deviation in normal specific acceleration and thrust were decreased from 0.4 m/s^2 and 0.7 N to 0.3 m/s^2 and 0.6 N respectively.
- Since all the dynamics of the aircraft are encapsulated behind the NSA controller, the airspeed and climb-rate controller was linearised about a single trim velocity. A sensitivity analysis was performed to analyse the closed-loop pole locations of the MIMO controller system at different airspeeds with the feedback gains calculated for the trim velocity case. The sensitivity analysis showed a small and acceptable variation in closed-loop pole locations over the velocity range of operation. A gain-scheduling strategy was thus not deemed necessary. The trim airspeed was chosen as 15 m/s . Thus, the closed-loop poles will be optimal when the aircraft is on landing approach at trim airspeed and suboptimal at higher velocities.

The linear closed-loop step response is illustrated in Figure 5.2. The climb-rate step has a fast rise time up to 90% after which it slows down and settles slowly. The reason for this behaviour is that the gain from thrust to airspeed is about six times smaller than the coupling from climb-rate to airspeed. The LQR algorithm realises this and uses the coupling from climb rate to airspeed to regulate the aircraft's airspeed. Note that if the aircraft were lighter the gain from thrust to airspeed would increase and the LQR controller would tend to make more use of the throttle to regulate the airspeed. In this case the climb-rate step response would look more like the airspeed step response.

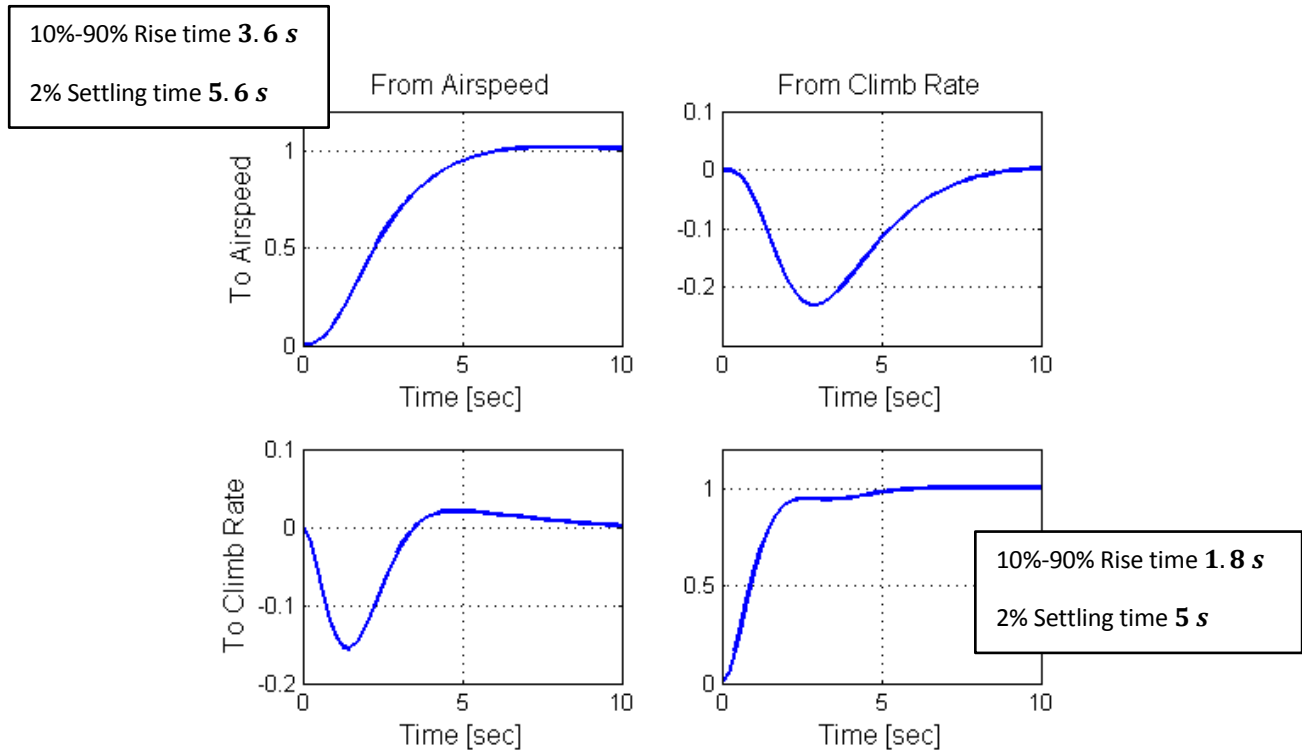


Figure 5.2 Airspeed Climb-Rate Controller Linear Step Responses

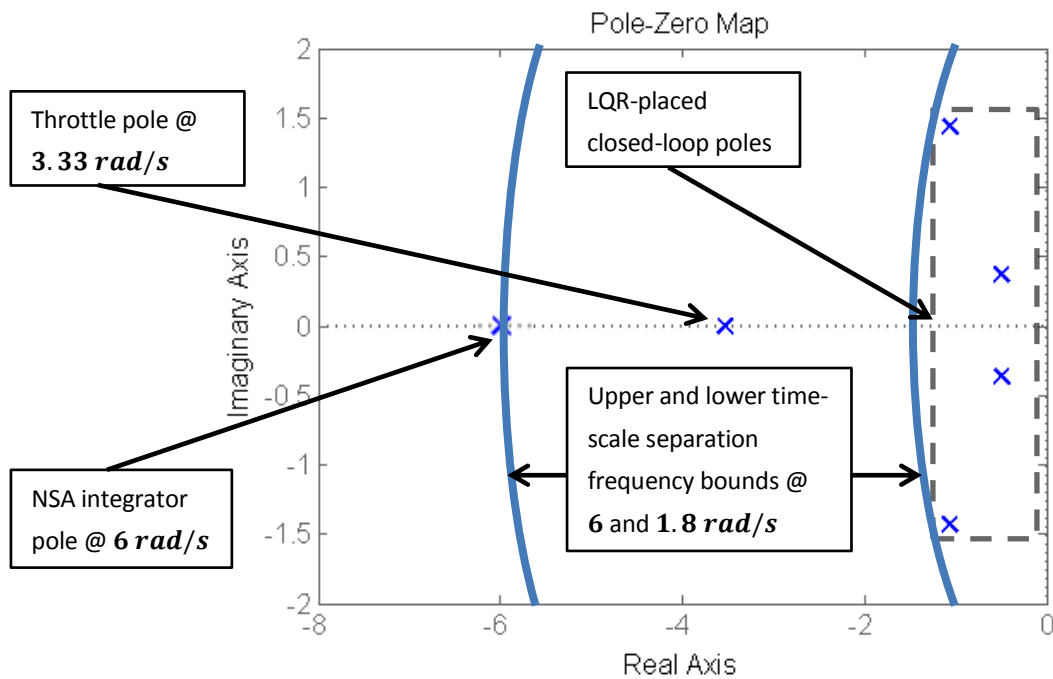


Figure 5.3 Airspeed Climb-Rate Controller Close-Loop Pole Locations at Trim Airspeed

Figure 5.3 illustrates the close-loop pole locations that the LQR algorithm generated with the \mathbf{Q} and \mathbf{R} design matrices with the time-scale frequency separation boundaries. A time-scale separation factor of 3.33 was achieved in the design.

5.1.2 Altitude Controller

With the design of the airspeed climb-rate controller completed, the focus shifts to the design of an altitude controller. In Figure 5.4, the altitude controller is designed to generate a climb-rate command from the altitude error signal (multiplied by a feedback gain). The altitude error signal is generated by integrating the climb-rate signal of the aircraft and then subtracting it from the reference altitude. The extra integrator is added naturally as a result of the height state. No extra control effort is required to maintain a specific altitude with zero steady-state error (type one system) if there is no bias on the climb-rate signal. This method of design eases the design process of the altitude controller, since all the dynamics of the aircraft are already encapsulated in the airspeed and climb-rate controller. To summarise: the altitude controller forms the top level of control with the LQR as middle-loop controller and the NSA controller as the lowest level of control.

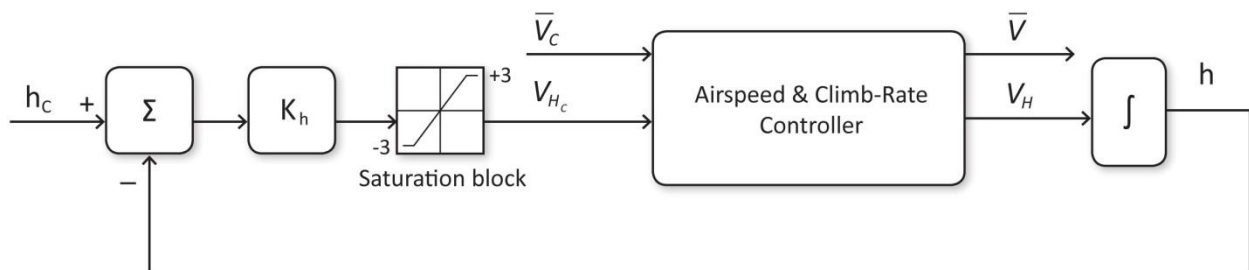
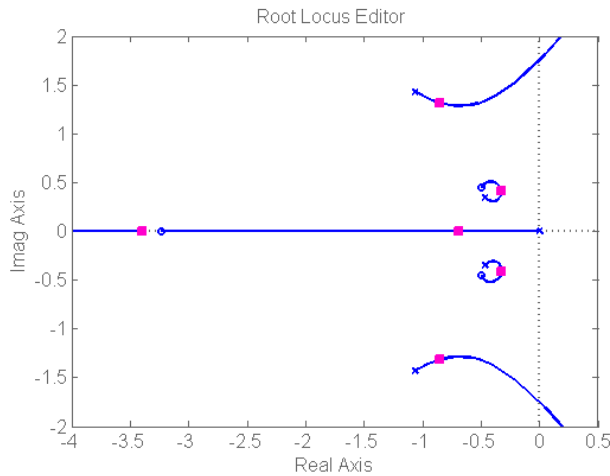


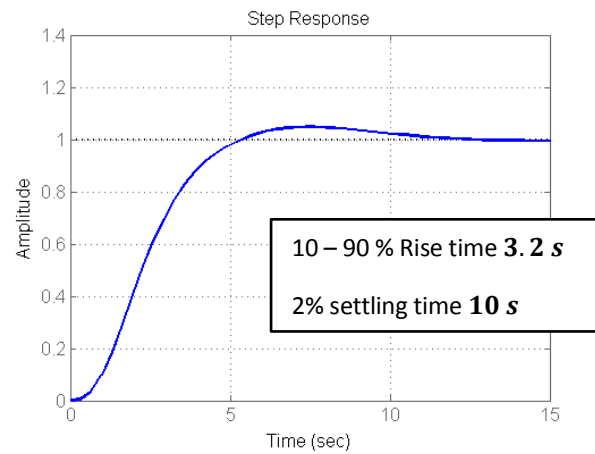
Figure 5.4 Altitude Controller Block Diagram

In Figure 5.4, h_c is the altitude command in metres, K_h the proportional altitude feedback gain and V_{HRef} is the trajectory reference climb-rate input. The longitudinal control strategy in Figure 5.4 forms a type one system, thus the system will track an altitude ramp input with a constant error. However, by introducing the reference climb-rate, the constant altitude ramp tracking error is reduced to near zero. Before the climb-rate command is sent to the airspeed climb-rate controller it is sent through a saturation block to ensure that it does not command climb-rates in excess of $\pm 3 \text{ m/s}$. This saturation block ensures that the aircraft enters a constant climb rate if large step commands are issued. Figure 5.5 (a) shows a variation in closed-loop pole locations for a change

in K_h . With reference to the root locus plot, one extra pole is added due to the integrator and the remainder were placed by the LQR strategy.



(a) Root Locus Design



(b) Linear Altitude Step Response

Figure 5.5 Altitude Controller Design

A proportional gain of

$$K_h = 0.42 \quad (5.19)$$

was found to yield acceptable closed-loop poles. The resulting step response is shown in Figure 5.5 (b), showing a 10 – 90% rise time of three seconds. The closed-loop system augmented by the height state is given below:

$$\begin{bmatrix} \dot{\mathbf{x}} \\ \dot{h} \end{bmatrix} = \begin{bmatrix} \mathbf{A} & -\mathbf{B}[0 \quad K_h]^T \\ \mathbf{C} & \mathbf{0} \end{bmatrix} \begin{bmatrix} \mathbf{x} \\ h \end{bmatrix} + \begin{bmatrix} \mathbf{B}[0 \quad K_h]^T \\ \mathbf{0} \end{bmatrix} h_c \quad (5.20)$$

where \mathbf{A} is the closed-loop airspeed and climb-rate controller state matrix, \mathbf{B} the input matrix and \mathbf{C} the altitude output matrix.

5.1.3 Airspeed Climb-Rate Controller Practical Flight Test

The climb-rate step response was investigated in Section 4.2.4.2. This section continues to analyse the airspeed climb-rate controller and investigates the airspeed step response. For the airspeed step response test, the safety pilot is given control over all of the aircraft's actuators except for the throttle and elevator, which are commanded by the airspeed climb-rate controller during the test. In this flight test the controller's ability to regulate airspeed while maintaining climb-rate is

investigated. After manual take-off the pilot trimmed the aircraft at an altitude of 60 m before arming the airspeed climb-rate controller with an airspeed command of 20 m/s and a zero climb-rate command. The control system was allowed to stabilise the aircraft before the airspeed step of 3 m/s was issued. Note this test was also performed on the same day as the climb-rate step response. Both the airspeed and climb-rate step responses were performed in the initial stages of controller design.

During the airspeed step response in Figure 5.6 (a), the accelerometer read a false acceleration spike of approximately -40 m/s^2 at 289.6 s for one sample period. The result of the false acceleration spike propagated into a momentary climb-rate spike, as highlighted in Figure 5.6 (b) which caused the control system to decrease the climb rate of the aircraft momentarily. This issue was fixed by updating the method according to which the accelerometer measurements are read from the IMU by the microcontroller on the IMU PCB. Also, during the airspeed test, the safety pilot banked the aircraft. The LQR controller compensated for the lift lost which also had an effect on the climb rate during the airspeed step response. With the mentioned climb-rate disturbances, a satisfactory practical airspeed step response was obtained. The expected theoretical 10 – 90% rise time and peak time of the airspeed response at 20 m/s are 3.65 s and 6.33 s respectively. The practical 10 – 90% rise time and peak time from Figure 5.6 are 3.34 s and 6 s respectively.

Figure 5.6 also illustrates an initialisation airspeed step response (starting at 281.2 s). The airspeed climb-rate controller was armed at 281.2 s with an initial command of 20 m/s. The second airspeed response is well damped and has 10 – 90% rise time of 3.8 s and a peak time of 6.2 s which correlates very well with the theoretical result. Note that during the second airspeed step response the climb-rate settled near 0 m/s.

In conclusion, a practical airspeed step response where the airspeed climb rate controller was already initialised and without roll-rate disturbances or an accelerometer measurement reading problem during the step response was never obtained. The two practical step responses presented in this section correlate well with the theoretical results and also show the robustness of the controller.

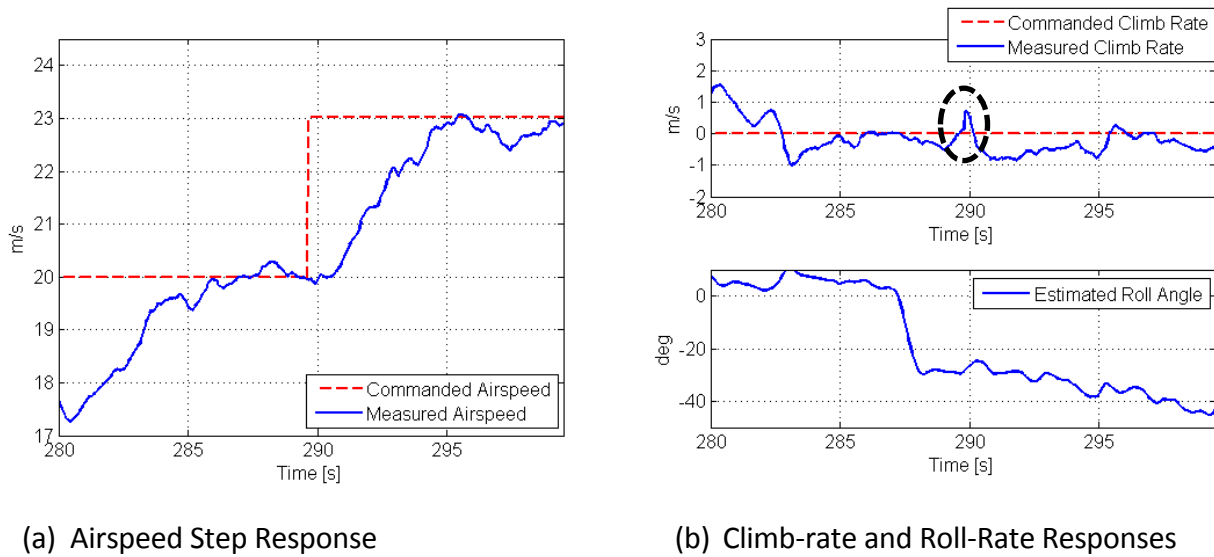
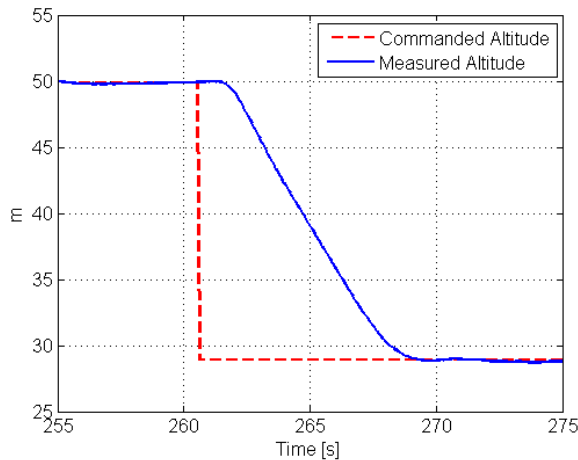


Figure 5.6 Practical Airspeed Step Responses

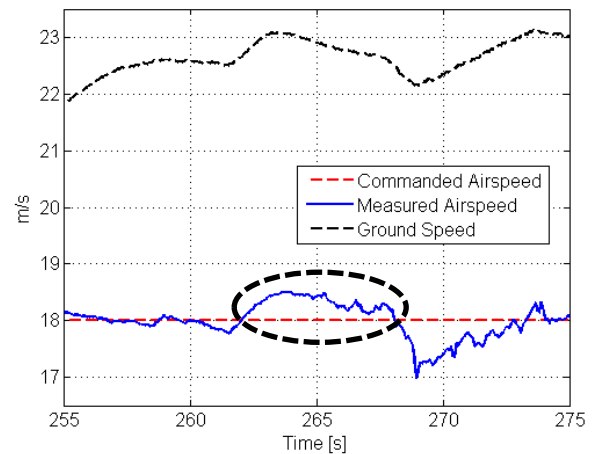
5.1.4 Airspeed Altitude Controller Practical Flight Test

This flight test was not conducted in conjunction with the safety pilot. The data presented here is a segment from data captured from one of the autonomous virtual deck landing tests (mock landings in the air). The results from this flight test represent the FCS performance developed in this dissertation with the designed closed-loop poles locations from Chapters 4 and 5. In this data segment the aircraft is turning from the downwind leg onto the leg that is perpendicular to the runway (base leg). Note that, for this and subsequent flight test results, the aircraft was in flap configuration and the DGPS rover module was installed.

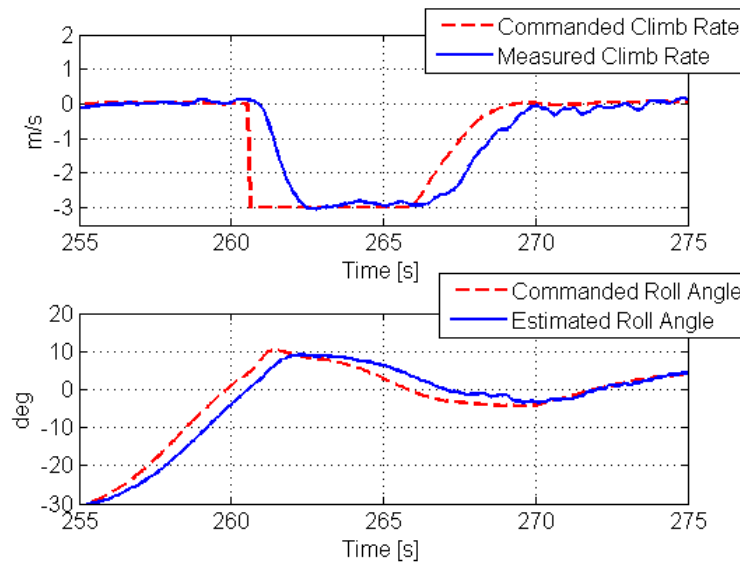
Figure 5.7 illustrates a near-linear practical 21 m step command in altitude with minimal overshoot. The practical 10 – 90% rise time of the step command is 5.1 s and the 90% rise time is 6.8 s. The expected theoretical 10 – 90% rise time is 3.2 s and the 90% rise time is 4 s. Note that the theoretical step response values are for a small altitude step response where the climb-rate limit is not reached. For the large altitude step command, the climb-rate limit of 3 m/s was reached in Figure 5.7. The proportional altitude controller had an RMS regulation error of 0.08 for the time segment between 255 s and 260 s and a 0.1 RMS regulation error between 270 s and 275 s. The highlighted increase in airspeed is a result of the aircraft picking up airspeed as it descends and the decrease in airspeed is a result of the aircraft reducing its climb rate.



(a) Altitude Step Response



(b) Airspeed Regulation during Altitude Step



(c) Climb-Rate and Roll Angle Estimates during an Altitude Step

Figure 5.7 Altitude and Airspeed Controller Practical Flight Test Result

5.2 Lateral Control Architecture

The development and the implementation of the roll-rate controller were described in Chapter 4. This controller forms the lowest level of control in regulating the aircraft trajectory in the inertial frame. The normal specific acceleration vector direction controller (NSAVDC) is designed in Section 5.2.1 by a pole-placement strategy. With the NSAVDC designed and implemented, an interface to

the guidance controller is established. The guidance controller is covered in Section 5.2.2 and calculates a lateral inertial acceleration based on a time-independent pre-programmed flight trajectory. With reference to Figure 2.2 on page 9, the specific commanded vertical and horizontal accelerations are converted into the NSA and reference bank angle as depicted in Figure 5.8.

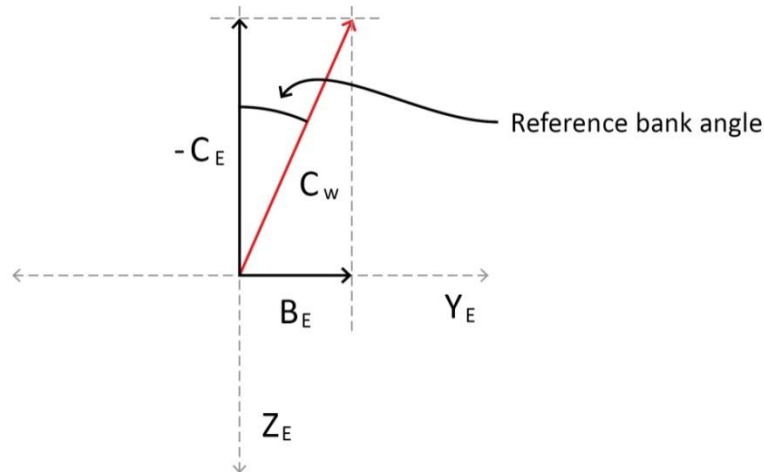


Figure 5.8 Specific Acceleration Command Conversion from Inertial to Wind Axes

The commands for the NSA and roll-angle controllers are given by

$$C_W = \sqrt{C_E^2 + B_E^2} \quad (5.21)$$

$$\text{Reference bank angle} = \arctan\left(\frac{-C_E}{B_E}\right) \quad (5.22)$$

As mentioned earlier, the main goal of the ESL ATOL group is to land an aircraft autonomously in crosswind conditions. To this end the non-linear guidance law developed in [21] is employed for lateral track regulation, since the performance of a PID linear cross-track error controller degrades under windy conditions [21]. The main advantage that the non-linear guidance law controller has over the linear cross-track error controller is that the inertial velocity is used at each instant to calculate the lateral acceleration command.

5.2.1 Normal Specific Acceleration Vector Direction Controller

In Chapter 4 the slowest dynamics of the roll-rate controller were located at 4.5 rad/s . A time-scale separation strategy can be employed to time-scale decouple the NSAVDC from the roll-rate controller. The guidance controller is then time-scale decoupled from the NSAVDC controller. This scenario makes the guidance dynamics too slow, and therefore the roll-rate controller dynamics are taken into account in the design of the NSAVDC. The guidance dynamics are then time-scale decoupled from the NSAVDC.

The NSAVDC regulates the error angle (angle between the commanded and the actual NSA vectors) to zero. The following intuitive equation derived in [1] describes the dynamics of the error angle:

$$\dot{\phi} = P_{W_C} - P_W \quad (5.23)$$

where P_{W_C} is a feed-forward roll-rate term to follow a reference trajectory and P_W is the current wind-axis roll-rate. The following roll-rate control law is defined based on the reference roll-rate and proportional feedback from the error angle:

$$P_R = P_{W_C} + K_\phi \phi \quad (5.24)$$

where K_ϕ is the error angle feedback gain and ϕ the error angle. The roll-rate dynamics from Section 4.4.1 are augmented by the roll-rate integrator of Equation (4.38) and the error angle dynamics of Equation (5.23), resulting in the augmented system below:

$$\begin{bmatrix} \dot{P}_W \\ \dot{E}_P \\ \dot{\phi} \end{bmatrix} = \begin{bmatrix} \frac{L_p}{I_x} & 0 & 0 \\ 1 & 0 & 0 \\ -1 & 0 & 0 \end{bmatrix} \begin{bmatrix} P_W \\ E_P \\ \phi \end{bmatrix} + \begin{bmatrix} \frac{L_{\delta_A}}{I_x} \\ 0 \\ 0 \end{bmatrix} [\delta_A] + \begin{bmatrix} 0 \\ -1 \\ 0 \end{bmatrix} P_R \begin{bmatrix} 0 \\ 0 \\ 1 \end{bmatrix} P_{W_C} \quad (5.25)$$

The closed-loop system is obtained by substituting the following control law into the augmented system above:

$$\delta_A = -K_P P_W - K_E E_P + N_P P_{W_R} \quad (5.26)$$

Note that the control law above is the same as in Equation (4.39) and is simply restated for convenience. Next the feedback gains are calculated by matching the closed-loop characteristic equation coefficients and the desired characteristic equation coefficients. The closed-loop characteristic equation is given in [1] as

$$\alpha_C(s) = s^3 + \left(\frac{L_{\delta_A}}{I_x} K_P - \frac{L_p}{I_x} \right) s^2 + \left(\frac{L_{\delta_A}}{I_x} K_E - K_\phi N_P \frac{L_{\delta_A}}{I_x} \right) s + K_\phi K_E \frac{L_{\delta_A}}{I_x} \quad (5.27)$$

The desired characteristic equation for the augmented system is defined as

$$\alpha_c(s) = s^3 + \alpha_2 s^2 + \alpha_1 s + \alpha_0 \quad (5.28)$$

The feedback gains are calculated by

$$K_P = \frac{L_x}{L_{\delta_A}} \left(\alpha_2 + \frac{L_p}{I_x} \right) \quad (5.29)$$

$$K_E = \frac{L_x}{L_{\delta_A}} \left(\alpha_1 + \frac{\alpha_0}{z_f} \right) \quad (5.30)$$

$$K_\phi = \frac{\alpha_0}{\alpha_0 + \frac{\alpha_0}{z_f}} \quad (5.31)$$

The feed-forward zero z_f can be placed by calculating N_P :

$$N_P = -\frac{K_E}{z_f} \quad (5.32)$$

5.2.2 Guidance Controller

The control law aligns the velocity vector of the aircraft with the reference trajectory and regulates the cross-track position error to zero. When the velocity vector is not in line a perpendicular specific acceleration is generated by the controller to regulate the aircraft back on track. The guidance control law is illustrated conceptually in Figure 5.9.

The reference point on the trajectory is chosen at each instant, with L a constant distance between the dynamic reference point on the trajectory and the aircraft. The following control law regulates the lateral acceleration command:

$$a_s = 2 \frac{V^2}{L} \sin \eta \quad (5.33)$$

In the equation above the direction of the commanded acceleration depends on the sign of η . The commanded acceleration is equal to the centripetal acceleration that the aircraft would experience if it follows the instantaneous circular segment to the reference point. The length of L is given by

$$L = 2R \sin \eta \quad (5.34)$$

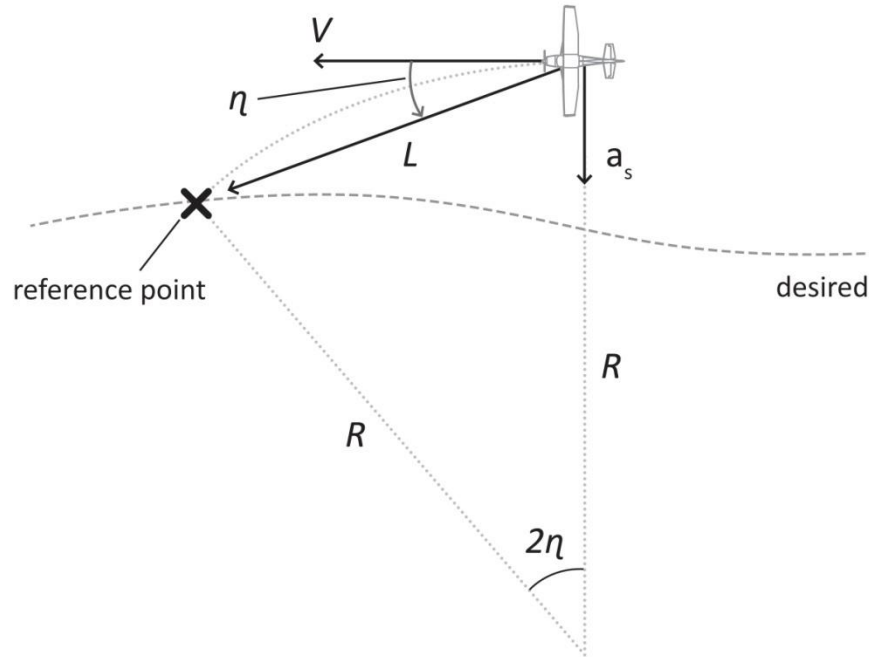


Figure 5.9 Park's Lateral Guidance Controller [21]

The centripetal acceleration command is obtained by solving for R in Equation (5.34) and substituting the result into the centripetal acceleration, Equation (5.35):

$$a_s = \frac{V^2}{R} = 2 \frac{V^2}{L} \sin \eta \quad (5.35)$$

The non-linear guidance law is linearised in the scenario depicted in Figure 5.10 in order to obtain the guidance controller's dynamics in the s plane.

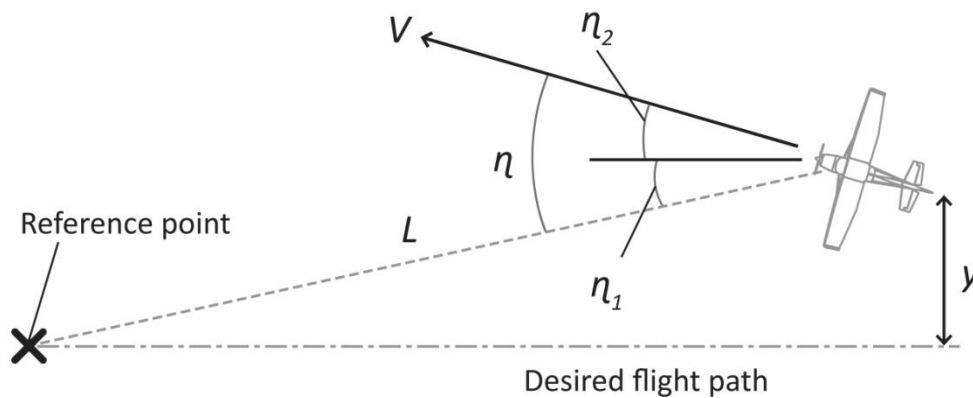


Figure 5.10 Linearising the Non-Linear Guidance Law [21]

In the scenario shown in Figure 5.10, L is the distance between the aircraft and reference point, V the trim airspeed, and η is assumed to be a small angle

$$\eta \approx \eta_1 + \eta_2 \quad (5.36)$$

with

$$\eta_1 \approx \frac{y}{L} \quad , \quad \eta_2 \approx \frac{\dot{y}}{V} \quad (5.37)$$

Substituting Equation (5.34) and the results from Equation (5.37) into Equation (5.35) yields

$$a_s = 2 \frac{V^2}{L} \sin \eta \approx 2 \frac{V}{L} \left(\dot{y} + \frac{V}{L} y \right) \quad (5.38)$$

The linearised guidance control law yields a PD controller that regulates the cross-track error. By taking the Laplace transformation of Equation (5.38) the closed-loop pole locations of the guidance controller can be written as

$$s = -\frac{V}{L} \pm \frac{V}{L} i \quad (5.39)$$

The resulting closed-loop poles above are optimally damped and located at $\sqrt{2}V/L \text{ rad/s}$ in the s plane. The frequency of the guidance controller at the aircraft trim airspeed V can be adjusted by changing the magnitude of the sight vector L .

5.2.3 Pole-Placement and Simulation

The roll-rate and integrator pole locations remain the same as those in the design of the roll-rate controller in Section 4.4.2. The closed-loop error angle pole is placed at

$$p_\phi = 2.25 \text{ rad/s} \quad (5.40)$$

In this project the magnitude of the sight vector was chosen to be

$$L = 100 \text{ m} \quad (5.41)$$

The resulting closed-loop guidance controller poles are located at

$$\omega_{trim} = \frac{\sqrt{2}V_{trim}}{L} = 0.212 \text{ rad/s} \quad (5.42)$$

Note that the closed-loop poles of the guidance controller are approximately 10.5 times slower than the error-angle pole. The initial idea in flight testing was to have the aircraft regulate its position slowly on the desired trajectory when on its final approach. The sight vector magnitude in

Equation (5.41) provided adequate cross-track regulation performance for the landing circuit and was never adjusted due to limited flight test time. For future improvements, however, a gain-scheduled strategy for different landing phases is suggested. Such a strategy would make the guidance controller more aggressive during the landing approach for tight lateral cross-track error control and less aggressive near the touchdown point.

The NASVDC non-linear step response is illustrated in Figure 5.11, followed by a non-linear lateral step response of the guidance controller in Figure 5.12. This section is concluded with an overview of the lateral control system closed-loop pole locations in Figure 5.13.

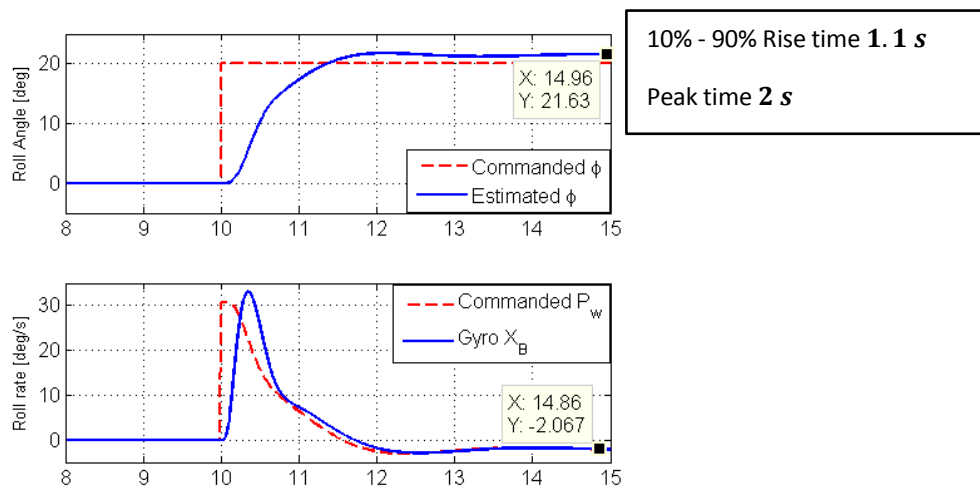


Figure 5.11 NSAVDC Non-Linear Step Response

The non-linear roll-angle step response of the NSAVDC is fast and well damped. The system is not expected to have a steady-state error since it has an augmented error integrator on roll-rate that provides infinite steady-state gain. The resulting steady-state error behaviour is a result of the banked turn state of the aircraft. In this state the constant yaw rate couples into the measured roll-rate via the pitch angle. This steady-state error effect becomes smaller as the bank angle decreases.

The guidance controller's ability to track a trajectory by rolling the aircraft is analysed in a non-linear simulation by inducing a lateral position error. In the simulation results (shown in Figure 5.12) a lateral position error of ten metres resulted in a roll-rate that caused the aircraft to bank 5° to turn the aircraft. The position step response below has a 10 – 90% rise time of 6.5 s and a settling time of 18.5 s. The approximated 10 – 90% rise time of the second order system is 6.8 s and the approximated settling time is 20.8 s. The simulated guidance controller is a bit faster than the

approximated rise time and settling time; this result is caused by overshoot in roll-rate with a result of banking the aircraft faster.

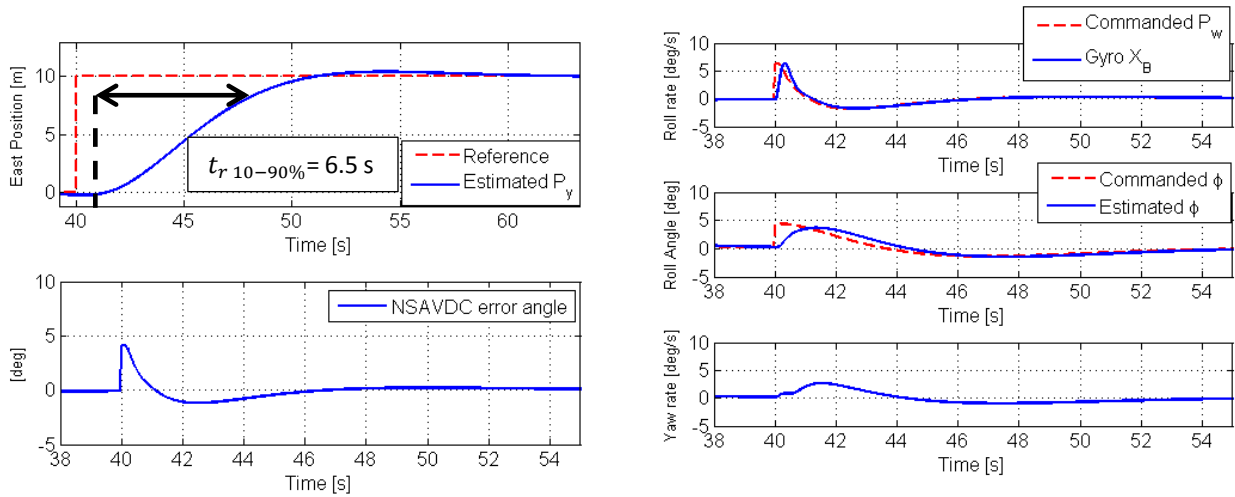


Figure 5.12 Lateral Position Step Response of the Guidance Controller

In conclusion: A gain schedule strategy can be employed to increase the bandwidth of the guidance controller in different stages of landing. By increasing the guidance controller’s bandwidth, a shorter approach can be flown since the settling time of the guidance controller decreases. The closed-loop pole locations of the lateral control architecture are illustrated in Figure 5.13.

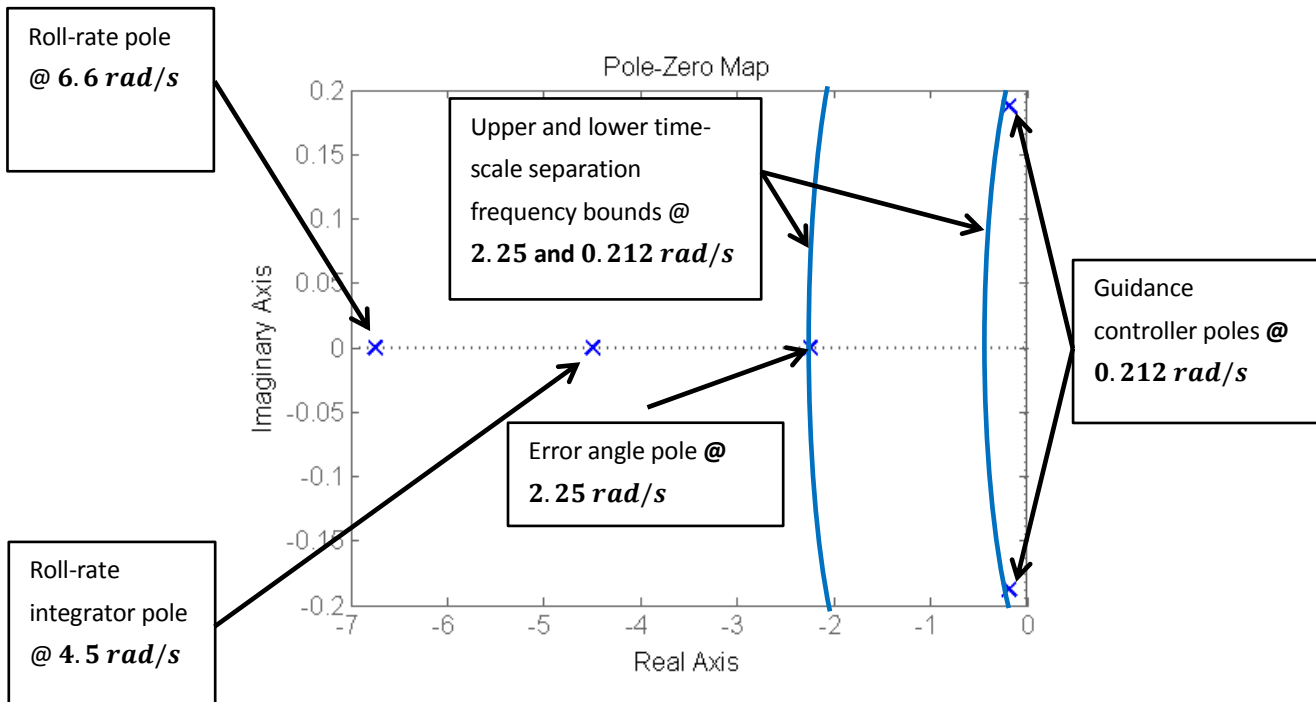


Figure 5.13 Lateral Control System Closed-Loop Pole Locations at Trim Airspeed

5.2.4 Guidance Controller and NSAVDC Practical Flight Test

In this section the performance of the guidance controller and the NSAVDC is investigated. The data segments below are extracted from data captured during an autonomous virtual deck landing. Figure 5.14 (a) shows the reference and achieved flight trajectory. Figure 5.14 (b) shows the reference and achieved trajectory in its North and East components. Note that the large following error in the North/East component in Figure 5.14 (b) shows the length of the sight vector used in the guidance controller. Figure 5.14 (c) shows the commanded and estimated roll-angle during the flight trajectory illustrated in Figure 5.14 (a). Finally Figure 5.14 (d) is a zoomed-in version of Figure 5.14 (b) and displays the lateral cross-track error on the up-wind leg and the runway outlines. In Figure 5.14 (b) and (d) the aircraft is in line with the runway on the up-wind leg for the time segment of 292 s to 315 s. The aircraft is flying over the runway between 308 s and 315 s.

In Figure 5.14 (a) the runway is located between the two dotted lines. The runway at HRF is 5 m wide and 100 m long with a -14.1° heading angle. Near the end of the down-wind leg the autopilot changed the aircraft's altitude from 50 m to 29 m as illustrated in Figure 5.7 (the data segments for the previous section and this section are extracted from the same flight test). On the up-wind leg the autopilot captured the two successive glide slopes and descended from 29 m to the virtual touchdown point at 8 m in altitude at zero North and East in Figure 5.14 (a). On the down-wind leg the aircraft's ground speed ranged between 20 m/s to 23 m/s and the commanded airspeed was 18 m/s as illustrated in Figure 5.7. On the up-wind leg the ground speed was approximately 1 m/s higher than the commanded airspeed which ranged between 14 and 15 m/s.

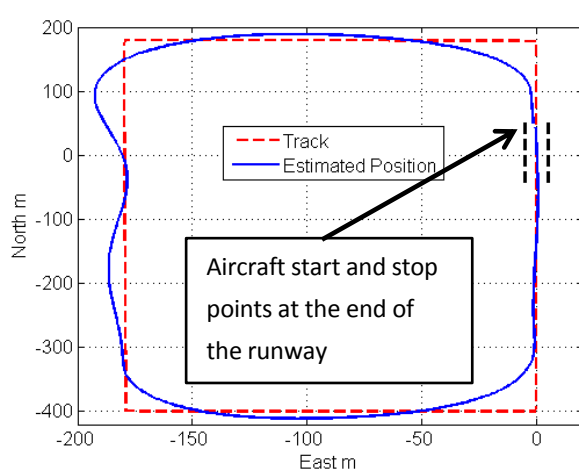
On the up-wind leg the guidance controller regulated the lateral cross-track error within bounds of ± 1.3 m with an RMS error of 0.71. Over the runway a satisfactory lateral cross-track error was obtained: the aircraft was within bounds of ± 0.85 m with an RMS error of 0.40.

5.3 Summary

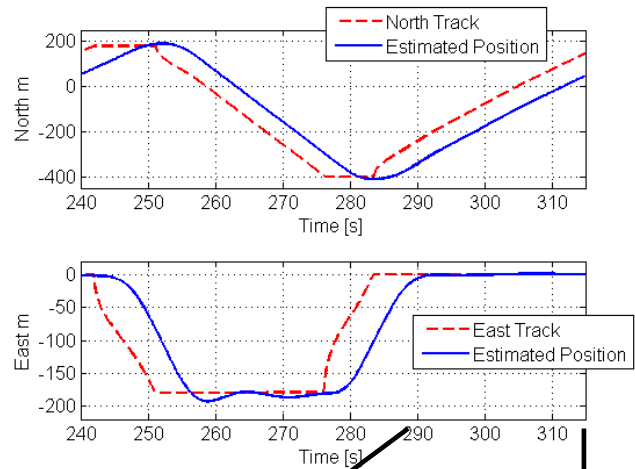
An aircraft-independent longitudinal outer-loop controller was designed to regulate the airspeed and altitude of the aircraft via a time-scale separation strategy. The designed outer-loop of the lateral control system takes the inner-loop dynamics into account since the available bandwidth near the touchdown airspeed is not sufficient for two consecutive time-scale separations.

The FCS (longitudinal and lateral control system) was tested practically by arming the autopilot to run through the landing state machine described in Chapter 7 at a safe altitude. The flight test

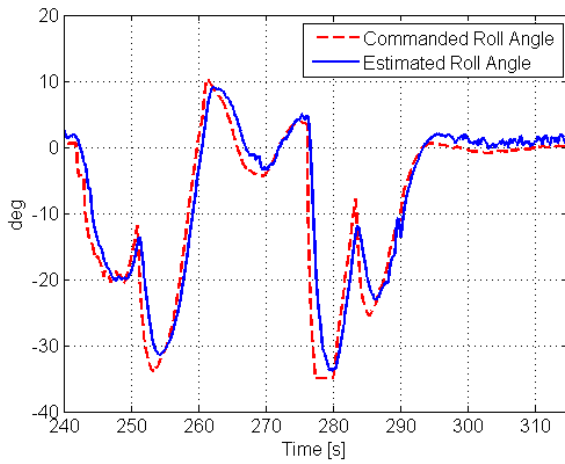
concluded with satisfactory practical results. This chapter marks the end of controller design. In Chapter 6 the hardware and software of the autonomous landing system are described.



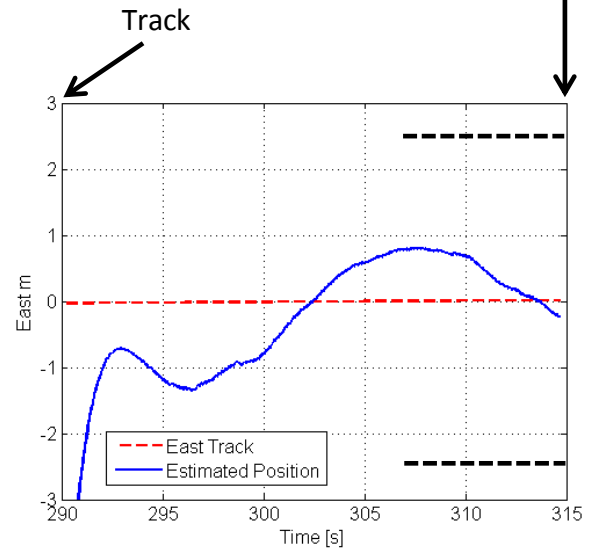
(a) Desired and Actual Flight Track



(b) North and East Components of Flight



(c) Commanded and Estimated Roll-Rate during the Flight Track



(d) Lateral Cross-Track Error on the Up-Wind Leg

Figure 5.14 Guidance Controller and NSAVDC Practical Flight Test Results

Chapter 6

Hardware and Software

This chapter presents the hardware and software used in this project. The chapter is divided into three main sections: Section 6.1 describes the airframe selected for this project, Section 6.2 gives an overview of the avionics and Section 6.3 concludes the chapter with an overview of the ground-station software.

6.1 Airframe

A testing platform was required for the goals set out in this project. At the start of the project, during a research group meeting (a think-tank session consisting of students and lecturers), a decision was made to standardise the airframe for all fixed-wing projects in the ESL. A modified Phoenix trainer 60 airframe was selected. Figure 6.1 shows the modified airframe by Banitz Hobbies. The modifications include: added wing strut for wing support, flap control surface, nose wheel and a section to install the avionics box. This airframe was chosen since it can be transported to the local airfield with relative ease (i.e. fuselage fits into the boot of a car) due to its size and it has sufficient space for avionics as well as a low wing loading (without any avionics). Using a standardised airframe has the following advantages for future projects in the ESL:

- New airframes can be equipped more quickly with avionics since all the planning has already been done. In other words the existing airframe can be used as a reference to equip a new airframe.
- Aerodynamic modelling coefficients can be shared amongst projects.
- Lower-level flight control systems designed specifically for this airframe can be reused in other projects without the need to retest.



Figure 6.1 The Airframe on Arrival from Banitz Hobbies



Figure 6.2 The Equipped Airframe on a Flight Test Day

6.2 Avionics

A block diagram overview of the complete avionics system is shown in Figure 6.3.

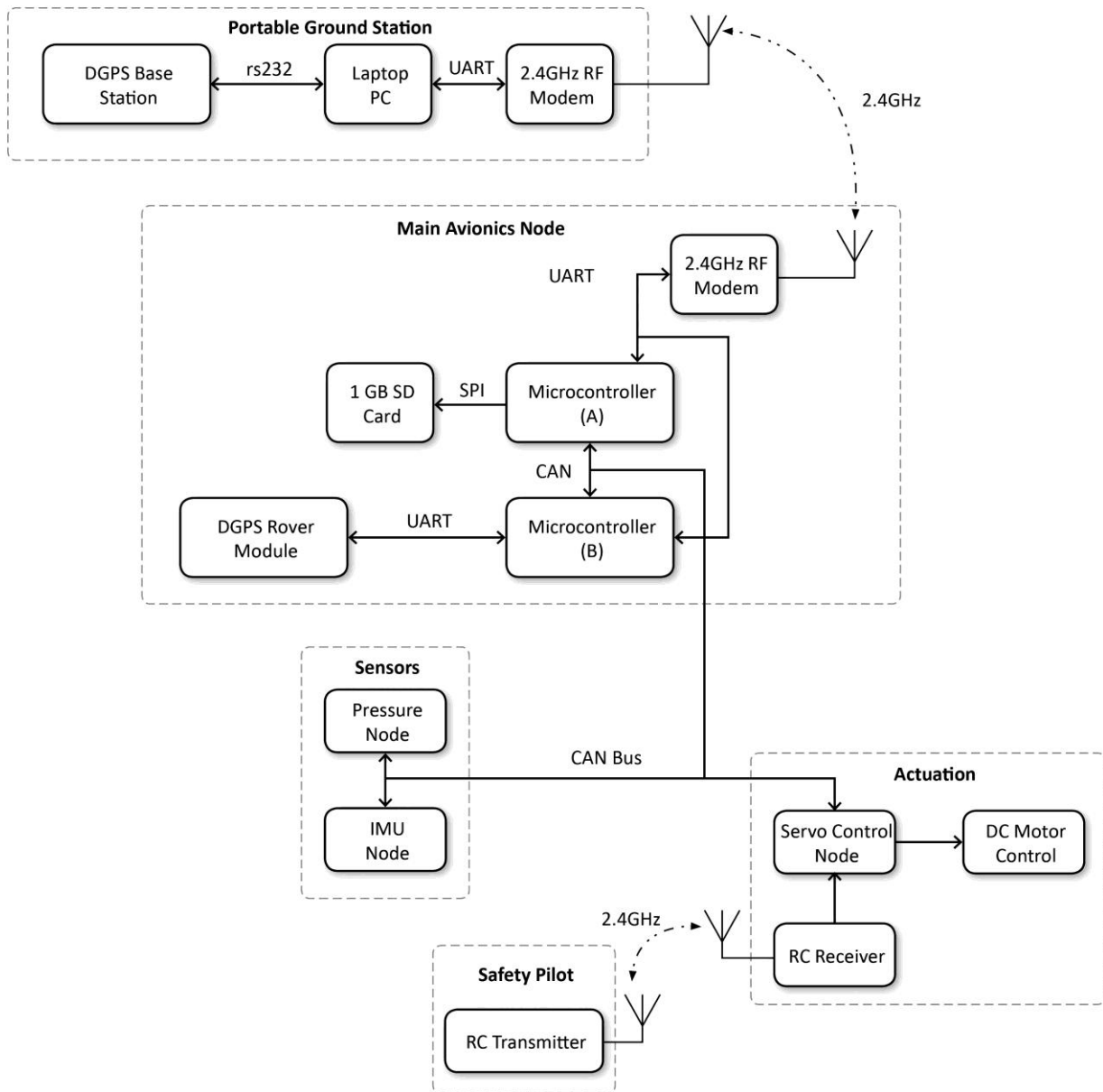


Figure 6.3 Avionics and Ground Station Block Diagram Overview

As can be seen in the block diagram above, the system can be divided into two parts: the aircraft and the ground station. The aircraft houses the following components: radio control (RC) receiver,

servos, avionics built in the wing and the avionics box built into the fuselage. The ground station consists of the DGPS base station, a laptop running the ground-station software, a radio frequency modem and an RC transmitter. The ground-station software is an interface to the aircraft's OBC and links the DGPS base station with the DGPS rover module in the avionics box on board the aircraft.

The following subsection gives an overview of the avionics used in this project. For more detailed information on the avionics refer to [19] and [29].

6.2.1 Avionics Box

The avionics box developed in this project was designed to house the standard ESL avionics stack and a DGPS rover module. The avionics box was designed in such a way that it can be easily inserted and removed from the aircraft. Figure 6.4 (a) shows a connection interface and top-side view of the avionics box, while Figure 6.4 (b) shows the avionics stack and rover module (encased in an aluminium box).



(a) Avionics Box



(b) Avionics Stack and Rover Module

Figure 6.4 Avionics Box Side View and Avionics

The avionics stack inside the avionics box consists of: an on-board computer (OBC), an inertial measurement unit (IMU), a DGPS rover module, an RF modem and an SD card for data logging. Figure 6.5 shows the avionics box mounted inside the aircraft. The avionics box is suspended inside the aircraft by two silicon mounts on each side connected to aluminium brackets which are held in place by two rigid rubber support pins. This configuration provides vibration isolation.



Figure 6.5 Avionics Box Mounted inside the Aircraft

6.2.2 On-Board Computer

The FCS is coded onto two 16-bit microcontrollers (dsPIC20F6014) linked via a CAN bus. With reference to Figure 6.3, microcontroller A is responsible for the operations listed below, and the software routine that microcontroller A executes is illustrated in Figure 6.6. The operations are:

- transmitting and receiving the telemetry data;
- sampling the IMU, magnetometer, air pressure and DGPS sensors;
- executing of the control (i.e. calculating and issuing actuator commands), state estimation and navigation algorithms; and
- logging sensor and flight data.

Microcontroller B is dedicated to parsing the RT-2 L1TE RTK correction packets received from the DGPS ground station via the RF module. These correction packets are sent to the rover module via the UART. The rover module updates microcontroller B on the aircraft's position, velocity and heading via the UART. Before the position, velocity and heading measurement updates are transmitted to microcontroller A via the CAN bus, a cyclic redundancy check (CRC) is performed in microcontroller B to ensure that the data is valid. The rover module is capable of

providing high-precision measurement updates at 50 Hz. However, due to limited processing power on microcontroller B and high data input/output rates, the DGPS setup was configured to provide measurement updates at a rate of 7 Hz (fastest reliable rate).

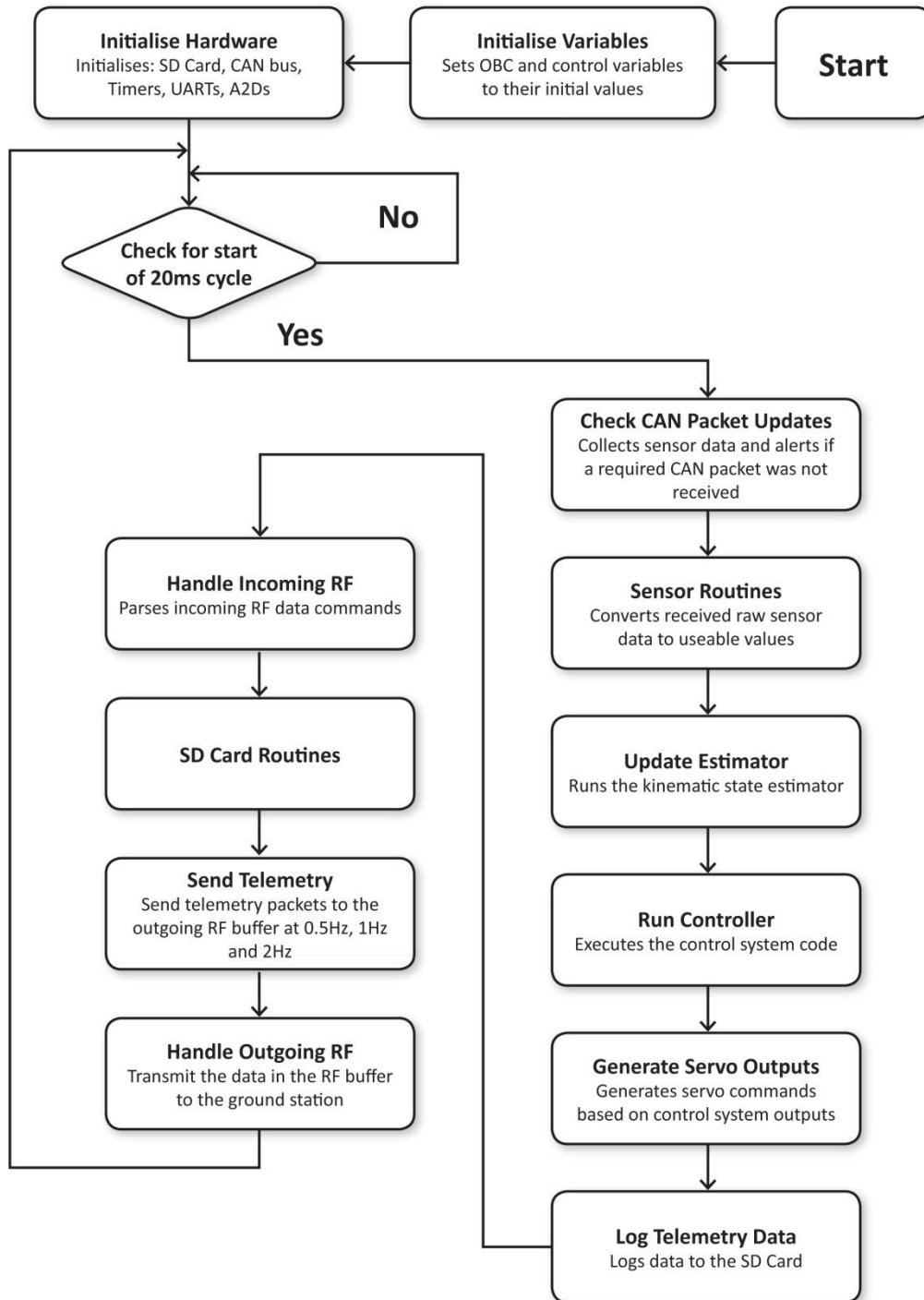


Figure 6.6 OBC Software Routine [ESL]

6.2.3 Inertial Measurement Unit

The IMU board houses the following two main components:

- ADIS 16350 tri-axis inertial sensor
- dsPIC30f4013 microcontroller

The IMU uses an SPI interface to communicate with the microcontroller which, in turn, uses the CAN bus to communicate with microcontroller A. The IMU is capable of conditioning the measured angular rates and sensed accelerations via a digital signal processing block. The IMU operates from a single five-volt power supply rail and was calibrated against temperature variations. The rate gyros were calibrated by spinning the IMU on a high-precision rotation table at different angular rates and the accelerometers were calibrated by placing the IMU on a flat surface at different, known angles.

Rate Gyroscopes

With no signal conditioning (digital processing) the rate gyroscopes are capable of measuring angular rates of up to $\pm 300^\circ/s$ at a bandwidth of 350 Hz using a 14-bit digital word with a resolution of $0.07326^\circ/s$. The IMU is programmed to filter the angular rates at 11 Hz via a five-tap Bartlett window.

Accelerometers

The accelerometers have a $\pm 10g$ range and with a 14-bit word a resolution of 2.522 mg is obtained. The measured accelerations are also filtered at 11 Hz via a five-tap Bartlett window.

6.2.4 GPS Module

Initial testing of the flight control system was done with a low-cost GPS module. Once enough confidence was gained in the FCS, the more expensive DGPS rover module was installed, replacing the low-cost module. The low-cost GPS module is the u-Blox RCB-4H OEM Receiver with a 25 dB gain active antenna with 4 Hz update rate. This low-cost GPS module has been used extensively in previous flight tests for various projects in the ESL. The DGPS software was developed by the ESL engineers (AM de Jager and Lionel Basson). During this project, the DGPS software was integrated into the OBC code and the hardware was integrated into the avionics box and airframe. The new DGPS system was thoroughly tested on the ground and in the air before it was used in the autopilot.

The OEMV-1G DGPS rover module was used in this project with the GPS-533 antenna installed on the aircraft. NovAtel's ProPack V3 was used as the ground station with a GPS-702L antenna.

6.2.5 Radio Frequency Communication Module

The RF module and antenna used are listed below:

- MaxStream XStream 2.4GHz OEM transceiver
- 2.1 dB gain active dipole antenna

The RF module has been proven to provide reliable line-of-sight communication in a number of previous flight tests in various projects in the ESL. The RF module is configured in a full duplex mode with a baud rate of 9600 *bps*.

6.2.6 Pressure/Magnetometer Printed Circuit Board

The pressure/magnetometer PCB is used to sense the dynamic and static pressure as well as the earth's magnetic field for navigation. The pressure/magnetometer PCB is installed in the wing and communicates via the CAN bus with microcontroller A. The pressure/magnetometer PCB consists of the following components:

- MPXV5004G differential pressure sensor
- MPXA4115A absolute pressure sensor
- HMC2003 three-axis magnetometer from Honeywell
- Microcontroller PIC18f458

The pressure sensor provides the altitude, airspeed and climb-rate of the aircraft. Only the airspeed was used since the DGPS provides far more accurate altitude and climb-rate measurements. Figure 6.7 is a photograph of the pressure/magnetometer PCB installed in the right wing with the pitot tube. The pressure/magnetometer PCB was installed near the wing tip to avoid possible propeller wash and to place the magnetometer as far as possible from magnetic materials and high currents from the motors batteries.

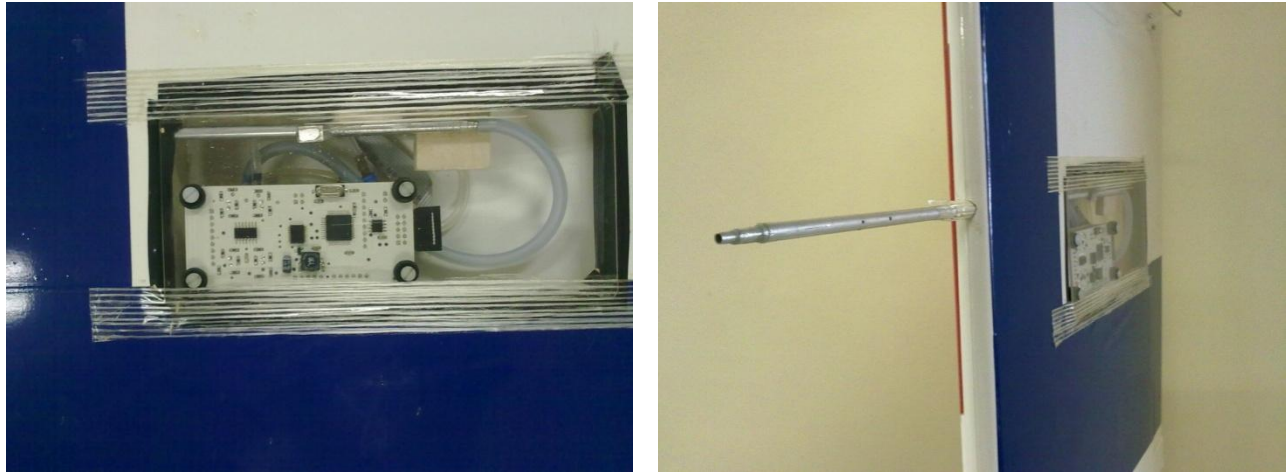


Figure 6.7 Photograph of the Pressure/Magnetometer PCB Installed in the Wing

Pressure

The pressure sensor is capable of measuring an airspeed of up to 80 m/s with a digital resolution of 0.002 m/s . The signal-conditioning circuits for the pressure sensors can be found in [29].

Magnetometer

The HMC2003 yaw angle measurements are used for navigation. The sensor is capable of measuring magnetic fields up to $\pm 2\text{ Gauss}$. The earth's magnetic field magnitude in the vicinity of Stellenbosch is in the order of 0.26 Gauss . The magnetometer was configured in a previous project to measure magnetic fields of up to $\pm 0.625\text{ Gauss}$, with a $20\mu\text{ Gauss}$ resolution.

Since the magnetometer is mounted in the wing, any materials with magnetic properties will distort the earth magnetic field and corrupt the magnetometer measurements. The calibration technique used by [29] is reused to calibrate the magnetometer for the disturbance caused by components with magnetic properties near the magnetometer. The calibration technique also determines the inherent sensor offsets.

6.2.7 Power Distribution

The following battery packs are used to power the avionics and the brushless DC motor:

- 11.1V , 1800mAh , 20C , LiPo battery pack
- 4.8V , 1500mAh Nichol Cadmium battery pack
- 18.5V , 5000mAh 20C , LiPo battery pack

The 11.1 V LiPo battery pack is used to power the avionics and the servo board (via the CAN bus). In the laboratory environment, the avionics pack consumes approximately 9.6 *watts* of power with the rover module and servo board switch on. The 11. V LiPo avionics battery pack can power the avionics with the rover module and servos switch off for approximately an hour. The NiCd Cadmium battery pack is connected to the servo board and acts as a backup power supply in case the servo board gets disconnected from the CAN bus. The 18.5 V LiPo battery pack is used to power the brushless DC motor. At full safe discharge rate the LiPo will be completely discharged in three minutes. Depending on airspeed in the flight test and wind conditions it was found experimentally that a flight test lasting 4.5 minutes results in the 18.5 V LiPo battery pack being at half of its capacity (TCS CAP averaging at 53%). It was also found experimentally via flight testing that the 11.1 V LiPo avionics battery pack can be used in two successive flight tests before recharging is required.

6.3 Ground Station

The ground station consists of the NovAtel base station, the RF communications module and a laptop running the ground-station software as shown in Figure 6.3. The ground-station software was developed in the ESL to interface with the OBC using QtCreator (a cross-platform C++ integrated development environment). The ground-station software provides an interface to the OBC to upload controller commands and parameters, to configure the OBC for the planned flight test and to monitor the aircraft. The RC transmitter in Figure 6.3 was modified so that the pilot can retake control of the aircraft at any time, by using one of the RC transmitter's channels in conjunction with a switch in the ground station to arm/disarm the autopilot (both switches must be armed to engage the autopilot). Figure 6.8 illustrates the object-orientated ground-station software and the data flow between the main objects with the hardware RF link to the OBC. The remainder of this section gives an overview of the different pages of the ground-station software. The *Controller*, *Controller Setup* and *L and N Setup* tabs were developed for the purpose of this project.

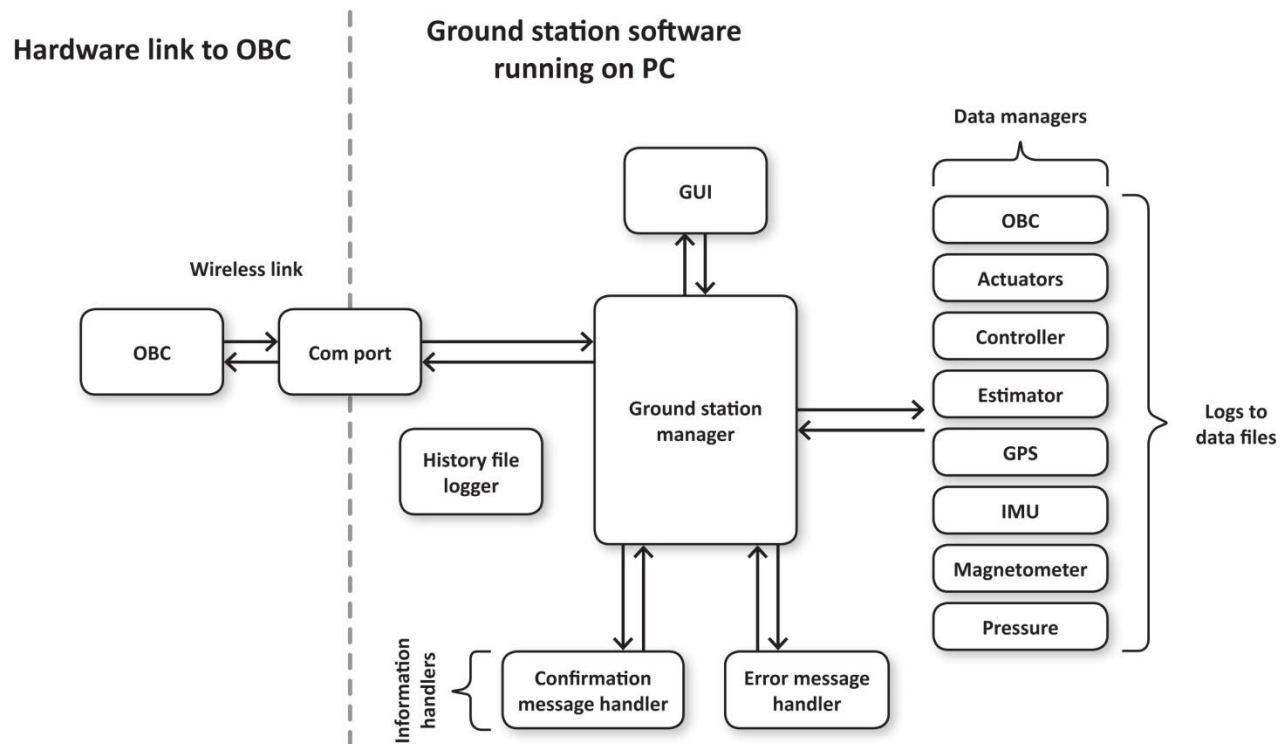


Figure 6.8 Ground Station Objects and Data Flow [ESL]

6.3.1 Ground Station Application

In Figure 6.9, the left-most part of the window is the *Main* tab. On this tab the commands such as *Start OBC* and *Reset OBC*, *Arm Autopilot* (toggle switch), *Start Logging* and *Stop Logging* data can be issued. The tab displays the *OBC Time*, the amount of *Data Logged* on the SD card, *Round Trip Time* of the OBC and the measured voltage on the servos. When the *Toggle HILS* button is pressed the OBC is set up for a HIL simulation. The *Command History* box (bottom left) displays a running history of all the ground-station commands issued and error messages that occur. The *Command History* is also logged. The right part of the window is the *IMU, Mag + Pressure* tab. This tab displays the angular rates, accelerations, magnetometer readings and pressure sensor data. This tab gives a good indication of the current state of the aircraft.

In the current screen shot, the *Controller* tab is selected and displays the *Controller* group boxes. The *Main* tab and *IMU, Mag + Pressure* tab are always visible. The *Controller* and *Control Setup* tabs are discussed next and the remaining tabs are discussed in subsequent sections.

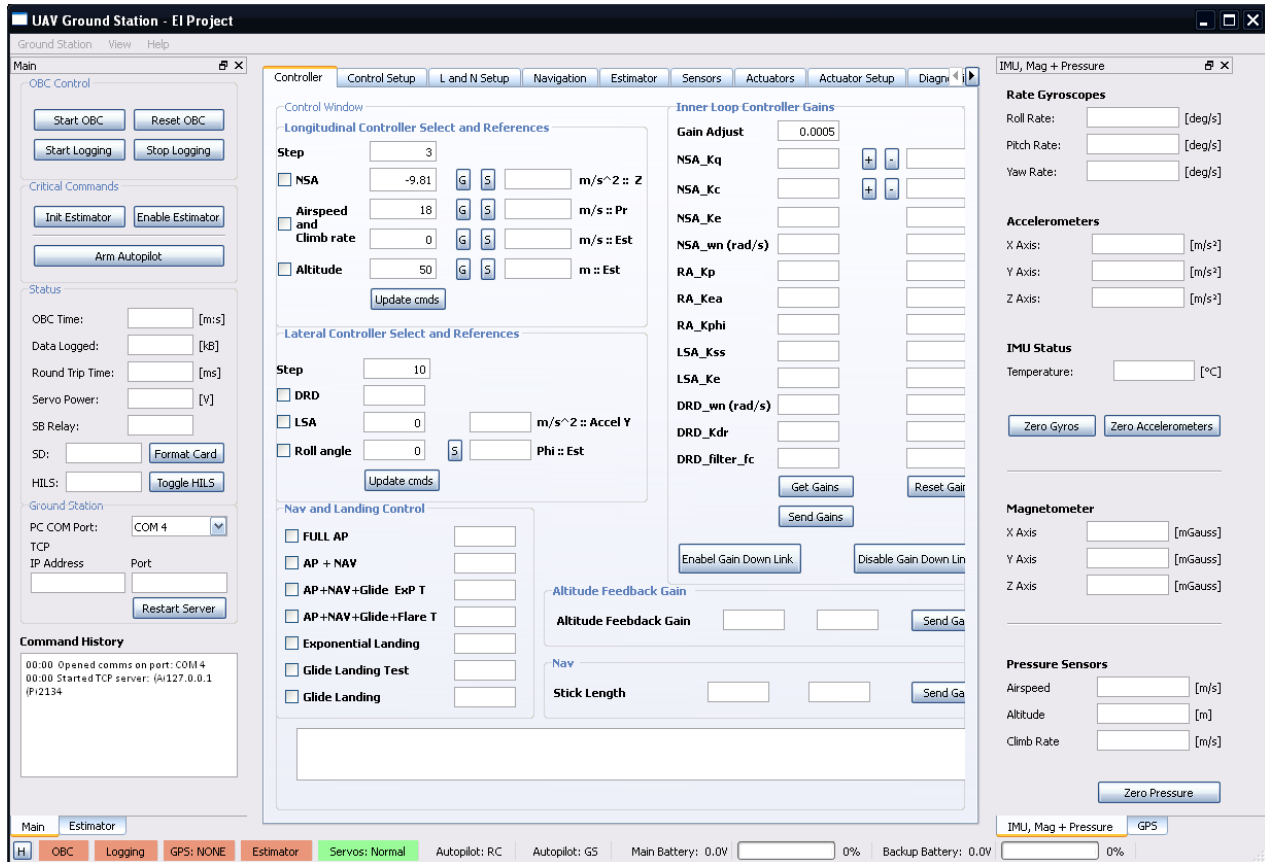


Figure 6.9 Ground Station Application with Controller Tab Open

In Figure 6.10, the *Controller* tab is selected and displays the *Controller* group boxes (zoomed in on the middle part in Figure 6.9 for clarity). The *Longitudinal/Lateral Controller Select and References* group boxes allow various autopilot control loops to be armed and their reference commands to be set. The *Inner-Loop Controller Gains* group box was used in initial flight testing to tune gains for the different inner-loop controllers. The *Altitude Feedback Gain* and *Nav* group boxes were used to adjust the proportional altitude controller feedback gain and the guidance stick length. The *Nav and Landing Control* group box (bottom left) enables and disables different landing phases in the landing state machine. For example, the *FULL AP* option enables the *Airspeed-altitude*, *DRD* and *Roll-angle* controllers. The corresponding white bar across the controller and state machine option turns green if the autopilot acknowledges the command. The white bar on the bottom turns green if the DGPS has a lock, and latches red if the DGPS loses lock at any time on the ground or during flight. In a situation where the DGPS loses lock, the DGPS internal estimator will start to diverge from centimetre accuracy to a normal GPS accuracy. When the DGPS loses lock the safety pilot is required to take over control of the aircraft.

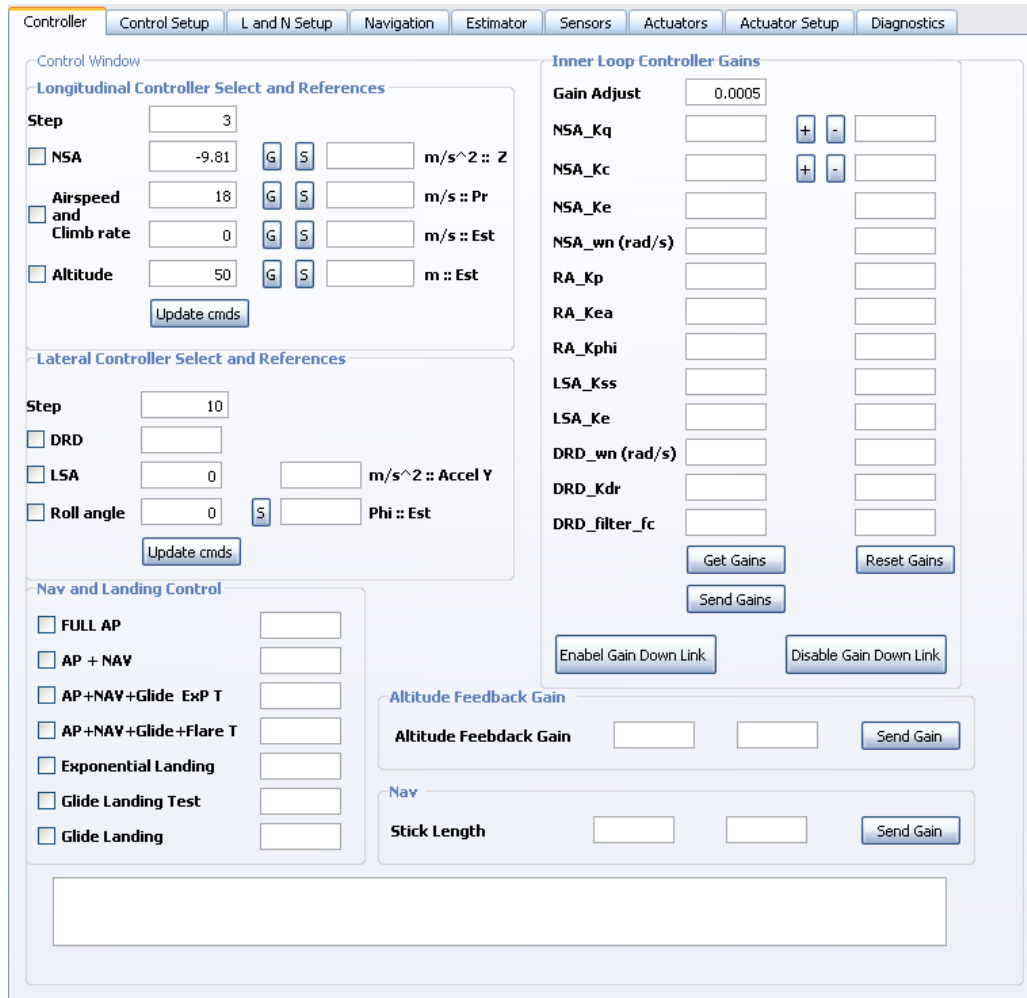


Figure 6.10 Controller Tab

The Control Setup tab was used in initial flight testing to adjust the following parameters on the OBC: inner-loop controller parameters (damping, integrator pole locations, etc.), the airspeed climb-rate controller feedback gains, the maximum climb-rate and airspeed, maximum roll-rate, maximum control surface deflections, etc.

6.3.2 Landing and Navigation Setup (L and N Setup Tab)

The screenshot shows the 'L and N Setup' tab in a software interface. The interface has tabs for Controller, Control Setup, L and N Setup (selected), Navigation, Estimator, Sensors, Actuators, Actuator Setup, and Diagnostics. The L and N Setup tab contains two main sections: 'Landing command' and 'Lateral Navigation Waypoints and Stick Parameters'.

The 'Landing command' section has buttons for 'Exponential Landing' and 'Glide Landing'. Below these are various input fields for parameters:

- True North Psi: -14.1
- Runway axis: (empty)
- Npos_Glide_start: -271.3233
- Npos_Glide_end: -125
- Npos_Flare_start: -125
- Npos_Flare_end: 50
- Flare_Position_Constant: 0
- Distance to impact: 0
- Change in Airspeed second glide slope (dv): 0
- Change in Airspeed before impact: 0
- Change in Airspeed first glide slope: 0
- Roll Angle Bias: 0
- Glide slope Gradient (m_g): 0
- Glide slope Constant (c): 0
- Offset Altitude: 0
- Landing Stick Length: 0

The 'Lateral Navigation Waypoints and Stick Parameters' section has a table for waypoints (WP1, WP2, WP3, WP4) with columns for Runway axis, NED, and NED OBC. It also has buttons for 'Transform Waypoints', 'UpDate WayPoint', 'Counter Clock Wise Default', 'Clock Wise', and 'GS OBC'.

Figure 6.11 L and N Setup Tab

The *Landing Command* group box in Figure 6.11 shows the different landing state machine parameters that can be adjusted. The *Glide Landing* button loads the default landing parameters in the *Landing Command* group box. Once loaded, the landing parameters can also be manually adjusted and updated on the OBC via the *Update Landing Setup* button. The parameters that can be adjusted include: the distance before the aircraft starts its descent on the first glide slope; the distance before the aircraft captures the second glide slope; the two different glide slope gradients; different airspeeds during different stages of the state machine; the virtual deck landing altitude (*Offset Altitude*) etc. In the *Lateral Navigation Waypoints* group box, four different waypoints can be entered. The waypoints are specified in runway axes and transformed via the runway heading angle into NED coordinates when the *Transform Waypoints* button is pressed. The runway heading angle at HRF is -14.1° (coordinated in NED) as shown in the *True North Psi* box in Figure 6.11.

6.3.3 Estimator

The screenshot displays the 'Estimator' tab interface, which is divided into four main sections:

- Reference Vectors:** Contains input fields for Gravity Vector (North: 0.0000 [m/s²], East: 0.0000 [m/s²], Down: -9.8100 [m/s²]), Magnetic Field (Stellenbosch dropdown, X Axis: 93.90 [mGauss], Y Axis: -41.37 [mGauss], Z Axis: -236.30 [mGauss]), and OBC Location. An 'Upload References' button is at the bottom.
- Estimator States:** Displays 'Inertial' data with 'Position' (North, East, Down in [m]) and 'Velocity' (North, East, Down in [m/s]). It also shows 'Attitude' (Roll, Pitch, Yaw in [deg]).
- Estimator Setup:** Includes 'Inertial Estimator Propagation' with radio buttons for 'Full Estimator with Accelerometers' and 'No Accelerometer Propagation'. It also has 'Attitude Estimator Updates' with radio buttons for 'Full TRIAD Update' and 'Tilt/Heading Update'. 'Initialise Estimator' and 'Enable Estimator' buttons are at the bottom.
- Noise Characteristics:** Features a 'Process' dropdown and 'Update: GPS'/'Update: Mag' buttons. It contains input fields for 'Acc.' (X, Y, Z Axis in [m/s²]) and 'Gyros' (Roll, Pitch, Yaw in [rad/s]). An 'Upload Characteristics' button is at the bottom.

Figure 6.12 Estimator Tab

The *Estimator* tab is shown in Figure 6.12. Once the estimation strategy is selected in the *Estimator Setup* box, the estimator is initialised and enabled (on the runway, moments before take-off) via the *Initialise Estimator* and *Enable Estimator* buttons. In this project the *Full Estimator with Accelerometers* and *Full TRIAD Update* options were selected. The estimated position, velocity and attitude states are shown in the *Estimated State* group box. The *Reference Vectors* and *Noise Characteristics* group boxes were not used.

6.3.4 Sensors Tab

The screenshot displays the 'Sensors' tab in a software interface, organized into several functional groups:

- Inertial Measurement Unit:**
 - Rate Gyroscopes:** Roll Rate, Pitch Rate, and Yaw Rate, each with a text input field and a unit of [deg/s].
 - Accelerometers:** X Axis, Y Axis, and Z Axis, each with a text input field and a unit of [m/s²].
 - Status:** Temperature with a text input field and a unit of [°C].
 - Buttons:** 'Zero Gyros' and 'Zero Accelerometers'.
- GPS:**
 - Status:** GPS Client Status (GPS Client Disconnected), Groundstation RTK Status (DGPS Disabled), and Rover RTK Status (RTK Timeout) are shown in orange status boxes. Fix Type, Satellites Used, Satellites Visible, and Diff Age are text input fields.
 - Buttons:** 'Request Space Vehicle Information'.
 - Geodetic LLH Position:** Latitude, Longitude, and MSL, each with a text input field and a unit of [deg] or [m].
 - Sigma:** Three text input fields for Sigma values.
 - Inertial Velocity:** North, East, Down, and Heading, each with a text input field and a unit of [m/s] or [deg].
 - Inertial Position:** Three text input fields for Inertial Position values, each with a unit of [m].
 - GPS Module Command:** A dropdown menu set to 'Coldstart' and a 'Transmit' button.
- Pressure Sensors:**
 - Measurements:** Airspeed, Altitude, and Climb Rate, each with a text input field and a unit of [m/s] or [m].
 - Buttons:** 'Zero Pressure'.
- Magnetometer:**
 - Measurements:** X Axis, Y Axis, and Z Axis, each with a text input field and a unit of [mGauss].
 - Reference:** Three text input fields for Reference values, each with a unit of [mGauss].

Figure 6.13 Sensors Tab

The *Sensors* tab is shown in Figure 6.13. The *Inertial Measurement Unit* group box displays the rate gyroscopes and the accelerometer measurements. The *Zero Gyros* and *Zero Accelerometer* buttons are legacy functions and were not used. The *Pressure Sensor* group box displays the measured airspeed, altitude and climb rate. The *Magnetometer* group box displays the magnetometer measurements. The *GPS* group box displays the *DGPS Status*, *Geodetic LLH Position*, *Sigma*, *Inertial Velocity* and *Inertial Position*. The *GPS Status* box shows the status of the NovAtel base station, Rover RTK status, the *Fix Type*, the number of *Satellites Used* and *Satellites Visible* and the *Differential Age (Diff Age)*. The *Differential Age* box shows how recently the rover module processed a DGPS correction packet. The corresponding *Sigma* boxes for the measured *Latitude*, *Longitude* and *MSL* boxes shows the 1 sigma accuracy the NovAtel's RT-2 L1TE RTK solution.

6.3.5 Actuators, Actuator Setup and Diagnostics Tab

The *Actuators* tab shows the actuator commands transmitted to and from the servo board in aero and particular units. The *Actuator Setup tab* provides a means for calibrating the servos. In this tab each servo can be commanded from the ground station and allows the user to update the mechanical gain matrix, mechanical offset vector and the mixing matrix. The *Diagnostics* Tab provides debugging information

6.4 Summary

This chapter presented the selected airframe and gave an overview of the different components of the avionics and ground station tabs. Figure 6.14 shows a photo taken at HRF of the complete system after a flight test.



Figure 6.14 Photo of the Aircraft and Ground Station after a Flight Test at HRF

Chapter 7

Landing System Design

This chapter defines the proposed autonomous landing strategy. Section 7.1 starts off with an overview of a textbook landing strategy followed by a discussion on the landing strategy that was implemented. Section 7.2 discusses the different landing phases in detail, defines the longitudinal and lateral landing trajectories as well as the landing trajectory parameters, and concludes with the landing state machine.

7.1 Autonomous Landing Strategy

During flight tests many hours were spent at Helderberg radio flyers club (HRF). During this time, it was always interesting to see human pilots land their aircraft. For these pilots, timing is very important. A typical pilot at HRF would manoeuvre his aircraft metres above the runway and perform a hold-off (a state where the aircraft flies parallel to the runway with a constant airspeed and altitude) and then reduce the aircraft's motor power until the aircraft gently sets down. This non-linear aircraft landing behaviour and timing that the pilot has developed over time to land the aircraft is very difficult to convert into a linear auto-landing system. The goal for this project is to implement a conventional landing strategy found on airfields where small types of aircraft (i.e. Cessna size) land.

A brief summary of a landing strategy for a conventional small aircraft (Cessna size) is given by [30]. The landing approach starts after the base to final turn (after the pilot aligns the aircraft with the runway). At the start of the landing approach the pilot adjusts the final landing flap settings and establishes a constant descent rate (with a typical landing flight path angle ranging between 3.3 and 15 degrees). The landing approach airspeed is usually specified by the manufacturer of the aircraft. In the absence of a specified landing approach speed, an approach speed of 1.3 times the stall speed of the aircraft should be used (rule of thumb in the aviation industry). Once the aircraft is at the desired altitude above the ground the round-out (flare) manoeuvre is started. The round-out is a slow transition from the current descending flight path to one that is parallel with, and a few metres above, the runway. Once in this state the aircraft enters the next landing phase, called the hold-off phase. The aim of this phase is to control the descent rate so as to land the aircraft gently

on the runway. Once the aircraft is in the hold-off phase the pilot slowly increases the angle of attack (AoA) by applying back elevator pressure. This causes the nose of the aircraft to rise to the desired landing attitude. When the AoA is increased, lift is also increased and the sink rate decreases. It is thus also important for the pilot to decrease the power to idle during the round-out so that the airspeed also gradually decreases as the AoA is increased. This roughly cancels the lift increase caused by the back elevator. In the final stage of the hold-off manoeuvre the aim is to obtain a desired landing sink rate and attitude. A gentle touchdown occurs as a controlled stall on the runway as the airspeed is continually decreased to stall speed by increasing the AoA gradually.

In this project a modified stabilised landing approach is implemented. A stabilised landing approach is an approach where the pilot establishes a constant glide path and maintains it to a predetermined location on the runway. If the pilot doesn't perform a round-out the aircraft will strike the aiming point. This situation is graphically illustrated in Figure 7.1. The landing approach that the autopilot will execute is as follows: After the base to final turn, illustrated in Figure 7.2, the aircraft starts its landing approach by gliding on a predetermined glide slope (first glide slope). The first glide slope is used to rapidly decrease the altitude of the aircraft and is a result of the testing environment (refer to Section 9.1.3). Then when the aircraft reaches a desired distance downrange it transitions to the second glide slope (or landing glide slope) and reduces its airspeed to 1.4 times the aircraft stall speed. This trajectory is maintained until touchdown occurs. The final pitch attitude on touchdown is a function of the aircraft's state on its second glide slope.

When the aircraft is on the final approach and settles on the landing glide slope, the longitudinal landing accuracy is expected to be a function of the estimated altitude error and the landing glide slope gradient. The shallower the landing glide slope is, the larger the longitudinal landing error will be from the intended touchdown point for an estimated altitude error (illustrated in Figure 8.6 on page 111). However with a steeper landing glide slope the longitudinal landing error will be reduced at the cost of a harder landing. In the modified landing approach, the landing glide slope is chosen to be shallow for a first iteration, so that the aircraft descends slowly and lands with a sink rate that would not cause damage to the aircraft's undercarriage. The stall speed of the aircraft in flap configuration was found to be 10 m/s in Section 9.1.1, thus the touchdown airspeed is chosen as 14 m/s . The landing glide slope is chosen as 3.3° in Section 9.1.2 based on practical tested touchdown sink rates and accelerometer landing spikes. The resulting touchdown sink rate from the chosen touchdown airspeed and landing glide slope is 0.8 m/s .

An exponential flare manoeuvre after the first \ glide slope to land the aircraft was also investigated and flight tested. However this method uses a very shallow landing gradient that increases the

longitudinal landing error for a given error in estimated altitude. Since this dissertation is mainly focused on accurately landing the aircraft, the modified stabilised approach is used.

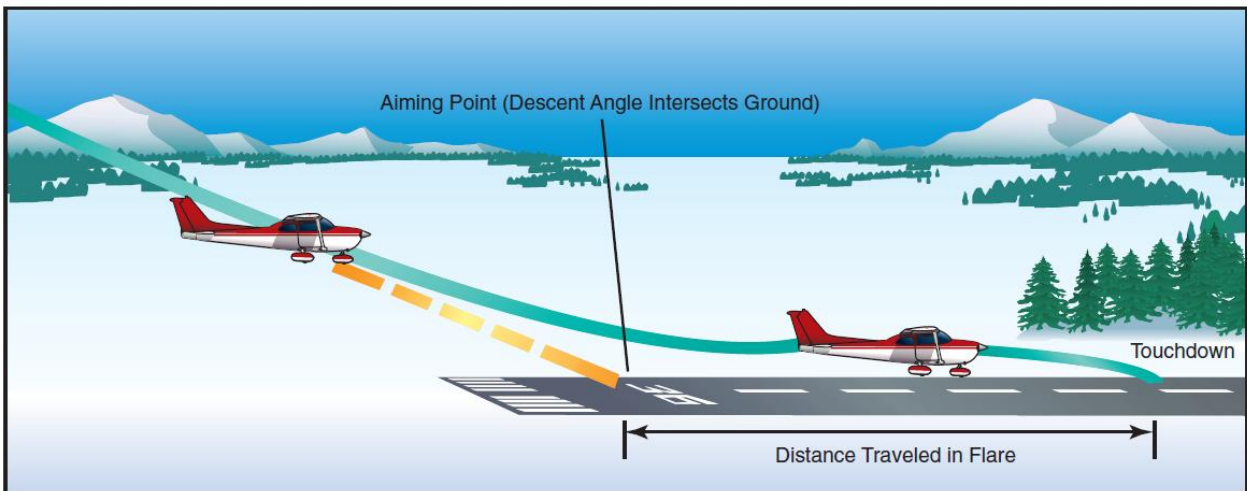


Figure 7.1 Stabilised Landing Approach [30]

During the landing approach tight lateral track regulation will ensure that the aircraft is aligned with the runway in the final landing phases. Crosswind landing and ground control of the aircraft after a landing are beyond the scope of this project and are considered to be future extensions of the project. For the flight control system to follow a fixed trajectory in space, tight requirements on reliability and noise characteristics are placed on the sensors on board the aircraft, since the sensor measurements are directly used in low-level high-bandwidth controllers. In this project a high-precision differential GPS is used to accurately determine the aircraft's position in the inertial frame. The remainder of sensors used in this project are low-cost off-the-shelf sensors with reasonable performance in accuracy and noise characteristics.

7.2 Landing State Machine

Figure 7.2 illustrates a conventional left-hand landing pattern. The safety pilot is responsible for guiding the aircraft via remote control to the entry area (dashed-line block) indicated in Figure 7.2 and for arming the autopilot. Once the autopilot is armed the autonomous landing state machine is initialised. The state machine flies the remainder of the landing pattern at constant altitude and airspeed, until the aircraft reaches the approach point. The end goal of the landing pattern is to regulate the airspeed and altitude for a good landing approach on the final leg.

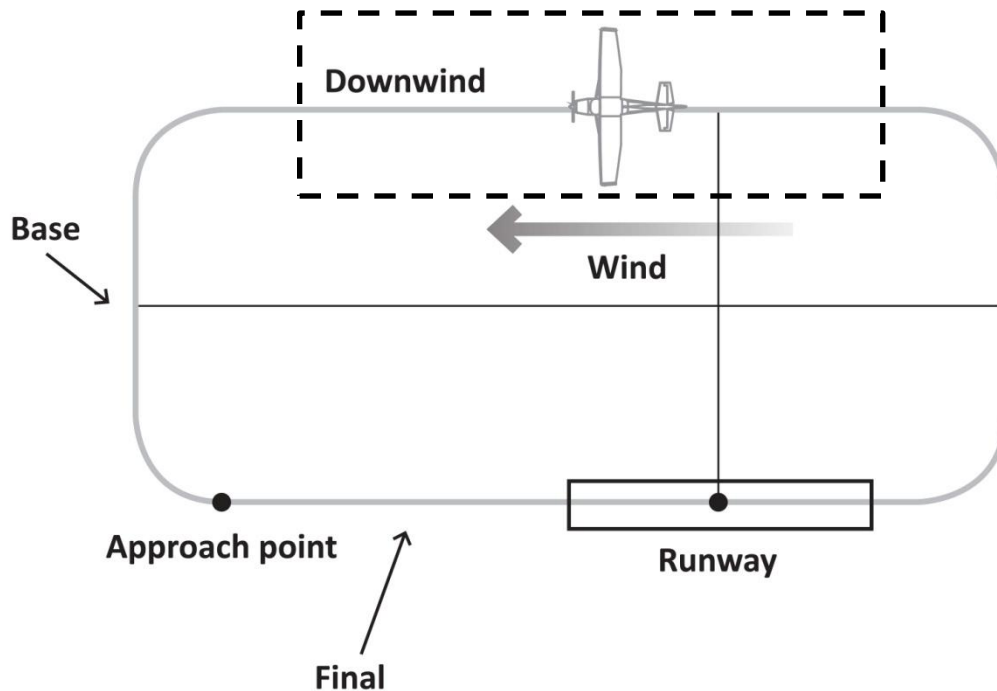


Figure 7.2 Conventional Landing Pattern [30]

Once the aircraft passes the approach point, the autopilot executes the landing phases outlined in Figure 7.3. Each of the four landing phases is discussed in detail, followed by the landing trajectory and parameters, and lastly the chapter is concluded by a detailed landing state machine.

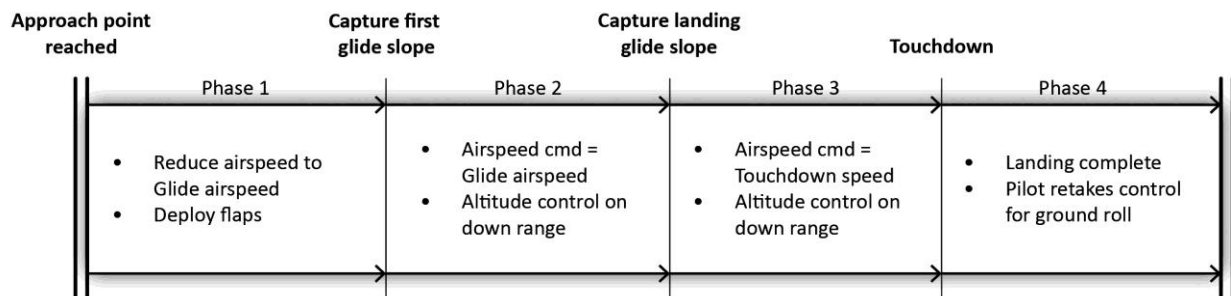


Figure 7.3 Landing Phases Flow

Landing phase 1:

In Phase 1, after the base to final turn, the autopilot reduces the airspeed to the landing glide speed and deploys the flaps. Flaps in the landing phase provide the following advantages by:

- Generating more lift, allowing for a lower landing airspeed.
- Generating more drag, allowing a steeper glide slope angle without any airspeed increase.
- Decreasing the length of the ground roll.

The sudden decrease in airspeed and the gradual extension of the flaps creates transient effects in altitude and pitch angle. The landing trajectory is designed so that the transient effects expire before the aircraft enters Phase 2.

Landing phase 2:

In Phase 2 the aircraft captures the first glide slope and starts its constant descent by controlling the altitude-based distance from the touchdown point (downrange).

Landing phase 3:

In Phase 3 the aircraft captures the second glide slope and reduces its airspeed on the new glide slope to touchdown speed. Transient motion is expected during the change in glide slopes; the trajectory is thus designed such that the transient motion does not affect the landing accuracy.

When the aircraft is near the end of Phase 3 (below three metres in altitude) the aircraft should be aligned with the runway and should land with a near-zero bank angle. If the autopilot is still correcting its lateral track as a result of wind conditions, the guidance controller will compensate by banking the aircraft to reduce the lateral track error. If the resulting landing bank angle is too large (15° for the airframe used) the wing tip could strike the ground. To avoid this potential situation the reference bank angle command is limited to $\pm 5^\circ$ and the roll-rate integrator is also limited to prevent integrator wind-up when the aircraft is below three metres in altitude near the end of Phase 3. With this strategy in place the guidance controller still has the ability to make small lateral error corrections but is not able to bank the aircraft excessively, thus a percentage of the lateral landing accuracy is traded for a safer landing.

Landing phase 4:

In the final stage of Phase 3 just before landing, the landing condition in the state machine is set as follows: once the aircraft reaches an altitude below one meter (moments before touchdown) a spike in the Z_B -axis accelerometer that exceeds the touchdown threshold (-20 m/s^2) signals that the aircraft has landed. On touchdown the FCS sets the elevator setting to the elevator command just before touchdown, cuts the throttle, halves the current flap setting (to dump lift and to keep the wheels on the ground), sets the rudder command to zero and sets the reference roll-angle

command to zero in order to keep the wings level during the ground roll until the safety pilot retakes control.

The landing state machine stops executing commands after touchdown and enters a waiting condition until the safety pilot retakes control. Ground controllers were not implemented since in a precision landing a capturing device will most probably be used to arrest the aircraft (i.e. an arrestor on an aircraft carrier deck).

Landing trajectory

The longitudinal and lateral landing trajectories are illustrated in Figure 7.4 and Figure 7.5 respectively.

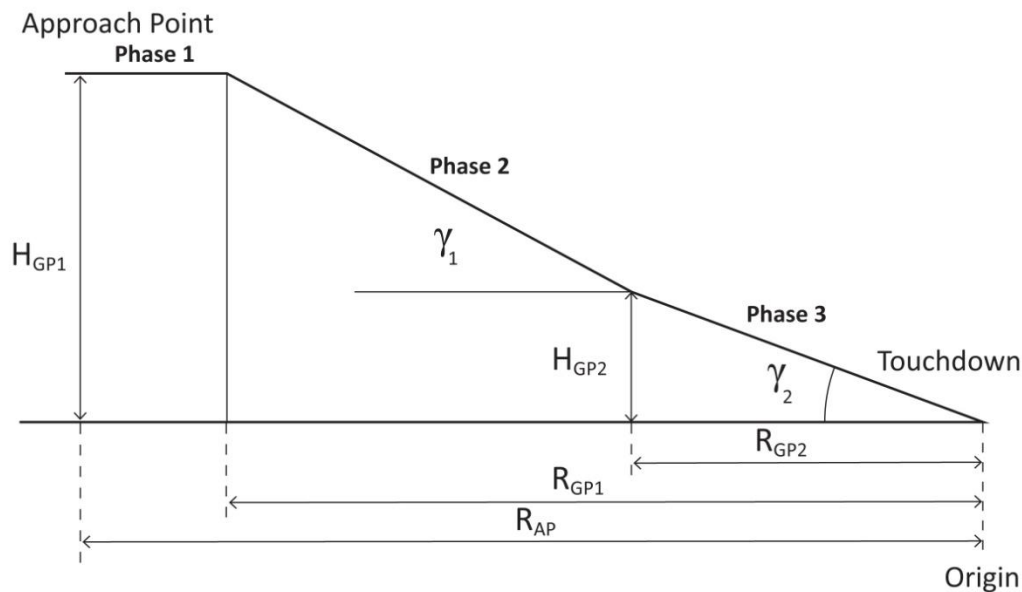


Figure 7.4 Detailed Longitudinal Landing Path

The longitudinal landing path variables are defined below:

- Altitude (H_{GP1}, H_{GP2}): the starting altitude of the aircraft at the approach point (start of the first glide path) and on the second glide path respectively.
- Approach range (R_{AP}): the range from the origin after the base to the final turn.
- Glide path range (R_{GP1}, R_{GP2}): the range from the origin where the two glide paths start.
- Glide path angles (γ_1, γ_2): the two desired angles of descent.
- Origin: the aiming point.

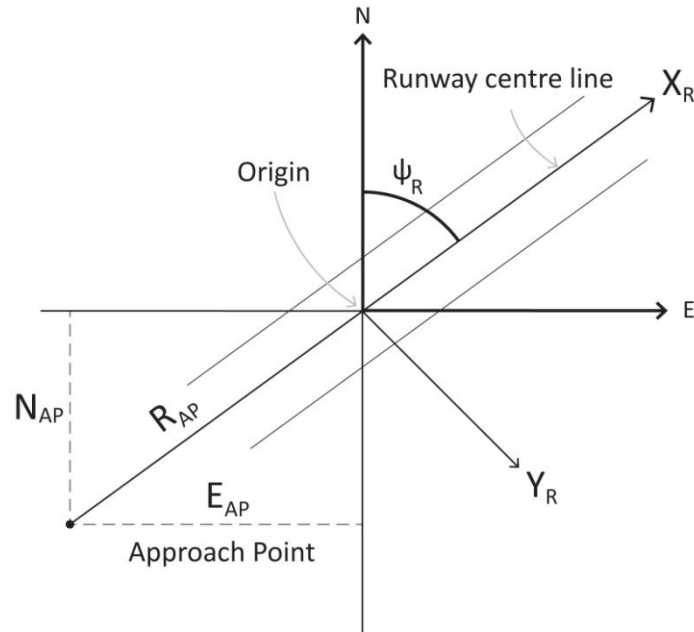


Figure 7.5 Lateral Landing Path

After the base to final turn is completed the aircraft passes the approach point (AP). The lateral approach parameters are:

- path heading angle : ψ_R
- North displacement from approach point: $N_{AP} = R_{AP} \cos \psi_R$
- East displacement from approach point: $E_{AP} = R_{AP} \sin \psi_R$
- altitude at approach point: $H_{GP1} = R_{GP1} \sin \gamma_1$

The values of the parameters listed above are given in Table 7.1.

Table 7.1 Landing Parameters

Longitudinal landing path variables	Values
H_{GP1}	22 m
H_{GP2}	6 m

R_{AP}	400 m
R_{GP1}	240 m
R_{GP2}	120 m
γ_1	6.6°
γ_2	3.3°

Lateral approach parameters	Values
ψ_R	-14.1°
N_{AP}	380 m
E_{AP}	97 m

The origin of the inertial axis system (defined in Section 3.1.1) is the point where the aircraft sensors are initialised on the runway before take-off. With the runway axis not aligned with the inertial axis system, a transformation matrix is required to relate the waypoints in the runway axis system to the inertial axis system. The following transformation matrix is used:

$$\begin{bmatrix} X_E \\ Y_E \end{bmatrix} = \begin{bmatrix} \cos \psi_R & -\sin \psi_R \\ \sin \psi_R & \cos \psi_R \end{bmatrix} \begin{bmatrix} X_R \\ Y_R \end{bmatrix} \quad (7.1)$$

where (X_E, Y_E) and (X_R, Y_R) are points in the inertial and runway axes respectively with ψ_R the runway heading angle defined in the inertial axis system.

Landing state machine

Finally the landing state machine is illustrated in Figure 7.6.

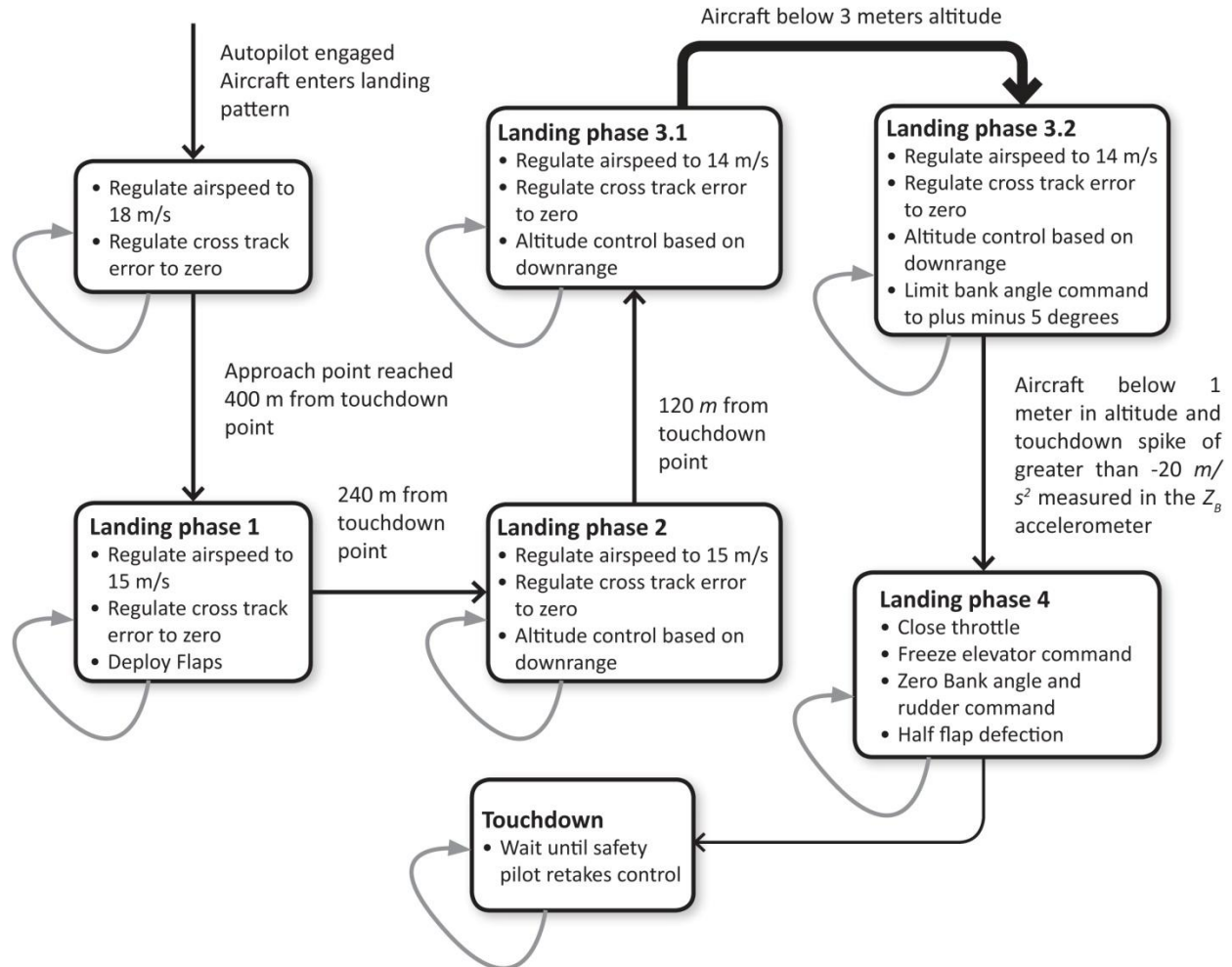


Figure 7.6 Landing State Machine

7.3 Summary

This chapter presented a brief summary of a conventional pilot handbook landing strategy and highlighted how the landing strategy employed in this project differs from the conventional landing strategy. This chapter covered the landing strategy used, dividing it into four different landing phases, followed by the longitudinal and lateral landing trajectories and concluded with a detailed landing state machine.

Chapter 8

Non-Linear Landing Simulation

This chapter starts by discussing the simulation environment and introduces the reader to the concept of software-in-the-loop simulation and hardware-in-the-loop simulation. The simulation environment is used as a tool to determine the control actions of the FCS in a landing simulation with different wind conditions and to obtain an indication of the landing accuracy of the FCS in the real world.

8.1 Overview of Simulation Environment

Simulations in Simulink give insight into the controller's performance and also test the simplifications and assumptions made during to the controller design process in Chapters 4 and 5. In this project there are two different types of simulation setups namely: software-in-the-loop (SIL) and hardware-in-the-loop (HIL).

8.1.1 Software-in-the-Loop Simulation

The SIL simulation is used to test individual controllers as well as the performance of the flight control system in performing landing manoeuvres under different wind and system noise conditions. The SIL simulation environment provides an easy environment to alter the system noise parameters (the sensors on board the virtual aircraft), alter wind parameters and generate random wind gusts during crucial landing phases. The SIL simulation setup also provides an easy environment to perform Monte Carlo simulations. The ability of the FCS to land the virtual aircraft autonomously can be thoroughly tested and evaluated in SIL simulations before performing HIL simulations. The simulation environment block diagram is shown in Figure 8.1.

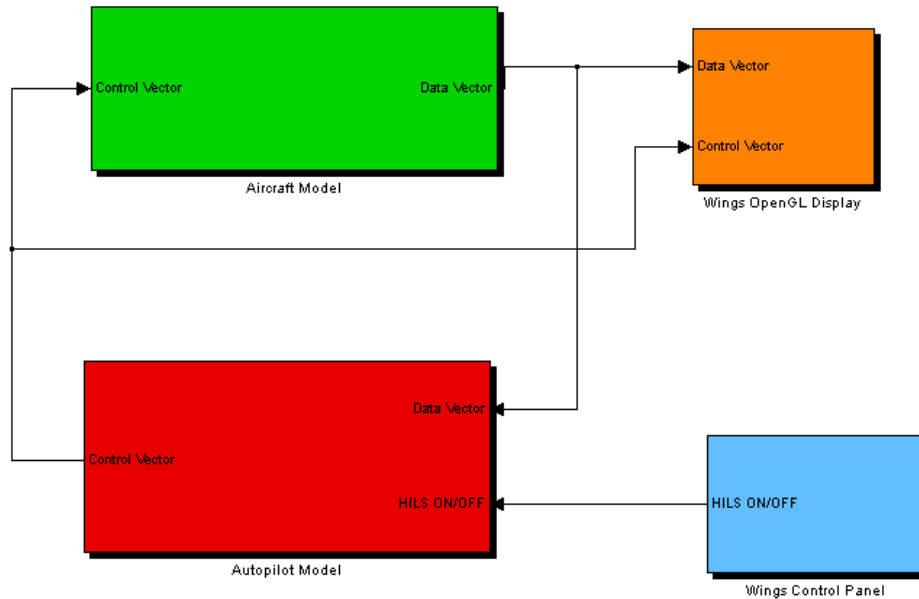


Figure 8.1 Non-Linear Simulation Environment

The actuator commands (*Control Vector*) generated by the *Autopilot Model* and the current state of the aircraft are used in the *Aircraft Model* to propagate the next time step of the *Data Vector* (aircraft states). The *Wings OpenGL Display* block receives the aircraft's states and displays the aircraft in a three-dimensional environment. The *Wings Control Panel* is used to toggle between HIL and SIL simulation modes. The *Aircraft Model* block houses the six degrees of freedom block, the aerodynamic model (developed in Chapter 3), the thrust model (developed in Chapter 3), the runway model, the gravitational model and the wind model. The six degrees of freedom block calculates the aircraft's states based on the outputs of the aerodynamic model, thrust model, runway model, gravitational model and wind model. The *Autopilot Model* block houses the software implemented kinematic state estimator, the different flight controllers and the landing state machine. The flight controllers and landing state machine algorithms are coded in a C file which forms part of the FCS software that is programmed onto the OBC.

8.1.2 Hardware-in-the-Loop Simulation

HIL simulation is used as a tool to reduce risk before practical flight tests, to prepare for a flight test and to verify the flight control system's performance with the full non-linear aircraft model. This section gives the reader a brief overview of the HIL simulation testing procedure and physical setup.

In an HIL simulation, the aircraft controllers are tested in such a way that the test environment mimics an actual flight test. The simulation starts off with the aircraft on the ground. Just as in a practical flight test, the estimator needs to be initialised and started. After a manual take-off, controllers are armed in a combination or individually, depending on what is being tested, via the ground station. The ground station provides an interface to communicate with the on-board computer (OBC) and to issue commands to the controllers and update parameters. During a simulated HIL flight, test telemetry data is logged via the OBC on an SD card. The data is then analysed after the simulated flight to verify individual controller performance or the flight control system as a whole.

The main drawback of HIL simulations is that the simulations are not as easily reconfigurable as they are in SIL simulations. Code changes, such as control algorithm changes, require recompiling and programming of the OBC. Parameter changes, such as wind speed and wind gusts, require the simulation to be stopped and restarted. With a manual simulation initialisation (HIL simulation setup), starting and configuring the OBC, followed by a manual take-off, flight test and finally the analysis of the saved data on the SD-card, HIL simulations become time-consuming. Thus HIL simulation verification is the last step before a practical flight test with the flight control system thoroughly tested and evaluated in SIL simulation.

The HIL simulation environment was developed in [29]. With reference to Figure 8.1, the main difference between SIL and HIL simulations is that the flight control system is implemented on the actual hardware, in other words sensor data is created by the *Aircraft Model* in the non-linear simulation environment in Simulink and is transmitted to the OBC via an HIL distribution board. The OBC executes pre-programmed control algorithms on the sensor data to calculate actuator commands based on the current flight envelope. The actuator commands are then transmitted to the non-linear simulation environment in Simulink via the HIL distribution board. In Simulink the aircraft's dynamic response to the actuator commands from the OBC is simulated by the *Aircraft Model*, whereafter sensor data is recreated and transmitted back to the OBC. The data flow is illustrated in Figure 8.2 and gives an overview of the HIL setup. For more detailed information refer to [29].

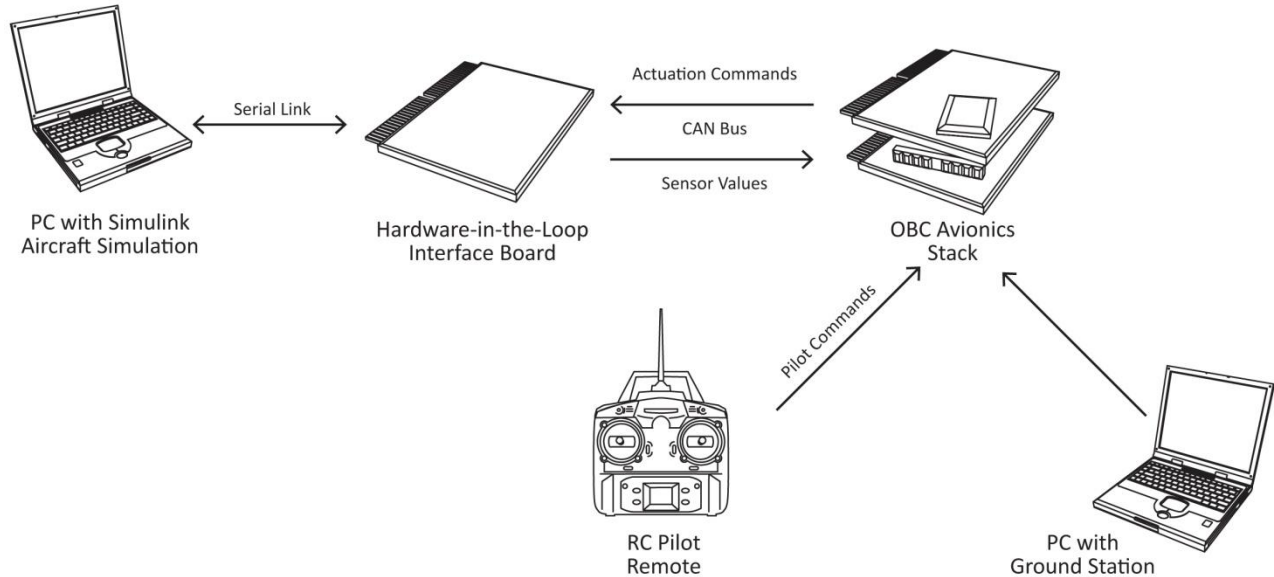


Figure 8.2 Hardware-in-the-Loop Setup Overview

8.2 Non-Linear Landing Simulation

With the controllers implemented and flight tested, the scene is set to analyse the ability of the flight control system to land the aircraft in different simulation environments. To this end, four simulation environments with different sensor noise and wind characteristics are used.

- No noise: This ideal non-linear simulation gives an indication of how well the FCS is able to land the aircraft in an environment with perfect sensors (no estimator) and no wind disturbances. This simulation introduces the simulation environment to the reader and acts as a benchmark.
- Constant wind: This simulation environment considers wind components parallel to the ground with perfect sensors.
- Wind gust: This simulation environment focuses on the aircraft when it is on its second glide slope and within five metres of altitude from the ground. During the aircraft's descent a wind gust is injected into the simulation. Perfect sensors are also used in this simulation environment to determine the FCS actions.
- Windless day: In flight testing, an estimator is used to estimate the aircraft's states from sensors; if the estimated states are delayed or contain an offset, the ability of the FCS to land the aircraft accurately is directly affected. In other words the FCS system can only

control the aircraft as well as the accuracy of the estimated states allows. Thus to gain insight into the statistical ability of the FCS to land the aircraft accurately, the estimator is not included in the loop. Instead real world sensor noise is added to the measured aircraft states. The statistical ability of the FCS to land the aircraft accurately is evaluated by performing the simulated landing a hundred times.

Since landing is a longitudinal control exercise and crosswind conditions are beyond the scope of this document, the landing analysis focuses mainly on the longitudinal landing aspect. In each of the simulations, the aircraft is initialised parallel to the runway on the downwind leg, with the runway axis aligned with the inertial axes, as illustrated in Figure 7.2. The ability of the FCS system to land the aircraft is based on the following figures of merit:

- The ability to track the reference altitude on the second glide slope. This performance index consists of two figures of merit: the maximum altitude tracking error and an RMS tracking error. The maximum tracking error is self-explanatory whereas the RMS tracking error gives an indication of how well the aircraft has followed the reference altitude. The RMS tracking error is calculated by subtracting the aircraft's altitude from the reference altitude when the aircraft is below three meters in altitude. This tracking error is squared, summed and divided by the total number of data points, before taking the square root of the result. In the fourth simulation environment the standard deviation, mean and maximum tracking error is used as a performance index.
- The ability to land the aircraft on the aiming point. This performance index evaluates the FCS's ability to land the aircraft accurately. The aiming point in simulation is located at the origin of the runway (0.0) with the aircraft's direction of flight in the north direction. The performance index is the distance from the desired touchdown point longitudinally and laterally to the origin of the runway. A positive longitudinal error indicates that the aircraft landed after the aiming point in the north direction. The landing is considered precise if the touchdown point falls in a circle with a diameter of 1.5 m, with the aiming point the centre of the circle. The circle's diameter is the length of the aircraft's fuselage. If the aircraft lands in circle with a diameter of 3 m, the landing is considered relatively accurate. Anything outside a circle with a diameter of 3 m is considered inaccurate. In the fourth simulation environment the landing distance error is expressed as a mean and standard deviation figure of merit from the desired touchdown point.

- Error in landing sink rate. This figure of merit gives an indication of how hard the aircraft is going to land. A zero sink rate error implies that the aircraft has landed at the desired sink rate whereas a negative sink rate indicates a softer landing. In the fourth simulation the sink rate is expressed as a standard deviation from the nominal sink rate in the Ideal simulation.
- The landing pitch angle. A positive pitch angle implies that the aircraft landed nose-up. In the fourth simulation environment the maximum and minimum magnitude of the pitch angles are used as a figure of merit as well as the mean and standard deviation of the landing pitch angle.

Note that the simulation environments do not include the ground effect. The ground effect was ignored based on the following arguments: On the maiden flight test the safety pilot was asked to fly in and out of the ground effect (ground effect occurs at an altitude of less than one wing span [31]). The pilot reported that aircraft felt the same in and out of the ground effect. Additionally, high-wing airplanes are less affected by the ground effect than low wing planes [32].

8.2.1 Ideal Non-Linear Landing Simulation

The landing flow diagram from Chapter 7 is restated in Figure 8.3 for convenience. The landing flow diagram is conceptually translated to the Simulink simulation environment in Figure 8.4 and Figure 8.5.

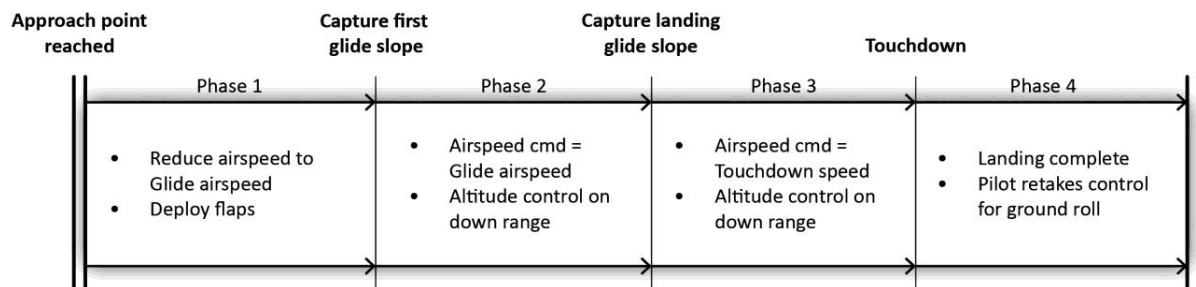


Figure 8.3 Landing Transition Phases

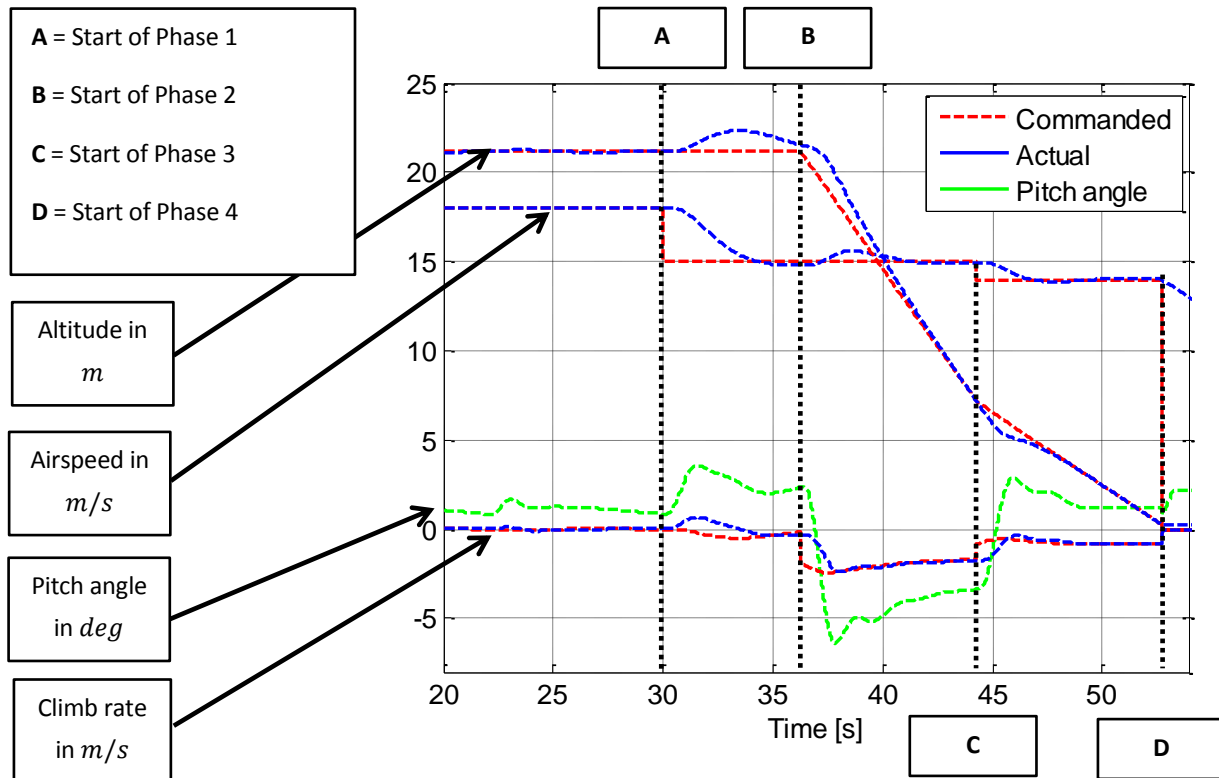


Figure 8.4 Landing Phases

Figure 8.4 illustrates the different landing phases and states, while Figure 8.5 illustrates only the landing states that are of interest. The landing states have the following convention: the red dashed line represents the commanded states, the solid blue line represents the actual state and the green line represents the pitch angle. On the y-axis from top to bottom, are the commanded and actual altitude in m , commanded and actual airspeed in m/s , the pitch angle of the aircraft in degrees and the commanded and actual climb rate in m/s .

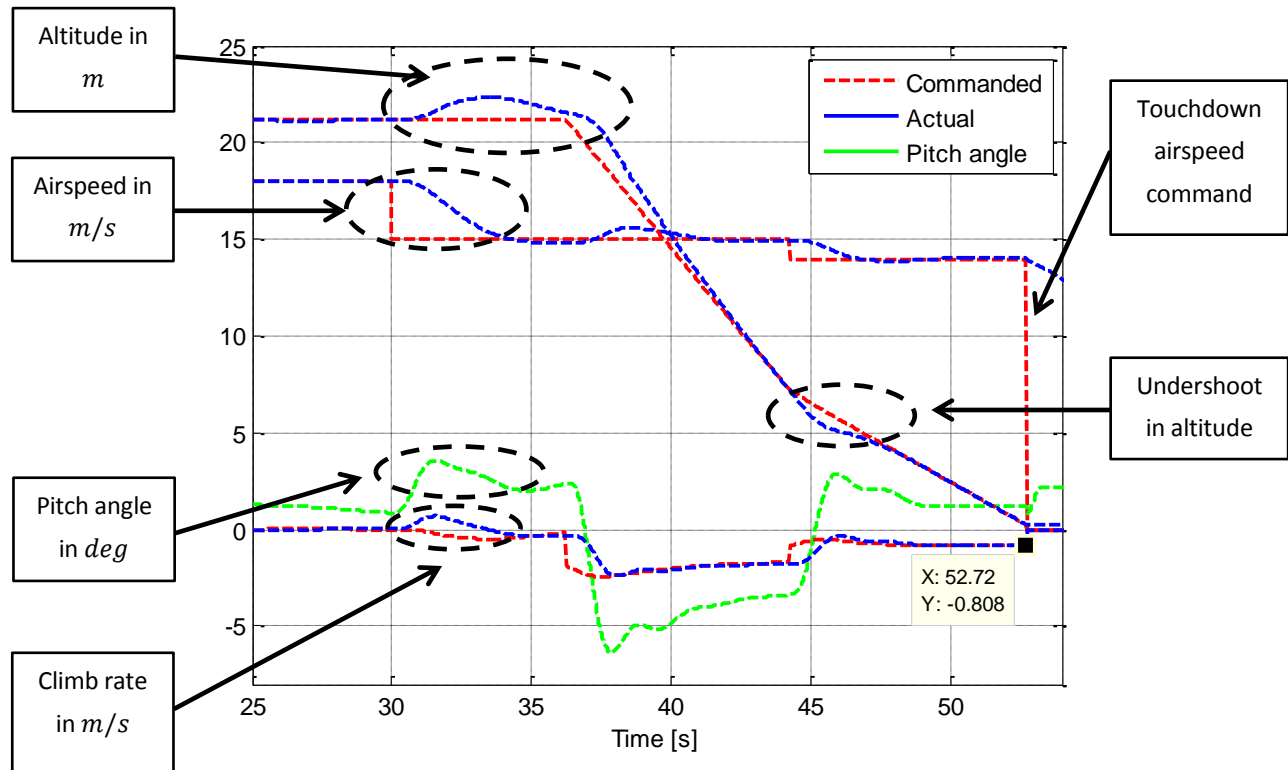


Figure 8.5 Aircraft Landing States

Ideal Simulation Interpretation

In Figure 8.5 the aircraft reaches the approach point at 22 s, the start of Phase 1. The FCS starts the state machine in Figure 8.5 by reducing the airspeed to glide airspeed and deploys the flaps. The highlighted airspeed section in Figure 8.5 shows the change in the level-flight airspeed command to the glide airspeed command. The subsequent rise in altitude, climb rate and pitch angle highlighted on the left in Figure 8.5 arises from the method in which the LQR controller reduces airspeed. The LQR controller uses gravity to decrease the airspeed of the aircraft by pointing the aircraft's nose up and reducing thrust. In Phase 2, the FCS captures the first glide slope in approximately three seconds. Phase 3 starts when the aircraft captures the second glide slope and reduces the airspeed to touchdown speed. A slight undershoot can be seen after which the aircraft tracks the second glide slope until touchdown. Touchdown is indicated on Figure 8.5 with a data tip at 52.72 s. The data tip displays the reference touchdown sink rate. Note that on touchdown the airspeed command is also set to zero.

Flight Control System's Performance

- In the simulation results illustrated in Figure 8.5, the FCS had a maximum tracking error of 0.78 m on the second glide slope, with an RMS tracking error of 0.076 from five metres. A smaller RMS tracking error means a better tracking ability. If the highlighted undershoot in altitude in Figure 8.5 is not taken into account, the RMS error for the last three metres above ground is found to be 0.002 . This result indicates that the aircraft is on the desired trajectory near the ground. When the RMS error figure of merit is used, the last three metres of the second glide slope are considered.
- The aircraft landed at $(0.1, -0.21)\text{ m}$; this result indicates that the aircraft landed precisely. The landing accuracy in this simulation can be attributed to the following factors:
 - Since the altitude controller is a type 1 system there exists a finite steady-state tracking error for a reference altitude ramp input which shifts the landing point. This landing error is reduced to nearly zero by adding a reference climb rate as described in section 5.1.2. In this simulation a steady state tracking error of approximately 0.005 m shifted the landing point by 0.1 m on the 3.3° glide slope.
 - A bigger landing error concern in practical landings is if there is an error in the estimated altitude. This concept is illustrated in Figure 8.6: if the estimated altitude error is 0.02 m and the landing glide slope angle is 3.3° , the touchdown point will shift by 0.35 m . This landing error can be reduced by increasing the landing glide slope, at the cost of landing with a larger sink rate which the landing gear has to absorb.

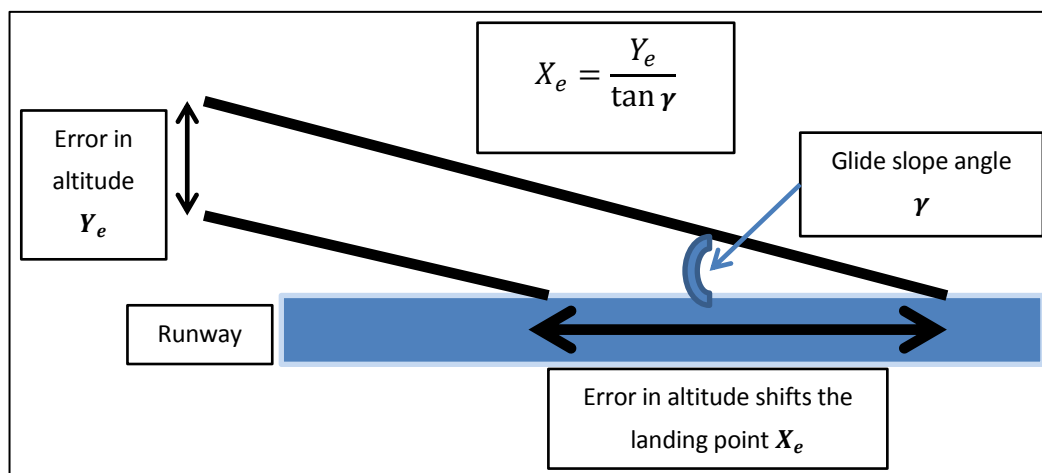


Figure 8.6 Landing Point Shift due to an Error in Altitude

- The lateral landing error is a result of the 2% settling time of 21.5 s of the guidance controller. Near touchdown the aircraft is in the 2% settling tolerance band. The small lateral landing error is acceptable for practical flight testing and can be reduced if needed by increasing the gain of the guidance controller.
- The nominal sink rate is -0.8 m/s and the landing sink rate error is 0.08 m/s . This result indicates that the aircraft landed with the desired sink rate, and this parameter indicates how hard the aircraft landed. An upper bound on the sink rate that will not cause damage to the aircraft is investigated in Section 9.1.2.
- In this simulation the aircraft landed with a positive pitch angle of 1.6° . The small touchdown pitch angle is drawback from using flaps in the landing, since the main wing produces more lift which results in the aircraft flying at a lower AoA angle.

8.2.2 Constant Wind: Non-Linear Landing Simulation

By convention, pilots approach the runway for a landing with a headwind. By landing the aircraft in the direction of the wind, the ground speed and ground roll of the aircraft is reduced. This simulation analyses the effect of headwind on the landing performance of the FCS. Due to the orientation of the runway at HRF, on some occasions practical landing tests were (of necessity) performed with a tailwind and thus the FCS's ability to land the aircraft with a tailwind was also analysed.

In this landing simulation scenario, the focus is on the aircraft when it reaches the second glide slope (having flown the entire landing pattern). In this simulation a headwind of 5 m/s is used and a similar simulation is performed with a tailwind of 2 m/s . In each of the two simulations the magnitude of the wind corresponds to conditions experienced during practical landing tests. The reason for the different magnitudes is that at HRF the aircraft could only land autonomously in the South to North direction of the runway. If the aircraft had landed in the North to South direction (opposite direction) it would have had to fly over a large highway and power lines. Thus if the tailwind was too strong on South to North direction of the runway, the safety pilot would retake control of the aircraft and land it on the other side of the runway with a headwind. Slight crosswind conditions were rarely experienced during practical landing tests, so they are not analysed in this simulation.

Simulation Interpretation: Headwind

Figure 8.7 illustrates the airspeed, altitude, pitch angle and ground speed during Phase 3 (aircraft on the second glide slope). The constant wind effect is evident in the difference between the airspeed and ground speed. In this simulation the FCS's ability to land the aircraft is expected to be similar to the Ideal simulation.

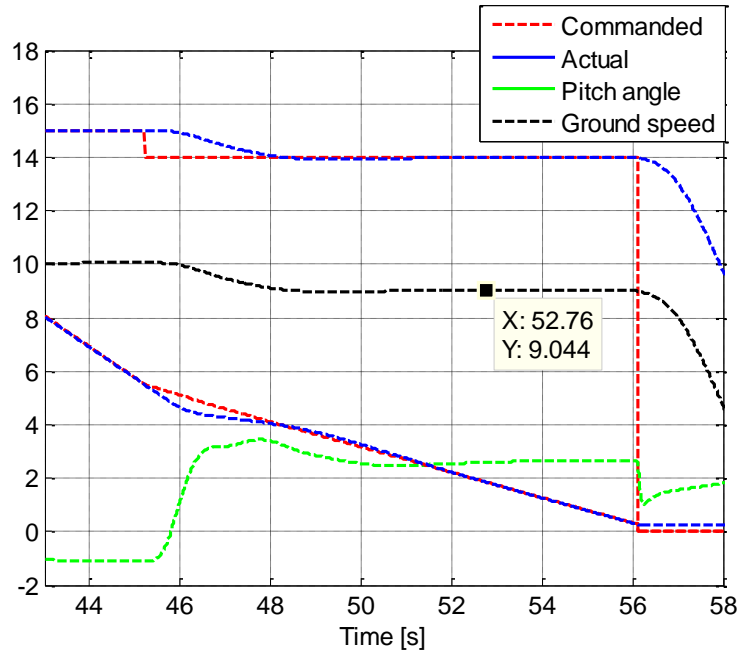


Figure 8.7 Headwind During Landing

Flight Control System's Landing Performance: Headwind

- The FCS had a maximum tracking error of 0.45 m which is smaller than the tracking error in the ideal case and tracked the landing glide slope with an RMS tracking error of 0.005 .
- The aircraft landed at $(-0.05, -0.21)\text{ m}$. This result indicates that the FCS achieved a precision landing. The slight change in longitudinal touchdown point relative to the Ideal simulation is a result of a steady-state error due to the headwind.
- The landing sink rate error is -0.31 m/s which indicates that the aircraft landed more softly than the Ideal landing.
- The aircraft landed with a positive pitch angle of 2.64° . This result is larger than the landing pitch angle in the Ideal simulation since the angle of descent will be shallower because of the decreased ground speed.

- The main advantage in landing in a headwind is the lower ground speed (i.e. longer settling time) and the larger landing pitch angle.

Flight Control System's Landing Performance: Tailwind

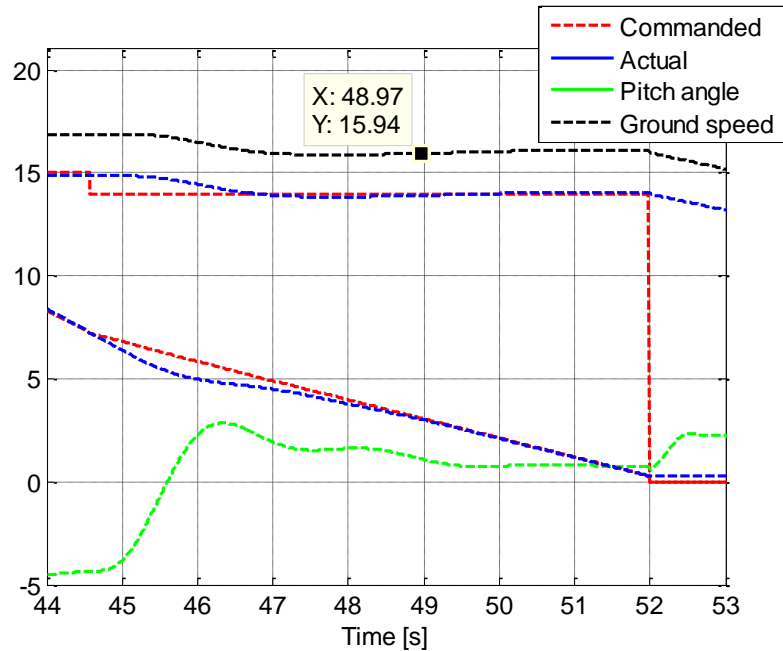


Figure 8.8 Tailwind During Landing

- The FCS had maximum tracking error of 0.88 m which is slightly larger than in the Ideal simulation and tracked the landing glide slope with an RMS tracking error of 0.03 .
- The aircraft landed at $(-0.07, -0.21)\text{ m}$. This result indicates that the FCS achieved a precision landing. The slight change in longitudinal touchdown point relative to the Ideal simulation is a result of a steady-state error due to the tailwind.
- The landing sink rate is error is 0.09 m/s and indicates that the aircraft landed slightly harder than in the Ideal case.
- The aircraft landed with a positive pitch angle of 0.8° .
- A tailwind produces the opposite effect in ground speed and pitch angle to the headwind.

8.2.3 Wind Gust: Non-Linear Landing Simulation

In this simulation environment, the aircraft is on the second glide slope near the ground. A wind gust of 3 m/s is injected into the simulation in the north direction (tailwind gust) via a low pass filter with a time constant of 2.5 s . The aim of this simulation is to investigate how the disturbance affects the ability of the FCS to land the aircraft. A second simulation investigates the effect of a wind gust travelling in the south direction (headwind gust) on the FCS. Wind gusts in the east and west (crosswind gust) directions cause the aircraft to weathervane into the direction of the wind gust which will cause the aircraft to land at a crabbed angle. A third simulation (similar to the previous two) investigates the effects of a wind gust in the east direction.

The chosen longitudinal wind gust magnitude and time constant corresponds well to the MIL-F-8785C Dryden model standard for take-off and landing operations for a manned aircraft in light turbulence. The calculated Dryden model longitudinal wind gust magnitude is 2.2 m/s and it has a time constant of 2 s for an aircraft 4 m above the ground, travelling at an airspeed of 14 m/s . The longitudinal wind gust parameters are also used for the lateral wind gust parameters. This is however not strictly correct but it gives a good enough indication of the FCS landing control actions, which is the focus in this section.

Simulation Interpretation: Tailwind Gust

Figure 8.9 illustrates the airspeed, pitch angle, altitude and ground speed on the second glide slope. The wind gust is injected at 41 s . Since the aircraft is settled on a constant descent angle the sudden wind gust causes the airspeed to decrease and pushes the aircraft downwards resulting in more a negative climb rate. The FCS compensates by increasing the pitch angle momentarily to reduce the climb rate. Once the climb rate is within bounds, the FCS corrects the airspeed by pitching the aircraft's nose downwards to increase the airspeed (using gravity coupling) while simultaneously increasing the thrust to achieve the desired airspeed.

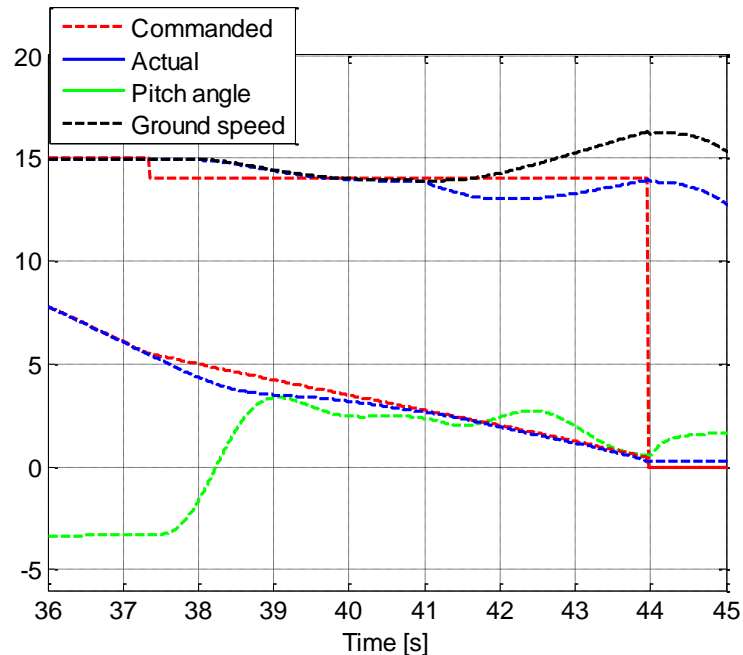


Figure 8.9 Tailwind Gust

Flight Control System's Performance: Tailwind Gust

- The resulting maximum track error is 0.78 m and the RMS tracking error for the last three metres is 0.137 . This result indicates that the aircraft has not settled on the desired glide slope after the wind gust disturbance.
- The aircraft landed at $(-2.6, -0.22)\text{ m}$, which indicates that the aircraft landed inaccurately. The decreased longitudinal landing accuracy is explained by the action that the FCS system takes to correct the airspeed. By pitching the aircraft's nose down to compensate for the decrease in airspeed, the aircraft's climb rate is increased which causes the aircraft to descend faster, resulting in a premature touchdown. The wind gust has a minimal effect on the lateral landing accuracy.
- The landing sink rate is error is 0.23 m/s , which indicates that the aircraft landed harder than in the ideal simulation.
- The aircraft landed with a positive pitch angle of 0.6° . In the Ideal simulation the aircraft landed at approximately triple this pitch angle. The near zero landing pitch angle, in combination with the tendency of the FCS to pitch the aircraft's nose downward to gain airspeed after a disturbance, is undesirable in the last stages of landing.

Simulation Interpretation: Headwind Gust

This simulation setup is similar to that of the previous simulation. The main difference is that the direction of the wind gust has changed. The wind gust is injected into the simulation at 41 s. In Figure 8.10 the wind gust causes the airspeed and the climb rate to increase. The flight control system performs in an opposite manner in this situation to that in the tailwind gust simulation. The FCS momentarily decreases the climb rate by dipping the aircraft's nose. When the climb rate is within bounds, the airspeed is reduced by simultaneously reducing thrust and raising the aircraft's nose.

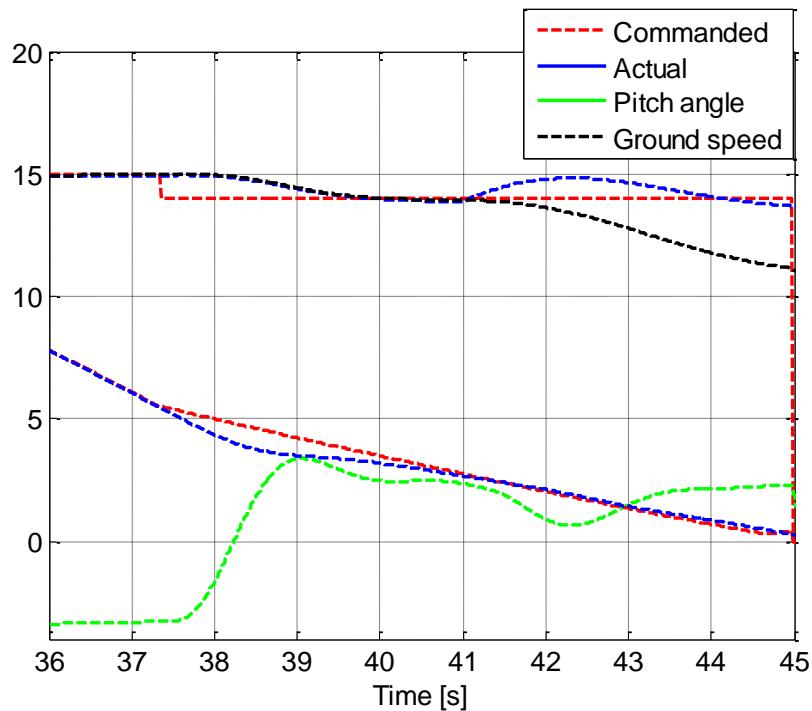


Figure 8.10 Headwind Gust

Flight Control System's Performance: Headwind Gust

- The resulting RMS track error for the last three metres error is 0.12. The result is similar to the RMS error of the Tail wind gust and also indicates that the aircraft has not settled on the desired glide slope. The maximum tracking error for both headwind and tailwind gusts is the same as in the ideal simulation.
- The aircraft landed at $(0.9, -0.2) m$ which indicates that the aircraft landed accurately. Since the FCS increases the pitch angle to compensate for the disturbance in airspeed, the

climb rate is reduced, causing the aircraft to descend slower and landing aft of the aiming point. The wind gust has a minimal effect on the lateral landing accuracy.

- The landing sink rate error is -0.06 m/s , which indicates that the aircraft landed more softly than in the Ideal case.
- The aircraft landed with a positive pitch angle of 2.2° . The tendency of the FCS to pitch the aircraft's nose upwards to compensate for an airspeed disturbance is a good property.

Crosswind Gust

The danger in these wind gusts lies in the landing yaw and bank angles that the autopilot generates to bank the aircraft back onto its trajectory. If the landing yaw angle is too large, and the landing gear cannot handle the side force, a potential crash is imminent. Also, if the aircraft's bank angle is too big near the ground the wing tip could potentially strike the ground before the landing gear does.

A crosswind gust has minimal effect on the landing ability of the FCS system. In a simulation where an east wind gust of 3 m/s was applied three seconds before the aircraft landed, the aircraft weathervaned into the wind gust while keeping the motion of the aircraft in line with runway. The aircraft landed with a yaw angle of -10° and a bank angle of approximately zero degrees. In this simulation a de-crabbing controller is required to align the aircraft's x_B -axis with the runway before touchdown; without the de-crab controller, the landing gear absorbs the side force.

8.2.4 Windless day Landing Simulation

The aim of this simulation environment is to give an indication of the ability of the FCS to land the aircraft in the real world. The simulation noise and wind parameters are listed in Table 8.1 and the simulation properties are defined as follows:

- The autonomous landing simulation is executed a hundred times with realistic sensor noise with different white noise generator seeds.
- The simulation environment excludes aircraft model inaccuracies and sensor offsets.

Simulation: Windless day

Table 8.1 Windless Day: Sensor Noise Characteristics and Wind Effects

Sensor	RMS noise values	Unit
Accelerometers	0.22	<i>m/s</i>
Rate gyroscopes	2	<i>deg/s</i>
Magnetometer	4×10^{-3}	<i>Gauss</i>
Airspeed	0.5	<i>m/s</i>
DGPS 2D position	0.02	<i>m</i>
DGPS altitude	0.02	<i>m</i>
DGPS velocity	0.03	<i>m/s</i>

Wind	RMS noise values	Unit
Gust	North = 0 East = 0	<i>m/s</i>
Constant	North = 0 East = 0	<i>m/s</i>

Simulation Results:

- The maximum altitude tracking error has a mean of 0.79 *m* and a standard deviation of 0.09 which correlates very well with the Ideal simulation.
- The standard deviation for the longitudinal and lateral touchdown point is 0.3 and 0.1 respectively, with a mean of 0 *m* and -0.19 *m* respectively. The non-zero mean of the lateral touchdown point is as a result of the guidance controller which is in the 2% settling band. Out of a hundred landings 98 were precise, 2 were accurate and 0 were inaccurate. The landing spread is shown in Figure 8.11. By using the 68-95-99.7 rule in statistics, the FCS is expected to land the aircraft 95 % of the time accurately (within a circle with a 1.5 *m* diameter) under no-wind conditions.
- The sink rate on touchdown has mean of -0.8 *m/s* and a standard deviation of 0.09. This result correlates very well with the Ideal simulation's touchdown sink rate. Since the

standard deviation in touchdown sink rate is relatively small, the aircraft is expected to land at the intended sink rate.

- The mean and standard deviation for the landing pitch angle is 1.62° and 0.24° respectively, with the minimum and maximum touchdown pitch angles being 0.96° and 2.1° respectively. The standard deviation in pitch angle shows that the aircraft is expected to land with a small pitch angle in the real world under no-wind disturbances.

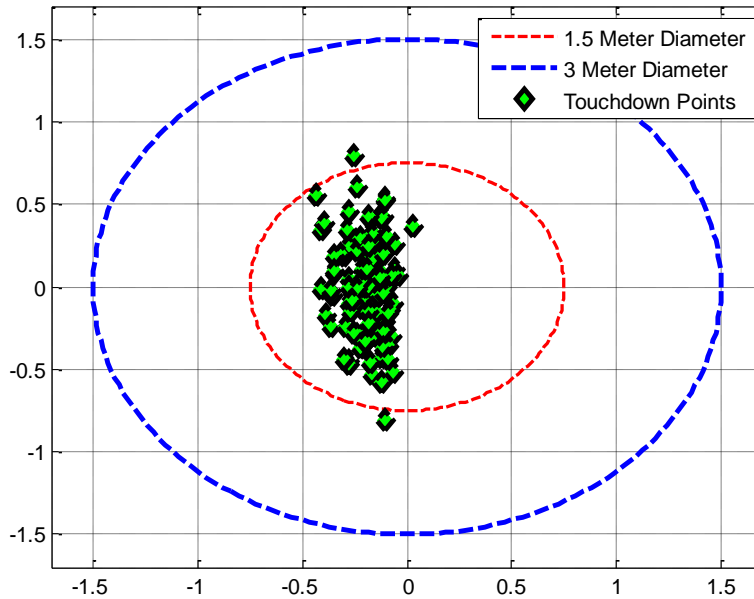


Figure 8.11 Simulated Touchdown Point Landing Spread

8.3 Summary

This chapter introduced the concept of SIL and HIL simulation and gave a brief overview of the data flow between the OBC and a PC running Simulink in an HIL simulation. The ability of the FCS to land the aircraft was then analysed in four different SIL simulation environments. The first simulation environment created a benchmark (Ideal simulation) to compare to the aircraft's landing performance in constant tail- and headwind (second simulation) as well as tailwind, headwind and crosswind gusts (third). The fourth simulation environment simulated the FCS landing performance in the real world on a windless day. Based on a hundred simulated landings, the statistical results indicated that the FCS is expected to land 95% of the time in a circle with a diameter of 1.5 m.

Chapter 9

Practical Flight Tests

This chapter presents the system identification techniques used to determine specific characteristics of the airframe, discusses the design of the landing trajectory and analyses the recorded practical autonomous landing data.

9.1 System Identification

Section 9.1.1 investigates the stall speed of the airframe in clean and flap configuration. Thereafter, in Section 9.1.2, the touchdown threshold that the Z_B axis accelerometer has to exceed to signal a landing to the FCS is investigated. Finally Section 9.1.3 discusses the two glide slopes used in the landing trajectory.

9.1.1 Stall Speed

The aircraft's stall speed was determined theoretically in AVL and tested practically in a flight test. In AVL the aircraft's elevator was constrained to keep the aircraft's pitching moment zero. The airspeed of the aircraft was then systematically reduced in AVL until the AoA reached 14° . The stall speed for the aircraft in clean and flap configuration was found to be:

$$V_{stall_{Clean}_{Theoretical}} \cong 12 \text{ m/s} \quad (9.1)$$

$$V_{stall_{Flap}_{Theoretical}} \cong 10 \text{ m/s} \quad (9.2)$$

For the practical stall speed test the safety pilot was asked to level the aircraft out at 100 m and to close the throttle and maintain altitude. Without flaps the aircraft's pitch angle increased rapidly and experienced a stall. The pilot retook full control and recovered the aircraft by pointing it nose-down until the airspeed was sufficient for normal flight. The practical stall speed of the airframe in clean configuration was found to be

$$V_{stall_{Clean}_{Practical}} \cong 12 \text{ m/s} \quad (9.3)$$

In the stall test with the flaps extended, the aircraft entered a constant glide and did not experience a stall. Only after the flight test data was analysed was it found that the safety pilot had used only

six degrees of elevator deflection. The practical stall speed with the flaps extended was not retested. With a good match between the theoretically and practically tested stall speed of the airframe in clean configuration, the predicted AVL stall speed and flight test for the aircraft in flap configuration gives a good indication of where the aircraft is expected to experience a stall in flap configuration. Based on the theoretical AVL stall speed and practical flight tests for the aircraft in flap configuration, the aircraft's touchdown speed was selected to be 14 m/s . For the first landing iteration, this airspeed provided a safe region where the FCS can control the aircraft with relative ease (i.e. without using large actuator deflections), and added an extra measure of safety, that, in the event that the landing had needed to be aborted, the aircraft would still have had sufficient airspeed so that the safety pilot would have been able to retake control of the aircraft at a low altitude.

9.1.2 Touchdown

The accelerometer threshold that must be exceeded to indicate a landing impact was determined practically by investigating flight test data. Figure 9.1 shows two landing spikes in the Z_B -axis accelerometer measurement. This particular flight test was used to verify the avionics on board the aircraft. During the flight test the safety pilot was also instructed to perform one hard landing (left-most spike at 536.7 s) and to conclude the flight test with a soft landing (right-most spike at 575.8 s).

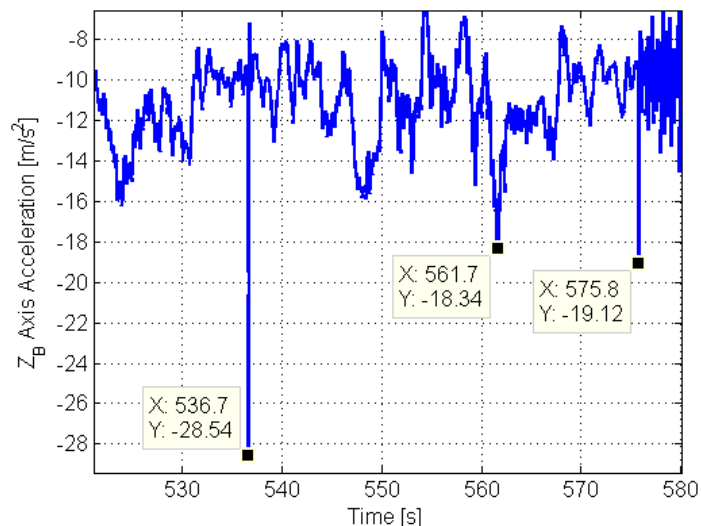


Figure 9.1 Landing Spikes in the Z_B -Axis Accelerometer

Note in the data segment illustrated in Figure 9.1, the middle spike at 561.7 s represents a steep climb rate. After the soft landing the accelerometer measurement becomes extremely noisy, which is a result of the ground roll. The hard-landing spike in Figure 9.1 is not the upper-most limit that the undercarriage of the aircraft can handle, but merely a representation of the maximum magnitude of the sink rate at touchdown that the safety pilot feels comfortable landing with.

For the purpose of this dissertation the Z_B axis accelerometer spike on impact indicates how hard the aircraft landed. The sink rate of the aircraft moments before touchdown gives an indication of how hard the aircraft is going to land. From a landing point of view it is important to control this parameter to ensure that no damage is caused to the undercarriage of the aircraft. The corresponding sink rates for the hard and soft landing performed by the safety pilot are stated below:

$$|\text{Sink rate}_{\text{Hard}}| \cong 1.4 \text{ m/s} \quad (9.4)$$

$$|\text{Sink rate}_{\text{Soft}}| \cong 0.5 \text{ m/s} \quad (9.5)$$

The hard-landing sink rate is used as an upper bound for the planned autonomous landing, since the undercarriage was able to absorb the shock with no visible damage. To quantify the sink rate an approximate conversion can be used to convert the sink rate into an equivalent drop height by making use of a constant acceleration equation of motion [10]

$$s = \frac{v^2}{2g} \quad (9.6)$$

where v is the magnitude of sink rate, s the equivalent drop height and g the constant gravitational acceleration. In the hard-landing case the sink rate is equivalent to dropping the aircraft from approximately 10 cm above the ground. Even though the undercarriage can handle this sink rate it is best to minimise the landing sink rate to prevent damage due to fatigue over time.

Based on the deductions made from Figure 9.1 and the knowledge that the FCS is expected to land with an airspeed of 14 m/s, with a landing glide slope between 3° and 6° which corresponds to medium and hard landing sink rates respectively, in the contexts of the two landings performed by the safety pilot. The acceleration threshold that needs to be exceeded to signal a landing was chosen to be -20 m/s^2 .

9.1.3 First and Second Glide Slope

The first glide slope's main aim in the landing state machine was to reduce altitude quickly, which is a testing environment constraint. Since the FCS is under evaluation it was necessary to keep the aircraft at a relatively high altitude in case of unexpected behaviour in the FCS. In other words: the higher the aircraft is from the ground the more time the safety pilot has to regain control of the aircraft in case of unexpected behaviour. To illustrate this point further: if the aircraft started its descent at 240 *m* from the aiming point with a landing glide slope of 3.3°, the aircraft would have been only 13.88 *m* above the ground. At this low altitude the aircraft is less visible from a distance of 240 *m* from the aiming point. Thus the combination of the first and second glide slopes allows the aircraft to fly the landing track at a higher altitude making it more visible to the safety pilot. The first glide slope was chosen as 6.6°; on this glide slope the aircraft has nearly double the starting altitude of the landing glide slope.

As mentioned earlier the longitudinal landing accuracy is expected to be a function of the estimated altitude error and the landing glide slope. For a first practical landing iteration the landing glide slope was chosen as 3.3° which translates to a 0.80 *m/s* sink rate at an airspeed of 14 *m/s*. The reasoning behind this design choice is as follows: by using a shallow glide slope the descent rate is not too fast to abort the landing if needed and the aircraft lands with a sink rate that would not cause damage to the aircraft's undercarriage even if the aircraft were to land harder than planned for. With enough confidence gained in the landing system, the plan was to increase the landing glide slope in subsequent landing tests to reduce the downrange error. Unfortunately, further landing iterations proved to be impossible because of unavoidable time constraints.

9.2 Autonomous Landing

A total of five autonomous landings were performed. The fourth and fifth autonomous landing tests were performed on the same day. The fourth and fifth autonomous landings are analysed next and are referred to as the first and second autonomous landings. In both cases the FCS landed the aircraft smoothly and safely. The recorded test data of the first autonomous landing is shown in Figure 9.2 .

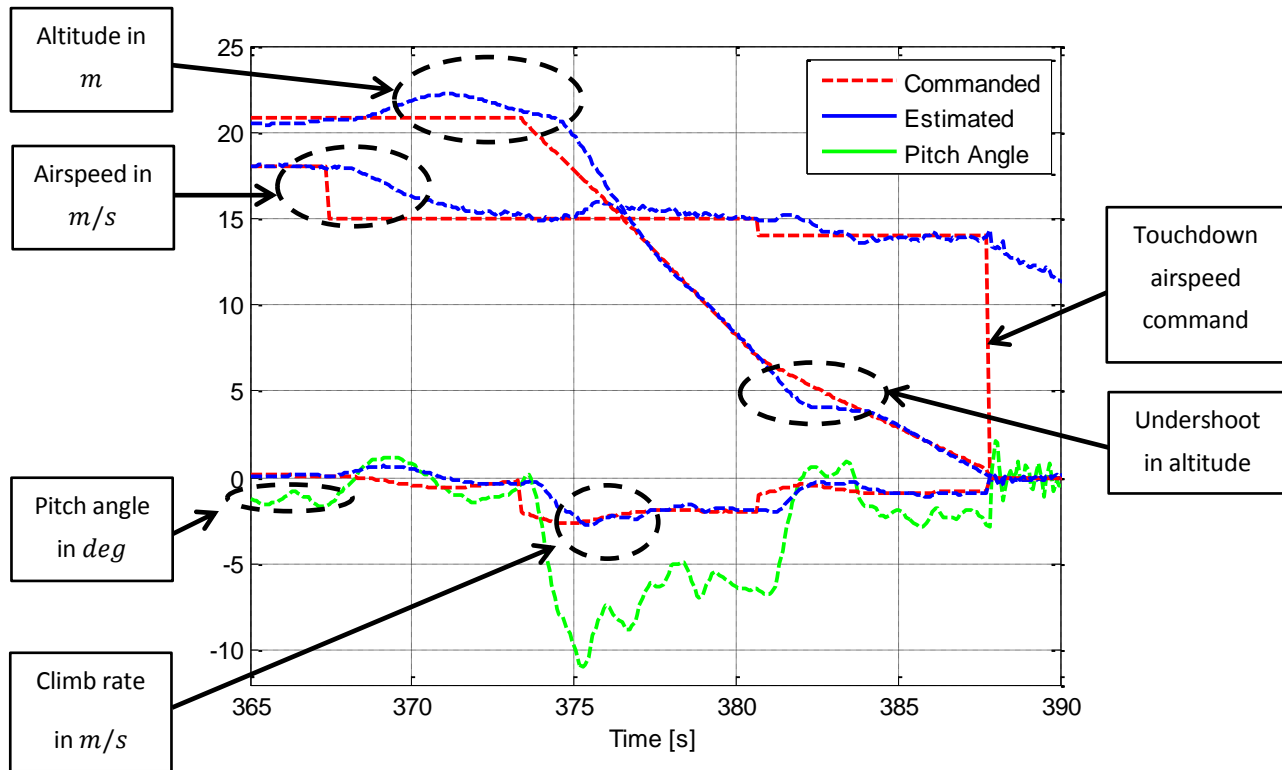


Figure 9.2 Measured Longitudinal Landing States During Actual Autonomous Landing

The data illustrated in Figure 9.2 is illustrated in the same format as the Ideal simulation in Section 8.2.1. A broad interpretation of the data presented in Figure 9.2 is given next, followed by an in-depth examination of these results.

9.2.1 Interpretation of Measured Landing Data

In Figure 9.2 the aircraft reached the approach point (Phase 1) at 367.5 s. The highlighted airspeed in Figure 9.2 shows the change in level-flight airspeed to glide airspeed. The highlighted rise in altitude, climb rate and pitch angle arises from the method in which the LQR controller reduces airspeed as discussed in Section 8.2.1. Note that the highlighted sections during the change in airspeed in Figure 9.2 are similar to the ideal simulation's highlighted sections in Figure 8.5. This observation indicates that the simulation environment describes the aircraft's real-world behaviour relatively accurately. The highlighted pitch angle represents the pitch angle at which the aircraft is flying straight and level. In Figure 9.2 the highlighted pitch angle is near zero since at take-off there was a bias of approximately 1.2° . Even with the addition of the bias to the recorded pitch angle, it is unlikely that the aircraft would cruise at a 0° pitch angle, which calls into question the accuracy of

the estimated pitch angle. In Phase 2, at 374.1 s, the aircraft captures the first glide slope in approximately three seconds. In Phase 3, at 380.7 s the aircraft captures the second glide slope with a slightly higher undershoot in altitude than in Figure 8.5. The aircraft touched down at 387.7 s as indicated by the zero commanded airspeed in Figure 9.2. The acceleration spike upon Touchdown is shown in Figure 9.3.

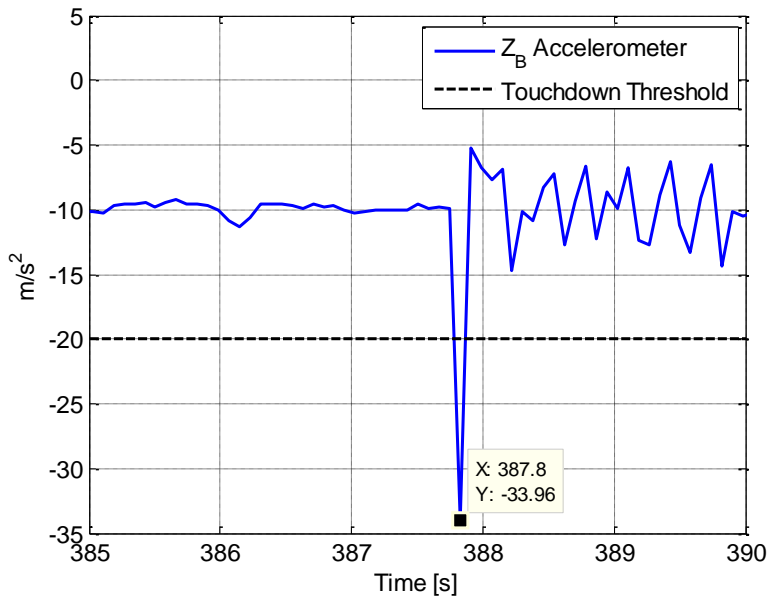


Figure 9.3 Touchdown Spike Measured by the Z_B -Axis Accelerometer

9.2.2 Airspeed and Climb Rate

Figure 9.4 illustrates the airspeed (pressure sensor), climb rate and ground speed from the DGPS during the landing approach. From Figure 9.4 it is evident that during the final landing stage there was a tail wind of approximately 1 m/s. Note that the highlighted ground speed is investigated later. The main effect of a tailwind during the landing approach is that it increases the descent angle, as was found in Section 8.2.2. The increase in descent angle leads to a more negative climb rate which causes premature touchdown at a smaller pitch angle. Touchdown can be seen in Figure 9.4 (a) when the airspeed command is reduced to 0 m/s. In Figure 9.4 (b) touchdown is indicated by the positive climb-rate landing spike followed by noise on the estimated climb-rate signal. The noise is a result of the aircraft running over the runway which was covered with rubble.

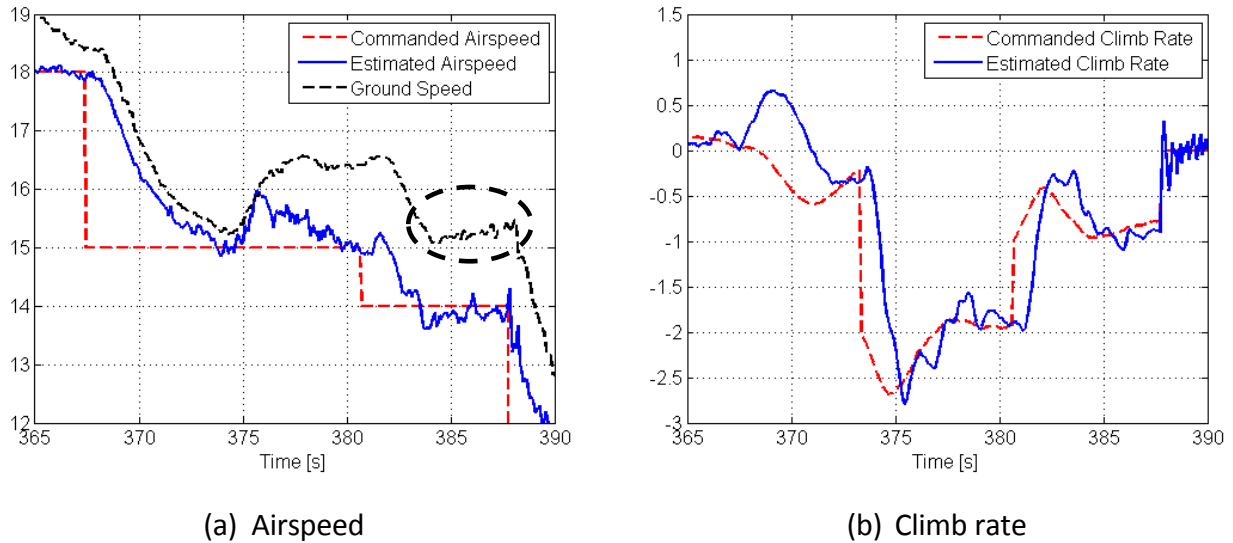


Figure 9.4 Airspeed and Climb Rate during the Landing Approach

9.2.3 Landing Accuracy

The touchdown accuracy is investigated by enlarging the section in Figure 9.2 just after the highlighted undershoot in altitude when the aircraft is on the second glide slope leading up to touchdown. Figure 9.5 illustrates the commanded estimated and DGPS altitude as well as a flag that indicates touchdown. The touchdown flag changes its state to true (0 to -0.5) when the touchdown acceleration spike is detected and the landing conditions are satisfied, as explained in Section 7.2.

In Figure 9.5, it is evident that the estimated altitude and the DGPS altitude diverge from the commanded altitude as the aircraft's altitude decreases, which in turn decreases the landing accuracy. The touchdown point is obtained by evaluating the estimated North and East position when the touchdown flag changes its state to true. In Figure 9.5, the aircraft landed approximately 7.2 m (downrange error) before the aiming point in the north direction and 1.2 m in the east direction. The large error in the longitudinal touchdown point is caused by the visible altitude error of approximately 0.35 m (on impact when the commanded altitude becomes zero) which shifted the touchdown point. On a closer evaluation of Figure 9.5 the estimated altitude slope is 0.7° higher than the reference slope of 3.3° from roughly 2.5 m in altitude.

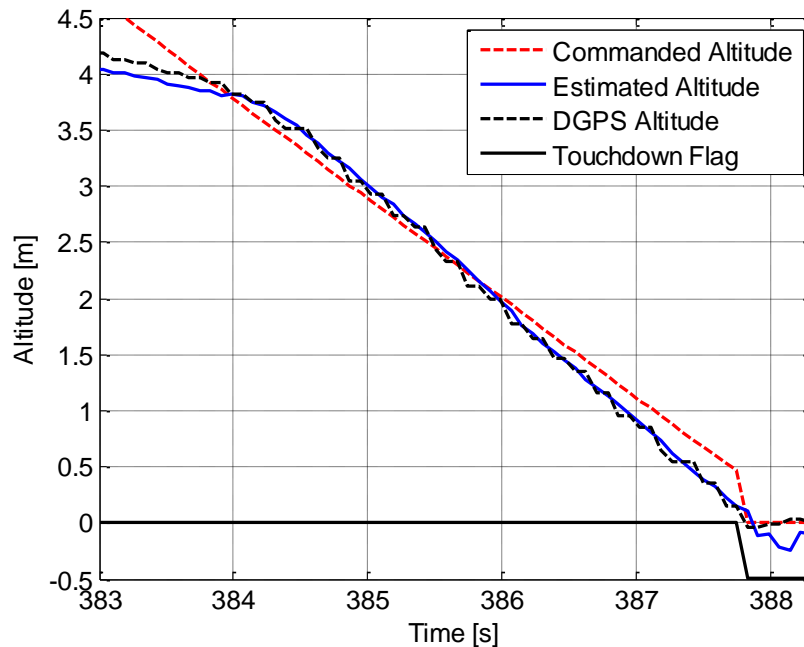


Figure 9.5 Practical Landing Altitude States on the Second Glide Slope

To evaluate this last observation the estimated, DGPS and commanded climb rates are plotted over time with the differentiated estimated altitude in Figure 9.6. The differentiated estimated altitude is obtained by using the gradient function in Matlab. Referring to Figure 9.6, the following observations can be made:

- The differentiated estimated altitude rate is more negative than the estimated climb rate and follows the DGPS climb rate envelope, which suggests that there might be a bias error on the estimated climb rate.
- The estimated climb rate is 0.1 m/s more negative than the -0.77 m/s commanded climb rate on touchdown. The differentiated estimated altitude is on average 0.11 m/s more negative than the estimated climb rate from 387 s to just before the dip in differentiated estimated altitude near 388 s. A further observation to note is that the estimated climb rate does not follow the commanded climb rate.
- On impact, there is a delay of 0.31 s between the estimated climb rate and the DGPS climb rate and a delay of 0.12 s between the differentiated estimated altitude and the DGPS climb rate.

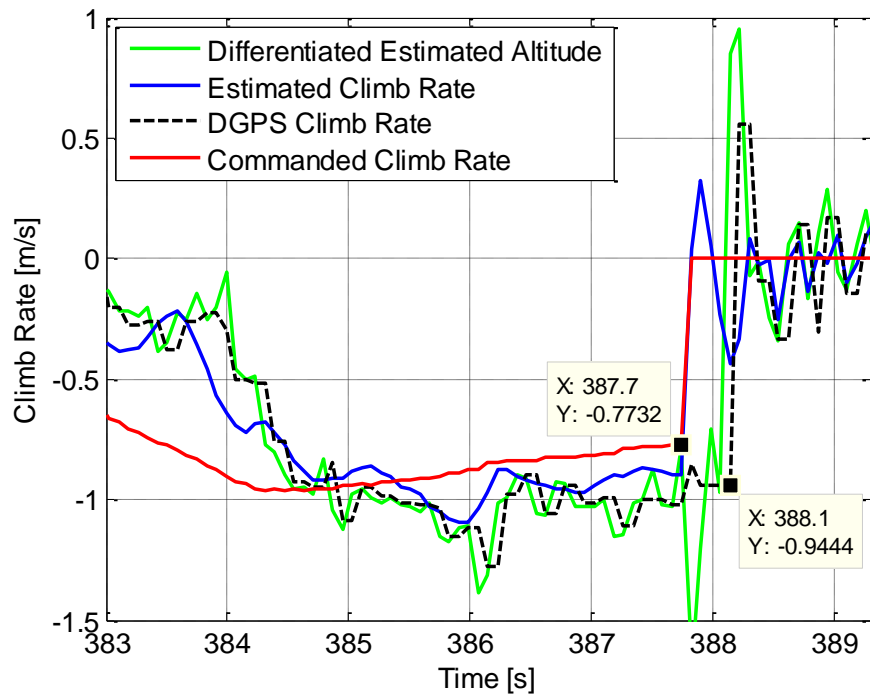


Figure 9.6 Practical Landing Climb Rate States Seconds before Touchdown

On the practical landing test day the aircraft seemed to land relatively close to the point of initialisation on the runway. This visual observation does not correlate very well with the estimated touchdown point. By re-evaluating the touchdown point relative to the measured DGPS North and East positions when the DGPS detected the impact, the aircraft landed 2.6 m before the aiming point and 1.1 m to the East, in compact form the aircraft touchdown point relative to the aiming point is $(-2.6, 1.1)\text{ m}$. In the second autonomous landing test the aircraft's touchdown point is $(-0.75, 0.8)$. Even though the longitudinal landing accuracy increased significantly relative to when the DGPS detected the landing impact, the FCS landing performance must be evaluated based on the estimated North and East positions when the accelerometer spike is detected since the FCS control actions are based on the estimated states and not the measured DGPS states. Thus the landing performance of the FCS falls into the inaccurate landing category set in this dissertation.

Based on the observations made in Figure 9.6, the objective now becomes to determine the cause of the inaccurate landing. To this end, the aircraft's states during a virtual deck landing are plotted in Figure 9.7 and analysed.

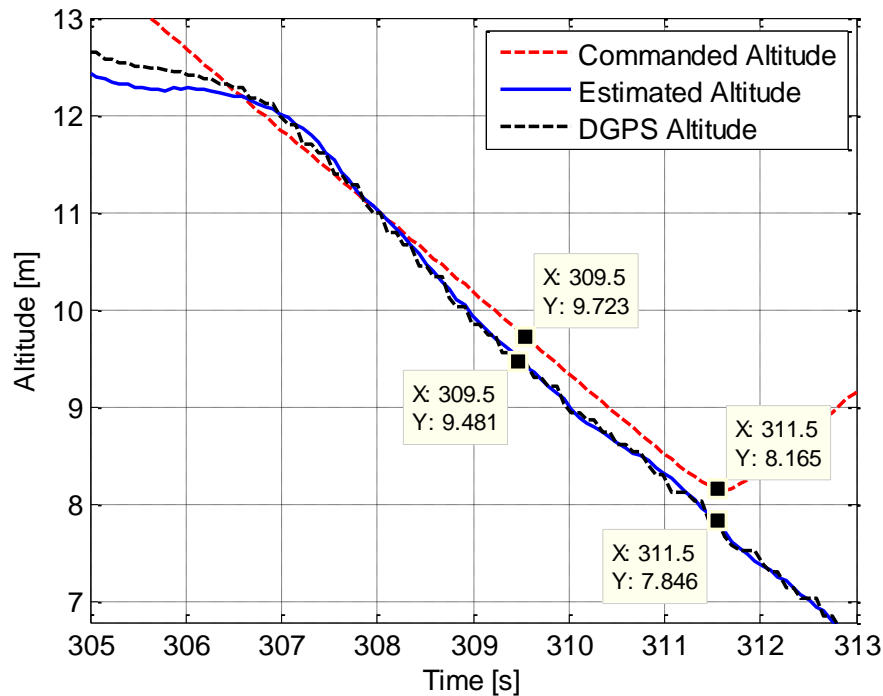


Figure 9.7 Practical Virtual Deck Landing Test

The virtual deck landing test was performed in the same flight test just before the actual landing in Figure 9.5. The wind conditions for the actual landing and virtual deck landing are shown in Figure 9.4 and Figure 9.8 respectively. By comparing the virtual deck landing's altitude profile with the actual landing altitude profile, it is evident that the two altitude profiles are not similar, nor are the wind conditions. In Figure 9.7 it is clear that the FCS tracks the reference altitude with a constant altitude error. In the case of the virtual deck landing, the resulting error in altitude can be explained by a bias error in estimated climb rate, since the measured airspeed is near the commanded airspeed as shown in Figure 9.7 and the estimated climb rate is near the commanded climb rate as shown in Figure 9.8. In the case of the first practical landing, the altitude error can be explained by a combination of the bias error in the estimated climb rate, the wind condition and the ground effect. These effects on the landing accuracy are investigated in the next sections, together with the origin of the climb-rate bias and the effect of a delayed DGPS climb rate measurement.

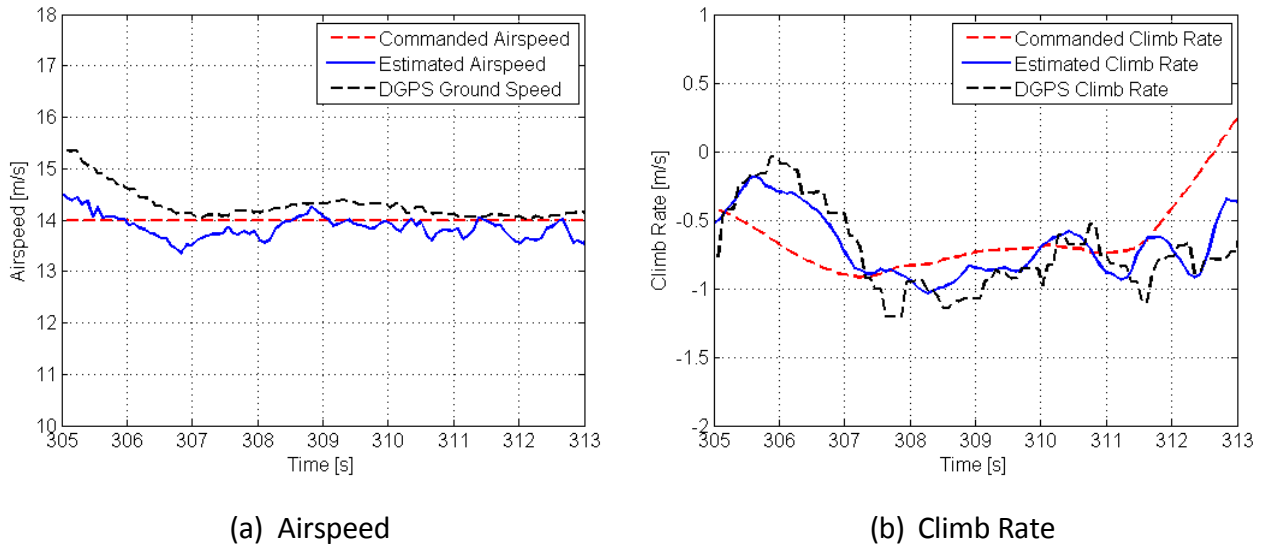


Figure 9.8 Virtual Deck Landing Airspeed and Climb-Rate States on the Second Glide Slope

9.2.3.1 Climb-Rate Bias

To determine the effect of a constant climb rate on the FCS, the aircraft's altitude profile on the second glide slope is investigated in a non-linear landing simulation in Figure 9.9, where a climb-rate bias of 0.1 m/s is added to the climb-rate signal. In the simulated landing it is evident that the added climb-rate bias resulted in the FCS tracking the reference altitude with a constant error in altitude after the aircraft settled on a glide slope. This behaviour is caused by the FCS architecture, since the climb-rate controller has an error integrator state that forces the estimated climb rate plus the climb-rate bias to the reference climb rate in steady state. Without the altitude controller for a zero climb-rate command for straight and level flight, the aircraft would have continuously climbed or descended based on the sign of the climb-rate bias. Thus it can be said that the error in altitude is a result of the altitude controller which attempts to reject the disturbance introduced by the climb-rate bias, but only manages to do so with a constant steady state error in altitude tracking.

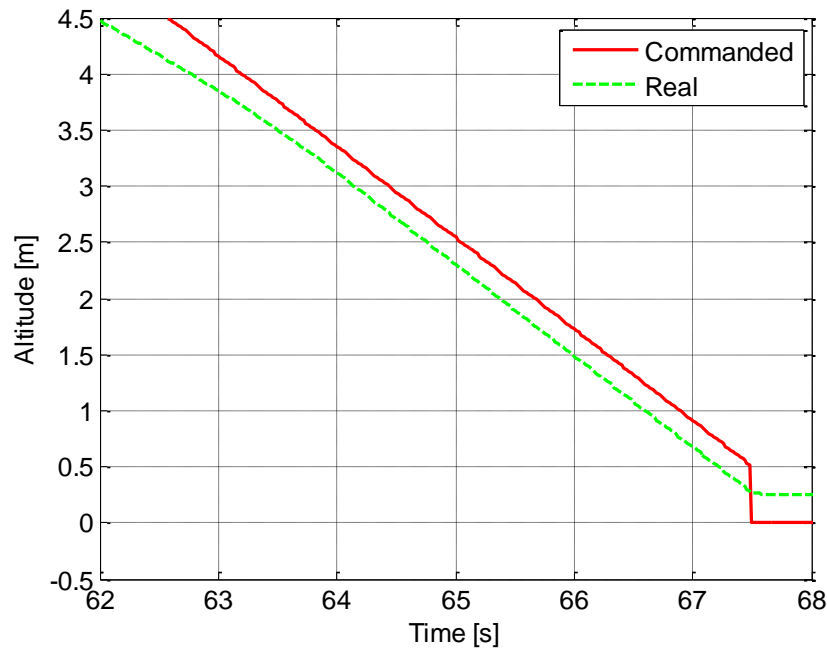


Figure 9.9 Simulated Landing with a Climb-Rate Bias

In the landing state machine the commanded climb rate is the sum of the feed-forward climb rate and the error in altitude multiplied by the altitude controller feedback gain (0.42). Figure 9.10 is zoomed in on Figure 9.9 and illustrates the commanded altitude and climb rate, actual altitude, estimated climb rate with the added bias error and the actual climb rate. During the aircraft's descent on the second glide slope, the feed-forward climb rate is -0.8 m/s (not shown in Figure 9.10). The commanded climb rate is equal to -0.7 m/s which is the sum of the reference feed-forward climb rate and the climb-rate command generated by the nearly constant error in altitude of 0.233 m from 63.5 s to touchdown. The constant altitude tracking error of 0.233 m results in a relatively large downrange error of -4 m .

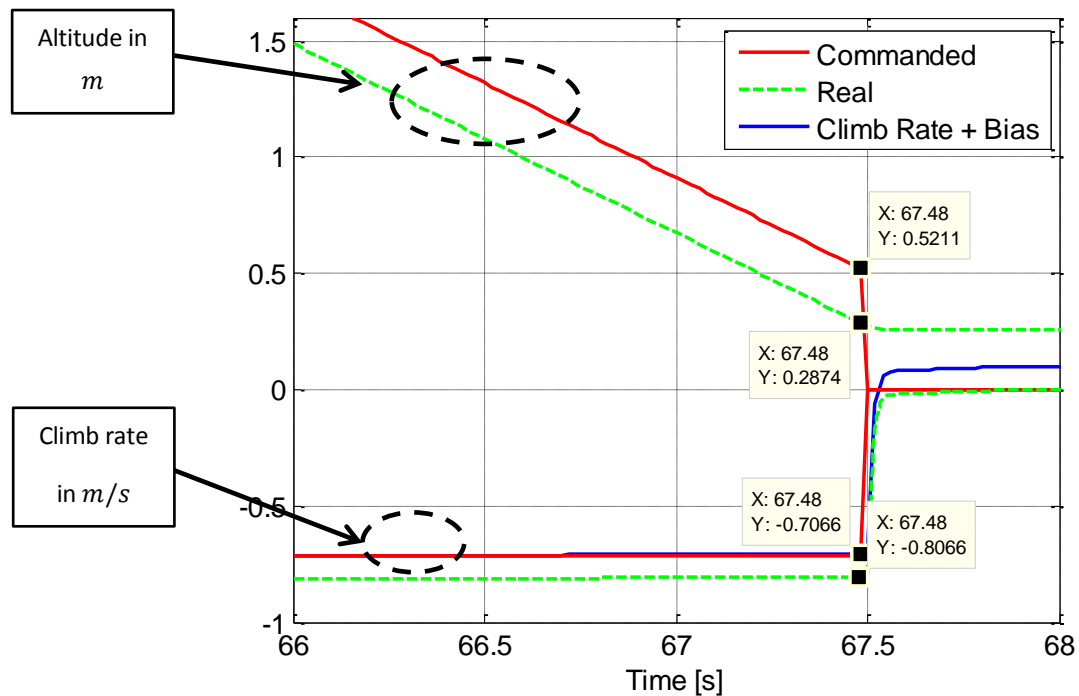


Figure 9.10 Simulated Landing Seconds before Touchdown

With the effect of the climb-rate bias explained in the FCS, the question remains as to how accurately the FCS is expected to land the aircraft, when the climb-rate bias is removed. An indication of the expected ability of the FCS to track the commanded altitude with accurate states can be obtained by re-evaluating the virtual deck landing. Referring back to Figure 9.7, it is evident that the FCS system performs very well in regulating the altitude of the aircraft on the second glide slope, with a mean error of -0.27 m and a standard deviation of 0.048 m from 309.5 s until 311.3 s (or equivalently from 1.5 m in reference altitude above the virtual deck touchdown point). The maximum and minimum tracking error during this time period is -0.21 m and -0.36 m respectively. If the bias on the climb rate (mean error) is removed it can be argued that the FCS is expected to have a maximum altitude tracking error of $\pm 0.14\text{ m}$ which would lead to a virtual deck touchdown longitudinal error of $\pm 2.5\text{ m}$. The expected landing error is calculated using the maximum tracking error as an offset in altitude which shifts the landing point as depicted in Figure 8.6. The resulting longitudinal landing error can also be easily decreased by increasing the landing glide slope; for instance if the glide slope were doubled, the landing error would be theoretically halved.

9.2.3.2 Wind Condition

With the effect of the climb-rate bias on the landing accuracy explained, the focus shifts to analysing how the wind affects the landing accuracy in the first and second landing. To this end the altitude profile, airspeed and climb-rate profile of the second autonomous landing is plotted in Figure 9.11 and Figure 9.12. It is evident that the altitude profile of virtual deck landing and that of the second autonomous landing compare well, even though there is a tailwind in the second autonomous landing. Furthermore, the measured airspeed and estimated climb rate in the second autonomous landing has not quite settled on the commanded values as in the virtual deck landing. In a tailwind gust simulation (described in Chapter 8), it was found that the LQR controller corrects the airspeed by pitching the aircraft's nose down, which explains why the measured airspeed and estimated climb are below the commanded values, since the LQR controller is still in the process of "trimming" the effect of the constant tailwind out. The effect of wind gust behaviour is more evident in the first autonomous landing; referring back to Figure 9.4, it can be seen that ground speed increases (highlighted section) as the aircraft nears the ground, which leads to a more negative climb rate as the LQR controller compensates for the loss in airspeed, which in turn leads to a diverging altitude profile and an increasing downrange error.

A similar landing performance analysis to that described in the previous section was performed on the second practical landing data, to gain an indication of the landing ability of the FCS amidst the disturbances caused by the climb-rate bias, wind effect and ground effect. The FCS follows the commanded altitude with a mean error of -0.32 m and a standard deviation of 0.036 m from approximately 1.5 m in reference altitude until touchdown. The maximum and minimum tracking error during this time period is -0.27 m and -0.38 m respectively. The mean tracking error for the second practical landing error is slightly larger than the virtual deck landing mean tracking error which is to be expected since the climb-rate profiles differ, while the standard deviation in altitude is similar. Thus it can be concluded, based on the captured data for the second autonomous landing and the virtual deck landing, that if the climb-rate bias is removed the landing accuracy in ground effect with a constant tailwind will be slightly less accurate than in the case for the virtual deck landing based on the small change in mean and standard deviation values for the two landings.

However, Even if the estimator is updated and the estimated states are accurate, the "nose down" effect that a tailwind gust has on the control actions of the LQR controller during landing is dangerous and leads to inaccurate landings. To remedy this in part it could also be argued that the aircraft is not supposed to land in a tailwind in the first place, which would ensure a more "nose-up"

landing approach for a headwinds and headwind gusts, as was found in simulation in Chapter 8. However due to the nature of the wind shear (where the aircraft could be flying with a headwind and seconds later with a tailwind), wind gusts and the ideology of a robust landing controller, the “nose-down” effect is undesirable.

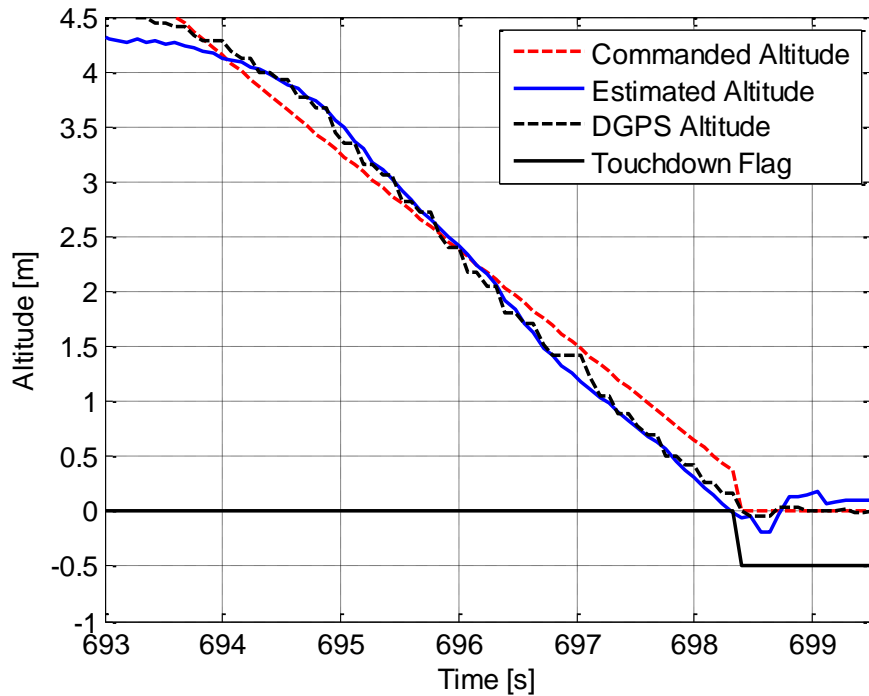


Figure 9.11 Measured Longitudinal Landing States during Second Autonomous Landing

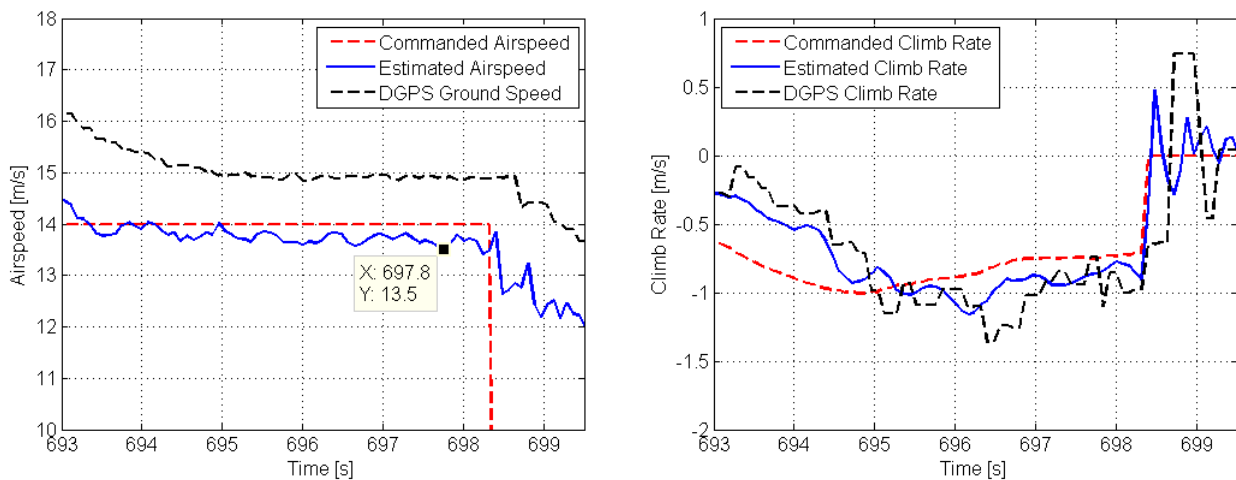


Figure 9.12 Second Autonomous Landing Airspeed and Climb-Rate States on the Second Glide Slope

9.2.3.3 Ground effect

As a rule of thumb in aerodynamics, the ground effect starts from a wing span above the ground (2 m wing span in this case). As the aircraft nears the ground, the lift on the main wings increases and the aircraft is expected to overshoot the aiming point (increase in climb rate) and to land with a positive downrange error. Based on the two autonomous landing altitude and climb rate profiles this effect is difficult to see, which suggests that the ground effect had a minimal effect on the downrange error.

9.2.3.4 Origin of the Climb-Rate Bias

A bias on the estimated aircraft states can be a combination of a bias on the accelerometer and the delayed DGPS position and velocity states. At this stage it is unclear as to what the delay is on the measured positions that the DGPS provides; however the delay on the measured DGPS climb rate can be clearly seen in Figure 9.6. Thus the focus of this section is on the delayed DGPS climb measurement and biased accelerometers.

A bias in the estimated climb-rate state is established, when the delayed climb-rate measurement of the DGPS corrects the biased propagated states from the accelerometer via the Kalman filter gain. Additionally, if the aircraft is in constant motion the delayed climb rate is equal to the propagated climb rate if there is no bias on the accelerometers. However, as the aircraft experiences transient motion, the delayed climb rate measurement is not equal to the propagated climb rate.

Furthermore, the delay on the measured DGPS climb rate will also affect the estimated attitude of the aircraft, since the DGPS climb rate is used to determine the inertial acceleration vector which is used in triad algorithm to update the propagated attitude estimate. The estimated attitude is also used in the DCM to transform the measured acceleration of the accelerometers in the aircraft's body axis to the inertial axis. The transformed body axis acceleration is used to propagate the aircraft's position and velocity states during the time when no measurement update is available.

9.3 Summary

This chapter started off by identifying the aircraft's stall speed in clean and flap configuration, the touchdown acceleration that needs to be exceeded to signal a landing to the FCS, and the use of having two glide slopes. A total of five practical autonomous landings were performed. The data

sets of the last two autonomous landings were analysed, and in each of these landings the practical landing performance did not correlate with simulated landing performance. Explanations for each of the two landings were given where the practical data deviated from the simulated landing results (in Chapter 8) concerning the climb-rate bias, wind disturbance and ground effect.

Chapter 10

Conclusion and Recommendations

10.1 Summary

This thesis has presented the design and practical demonstration of a flight control system that is capable of autonomously landing a fixed-wing UAV on a stationary platform, aided by a high-precision GPS. The project forms part of on-going research in ATOL at Stellenbosch University with the end goal of landing a fixed-wing UAV on a moving platform, for example on a ship's deck.

The selected airframe was equipped with the standard ESL avionics stack. The airframe's aerodynamic coefficients were determined via AVL and the equipped aircraft's mass moment of inertia was obtained by the double pendulum method. The stall speed of the airframe was also determined in AVL and practically flight tested. With a flight-ready aircraft, the scene was set for controller design and testing. The inner-loop and outer-loop controllers were designed based on the acceleration-based manoeuvre autopilot architecture [1]. In preparation for a practical flight test, the designed flight controllers were tested in SIL and HIL simulations to verify the performance of the FCS and to minimise risk. With an equipped airframe and practically flight-tested controllers, the scene was also set to test the developed landing state machine via virtual deck landings tests. Then with enough confidence gained in the FCS and to enable the FCS to perform practical landings, Novatel's high-precision GPS was integrated into the aircraft and the FCS OBC code. Considerable time went into testing the FCS with the new DGPS to ensure the desired operation. Landing simulations were repeated in SIL and HIL simulation to test the FCS robustness and execution of the landing state machine to minimise risk before practical landing tests.

The autopilot's landing accuracy was considered precise if the touchdown point was within a circle centred on the aiming point with the diameter of the aircraft's fuselage length (1.5 m). The landing accuracy was considered accurate if the aircraft landed within a circle with a diameter of twice the aircraft's fuselage length. Out of 100 non-linear autonomous simulated landings, the FCS landed the aircraft 98 times in a circle with a diameter of 1.5 m and twice within a circle with a diameter of 3 m. In the two analysed practical autonomous landing tests, the FCS landed the aircraft safely and smoothly inside a circle with a radius of 7.5 m based on the estimator's position. The large resulting

landing error is due to the large longitudinal error, which resulted primarily from a climb-rate bias and to a lesser extent from the nose-down effect that a tailwind has on the longitudinal FCS. An analysis that removed the climb-rate bias effect showed that the FCS is expected to land within a circle with a radius of 2.5 *m* during a practical landing; the expected landing error can be halved by doubling the current glide slope of 3.3°. However, the nose-down effect that a large tailwind gust has on the LQR controller is dangerous in the last stages of landing; hence a different longitudinal controller strategy is suggested in future autonomous landing projects.

10.2 Conclusion

By analysing the data from the autonomous landings the following conclusions can be drawn:

- In the first autonomous landing, the FCS landed the aircraft inaccurately relative to the estimated landing point as a result of the climb-rate bias and the nose-down effect caused by an increase in tailwind speed. In the second autonomous landing, the FCS landed the aircraft less inaccurately than in the first landing as a result of a more constant tailwind.
- The nose-down effect that was caused by a tailwind gust is an undesired property of the longitudinal LQR controller. The climb-rate bias caused the altitude controller to follow the reference altitude with a constant error in altitude.
- An indication of the ability of the FCS to land the aircraft with the climb-rate bias removed was obtained by investigating a virtual deck landing and the second autonomous landing. In the case of the virtual deck landing the effect of the constant bias in climb-rate bias was removed by shifting the estimated altitude upon the commanded altitude. This analysis showed that the FCS is expected to have a longitudinal virtual deck touchdown error of ± 2.5 *m*. In case of the second autonomous landing the mean altitude error was found to be slightly higher than virtual deck landing mean altitude error as a result of a tailwind. The standard deviation altitude error for both of the landings was found to be similar, which indicates that the FCS is expected to land with a similar longitudinal error to that of the virtual deck landing. It was also said that if the glide slope is doubled the landing error is expected to halve.
- The ground effect had a minimal effect on the landing ability of the FCS, since a similar landing performance was obtained in the second autonomous landing to that of the virtual deck landing (out of ground effect).

- The climb-rate bias is a combination of the delayed climb-rate measurement of the DGPS and bias a on the Z_B -axis accelerometer. The delayed DGPS climb-rate measurement is also used in the estimator to correct the propagated attitude, which affects the estimated attitude. The DCM is in turn used to transform the measured acceleration in the aircraft's body axis to the inertial frame, which in turn affects the propagated position and velocity states when no measurement update is available
- A decrease in accuracy in the estimated position states and a bias on the aircraft's attitude affects the performance of the guidance controller, since the estimated position of the aircraft is used to calculate a roll-angle command for the roll-angle controller. In Section 5.2.4 the maximum lateral landing error bounds of the FCS were found to be $\pm 0.85 m$ when the aircraft is passing over the runway during a virtual deck landing. The lateral landing error in the practical landings is of a similar order to that found in virtual deck landing.

10.3 Recommendations

The following list is a set of recommendations on how the autonomous landing system as whole can be improved and extended.

Estimator

- An estimation strategy such as the measurement extrapolation Kalman filter (MEKF) could be employed to provide accurate state estimates with known delays in sensor measurement updates. The MEKF filter essentially computes a correction term that is added to the estimation process when the delayed measurement arrives [33].
- During the integration of the DGPS rover module into the OBC, the estimator gains were not recalculated, and those of the standard GPS were reused. This has the effect that the estimated states had a smaller mean error since the DGPS measurements had a smaller mean error than the standard GPS. If the measurement covariance matrices had also been updated the estimated states would have had a smaller variance error. Due to time limitations the estimator was not updated and flight tested.

Hardware

- There are various methods to determine the time delay in the measured DGPS position and velocity states. With the DGPS time delay known, the estimated state accuracy can be increased.
- The current speed controller does not allow the thrust vector of the motor to reverse and is also fairly old and relatively heavy compared to new speed controller designs. By replacing the current speed controller the aircraft would be made lighter and the ability to reverse thrust would be gained.
- The current LiPo battery pack, speed controller, engine and propeller limit the aircraft's flight envelope and flight time to five minutes. The current aircraft configuration is heavy and flies at trim speed at approximately 75% of the current maximum thrust. In stronger winds more thrust is required. If longer flight times are required a better LiPo battery pack can be installed. By changing to a better propeller and engine combination more thrust can be achieved to fly in stronger winds. The changes mentioned in this paragraph can be easily implemented since the more serious RC hobby enthusiast can tell from experience which battery pack, speed controller and engine-propeller combination works best.
- The current silicon dampers that hold the avionics box in place in the aircraft are made in the ESL. These dampers are not rigid enough to keep the avionic box in the calibrated position inside the aircraft. Thus small biases exist on the acceleration and rate gyro measurements. A more rigid damper or a different design to keep the avionics box in the calibrated position inside the aircraft will remove small biases from the IMU's measurements.
- The addition of hand-fastened screws significantly decreased the setup time of the aircraft before a flight test. The use of as few tools as possible on a flight day decreases setting up time and this is recommended for all projects.
- The addition of an AoA sensor could lead to more accurate state estimation and opens new doors to control the aircraft on the final stages of landing.

Control System

- The LQR controller is well-suited for flight control since it uses gravity to reduce or increase the aircraft's airspeed/climb rate. However, a situation may present itself where a wind gust reduces the airspeed of the aircraft during the final stages of landing. In this situation the LQR controller will pitch the nose of the aircraft down to regain airspeed which could potentially lead to a crash. Thus in further autonomous landing projects it is advised to use two SISO systems to regulate the airspeed and climb-rate via throttle and elevator respectively to overcome this limitation.
- The current landing state machine detects the transition from aircraft to ground craft. Thus the landing state machine can be extended to include the ground roll. Take-off, ground controllers and advanced guidance algorithms can be added from [12] to create a system that is capable of autonomous navigation, take-off and landing. In the landing tests the aircraft had minimal bounce and the wheels of the aircraft remained in contact with the ground, thus a ground controller will be relatively easy to add to the current FCS.
- The current control system does not have the ability to de-crab the aircraft moments before touchdown in crosswind conditions. A de-crab controller can be designed to align the aircraft's body axis with the runway at the last moment before touchdown.
- The current control system has limited safety features and relies on the safety pilot to abort the landing if the aircraft is coming in for landing too quickly or with a negative pitch angle for landing. Additional safety checks should be built into the control system to abort the landing automatically and to go around and try again.
- If an AoA sensor is installed, a control system can possibly be developed that controls the AoA based on the downrange of the aircraft from the intended touchdown point. With this type of control system the aircraft could follow a virtual trajectory with different AoA's instead of different waypoints with specific climb rates. With this strategy the aircraft would experience a complete controlled stall just before touchdown.

Landing

- The current glide slope that the FCS follows to land the aircraft can be optimised to provide the best measure of safety and accuracy during landing. By analysing the amount of impact force the landing gear can dissipate, as well as by determining the estimated altitude error after the estimator is updated.

- In simulation it was assumed that the ground effect would have minimal impact on the landing accuracy, while in practice it was found that the ground effect was not evident in analysed landing data. By investigating the ground effect in future projects, the landing performance could be increased.
- The ground roll can be decreased by deflecting the ailerons upwards and leaving the flaps downwards to create additional drag. This idea was tested in simulation with good results but not in the real world. The ground roll can also be reduced by reversing the thrust once the aircraft is on the ground.

In closing the four most important recommendations are: the LQR controller should be replaced by two SISO controllers to avoid a nose-down situation, the accelerometers must be recalibrated to remove biases on them, the DGPS delay must be used in the estimation strategy to increase the accuracy of the estimated states and finally the glide slope must be optimised based on the estimated altitude error and the landing impact force that the landing gear can dissipate.

Appendices

Appendix A

Aircraft Specifications and Modelling

This appendix describes the aircraft data used in the non-linear simulations. The aircraft used in this project was a modified Phoenix Trainer 60, equipped with a Hyperion Zs-4025-10 brushless DC motor controlled by the Hyperion ATLAS series electronic speed controller (ESC). The appendix summarises the aerodynamic and physical characteristics of the aircraft.

A.1 Physical Specifications

A.1.1 Aircraft's Weight Budget

Table A.1: Aircraft Weight Budget

Aircraft with wings (pressure board and counterweights on wings included), servo board, receiver, speed controller and motor	4.382 <i>kg</i>
DGPS <ul style="list-style-type: none"> • Rover module in aluminium safety box • DGPS antenna 	0.48 <i>kg</i> <ul style="list-style-type: none"> • 0.28 <i>kg</i> • 0.2 <i>kg</i>
Avionics box, OBC , Ublox GPS, Maxstream and IMU	0.5361 <i>kg</i>
Batteries <ul style="list-style-type: none"> • Backup (NiCd) • Avionics (3 cell LiPo) • Main engine (5 cell LiPo) 	0.896 <i>kg</i> <ul style="list-style-type: none"> • 0.1 <i>kg</i> • 0.1435 <i>kg</i> • 0.6525 <i>kg</i>
Total mass	6.2945 <i>kg</i>

A.1.2 Moment of Inertia

The double pendulum method was used to determine the moment of Inertia. This method was first used in the ESL in [9] and then later in [29] to determine the moment of inertia for two different types of RC aircraft. In the double pendulum method the aircraft is suspended by two thin strings that run parallel with the axis of interest. Figure A.1 demonstrates this setup.



Figure A.1 Moment of Inertia Measurement Setup

A small moment is induced on the axis of interest and then, by observing the period of oscillation, the moment of inertia can be calculated. Refer to [9] for more information on this method. The calculated moment of inertia for the modified Phoenix Trainer 60 is given below,

Table A.2 Measured Moment of Inertia

Inertia	Value	Unit
I_{xx}	0.7212	kg. m ²
I_{yy}	0.5139	kg. m ²
I_{zz}	0.9239	kg. m ²

A.1.3 Engine Thrust

A static thrust test was used to determine the maximum aircraft engine thrust and time constant:

$$T_{Max} = 32 \text{ N} \quad (\text{A.1})$$

$$\tau < 0.2 \quad (\text{A.2})$$

A.2 Modelling Constants

A.2.1 Air Density

The air density is used as constant in the aerodynamic model. This assumption is based on the small altitude ranges. The air density at sea level is given by

$$\rho = 1.225 \text{ kg/m}^3 \quad (\text{A.3})$$

A.2.2 Gravitational Acceleration

In the modelling of the aircraft an equipotential gravity vector is assumed, thus earth's gravitational constant at sea level is used:

$$g = 9.81 \text{ m/s}^2 \quad (\text{A.4})$$

A.3 Aerodynamic Model

A.3.1 Airfoil Specifications

The airfoil properties of the modified Phoenix Trainer 60 are given below, where ND stands for non-dimensional. The modifications done to the aircraft only affect the fuselage of the aircraft.

Table A.3 Airfoil Properties

Parameter	Symbol	Value	Unit
Root chord	c_r	0.3730	m^2
Tip chord	c_t	0.3330	m^2
Span	b	1.9120	m^2

Area	S	0.69190	m^2
Mean aerodynamic chord	\bar{c}	0.36278	m^2
Aspect ratio	A	5.28	ND
Oswald efficiency factor	e	0.85	ND

A.3.2 Aircraft Trim Airspeed

The trim airspeed of the aircraft was chosen to be in the middle of the flight envelope:

$$V_{W_0} = 15 \text{ m/s} \quad (\text{A.5})$$

A.3.3 Non-Dimensional Stability and Control Derivatives

To calculate the derivatives of the modified Phoenix Trainer 60, a free computational fluid dynamics program, based on vortex lattice methods, was used. Athena Vortex Lattice (AVL) was developed by MIT's Aeronautics and Astronautics department. The aircraft geometry is constructed in AVL by measuring the dimensions of the aircraft and entering them into a text file. AVL provides a user guide in a text document on how to use the program and [29] presents a useful summarised version of AVL's user guide.

The geometry of the airframe is shown in Figure A.2. From the geometry plot of the aircraft, various actuator surfaces can be seen in yellow with an approximated cylinder-shaped fuselage in blue. The stability and control derivatives calculated by AVL are presented in Tables A.4 and A.5 respectively.

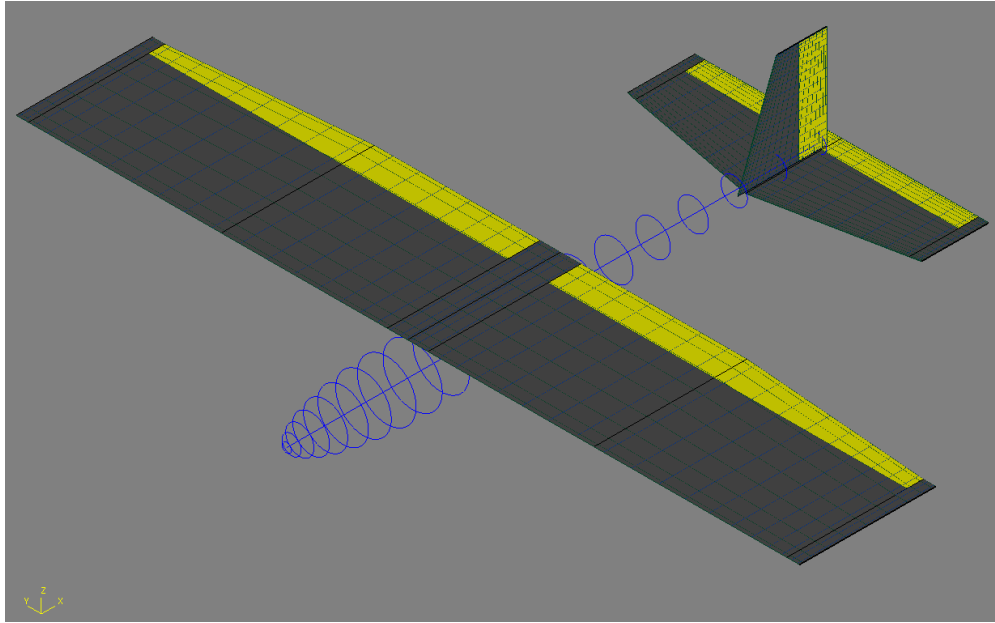


Figure A.2 AVL Geometry Plot of the Aircraft

Table A.4 Stability Derivatives for the Aircraft in Clean Configuration

Due to	Angle of Attack (α)	Side-slip Angle (β)		
Z force	$C_{L\alpha} = 4.712760$	$C_{L\beta} = 0.000000$		
Y force	$C_{Y\alpha} = 0.000000$	$C_{Y\beta} = -0.403886$		
l	$C_{l\alpha} = 0.000000$	$C_{l\beta} = -0.001929$		
m	$C_{m\alpha} = -0.540949$	$C_{m\beta} = 0.000000$		
n	$C_{n\alpha} = 0.000000$	$C_{n\beta} = 0.051502$		
Due to:	Roll-rate (p)	Pitch Rate (q)	Yaw Rate (r)	
Z force	$C_{Lp} = 0.000000$	$C_{Lq} = 7.878252$	$C_{Lr} = 0.000000$	
Y force	$C_{Yp} = -0.001294$	$C_{Yq} = 0.000000$	$C_{Yr} = 0.116584$	
l	$C_{lp} = -0.418910$	$C_{lq} = 0.000000$	$C_{lr} = 0.001828$	
m	$C_{mp} = 0.000000$	$C_{mq} = -7.612766$	$C_{mr} = 0.000000$	
n	$C_{np} = 0.000443$	$C_{nq} = 0.000000$	$C_{nr} = -0.048000$	

Table A.5 Control Derivatives

Due to:	Delta Aileron(ζ_A)	Delta Elevator (ζ_E)	Delta Rudder (ζ_R)	Delta Flap (ζ_F)
Z force	$C_{L\zeta_A} = 0.0000$	$C_{L\zeta_E} = 0.4695$	$C_{L\zeta_R} = 0.0000$	$C_{L\zeta_F} = 1.0531$
Y force	$C_{Y\zeta_A} = 0.0025$	$C_{Y\zeta_E} = 0.0000$	$C_{Y\zeta_R} = 0.1017$	$C_{Y\zeta_F} = 0.0000$
l	$C_{l\zeta_A} = -0.2763$	$C_{l\zeta_E} = 0.0000$	$C_{l\zeta_R} = 0.0019$	$C_{l\zeta_F} = 0.0000$
m	$C_{m\zeta_A} = 0.0000$	$C_{m\zeta_E} = -1.0066$	$C_{m\zeta_R} = 0.0000$	$C_{m\zeta_F} = 0.1803$
n	$C_{n\zeta_A} = -0.0011$	$C_{n\zeta_E} = 0.0000$	$C_{n\zeta_R} = -0.0443$	$C_{n\zeta_F} = 0.0000$

A.3.4 Dimensional Stability and Control Derivatives Notation

To keep equations as manageable and understandable as possible, the notation defined in Table A.6 and Table A.7 was used in [1]. The notation represents the stability and control derivatives with their relative scaling factors included during controller design.

Table A.6 Dimensional Stability and Control Derivatives (Forces)

Due to	Lift Forces	Side slip Forces
Angle of Attack (α)	$L_\alpha = qSC_{L\alpha}$	
Side-slip Angle (β)		$Y_\beta = qSC_{y\beta}$
Roll-rate (P)		$Y_P = qSb \frac{b}{2V_a} C_{yP}$
Pitch Rate (Q)	$L_Q = qS \frac{\bar{c}}{2V_a} C_{LQ}$	
Yaw Rate (R)		$Y_R = qSb \frac{b}{2V_a} C_{yR}$
Delta Aileron(ζ_A)		$Y_{\zeta_A} = qSC_{y\zeta_A}$
Delta Elevator (ζ_E)	$L_{\zeta_E} = qSC_{L\zeta_E}$	
Delta Rudder (ζ_R)		$Y_{\zeta_R} = qSC_{y\zeta_R}$

Table A.7 Dimensional Stability and Control Derivatives (Moments)

Due to	Roll Moment	Pitch Moment	Yaw Moment
Angle of Attack (α)		$M_\alpha = qS\bar{c}C_{m_\alpha}$	
Side-slip Angle (β)	$L_\beta = qSbC_{l_\beta}$		$N_\beta = qSbC_{n_\beta}$
Roll-Rate (P)	$L_P = qSb\frac{b}{2V_a}C_{l_p}$		$N_P = qSb\frac{b}{2V_a}C_{n_p}$
Pitch Rate (Q)		$M_Q = qS\bar{c}\frac{\bar{c}}{2V_a}C_{m_Q}$	
Yaw Rate (R)	$L_R = qSb\frac{b}{2V_a}C_{l_R}$		$N_R = qSb\frac{b}{2V_a}C_{n_R}$
Delta Aileron (ζ_A)	$L_{\zeta_A} = qSbC_{l_{\zeta_A}}$		$N_{\zeta_A} = qSbC_{n_{\zeta_A}}$
Delta Elevator (ζ_E)		$M_{\zeta_E} = qS\bar{c}C_{m_{\zeta_E}}$	
Delta Rudder (ζ_R)	$L_{\zeta_R} = qSbC_{l_{\zeta_R}}$		$N_{\zeta_R} = qSbC_{n_{\zeta_R}}$

Appendix B

Attitude Representation

Different methods exist to describe the orientation of a rotating axis system relative to an inertial axis reference frame. In this appendix the Euler 3-2-1 set of rotations is discussed.

B.1 Euler Angles

Consider the inertial axis system described in Section 3.1.1, and define an axis system $F_0(X_0Y_0Z_0)$ that coincides with it. Now define an arbitrary vector $\bar{V} = [x_0 \ y_0 \ z_0]^T$ coordinated in the F_0 axis system. The F_0 axis system is now rotated through three consecutive rotations to align itself with the body axis of an aircraft.

- Rotate the F_0 axis system about the Z_0 -axis by the yaw angle ψ , to create a new axis system $F_1(X_1Y_1Z_1)$. The first transformation from \bar{V}_0 to \bar{V}_1 can be described by

$$\begin{bmatrix} x_1 \\ y_1 \\ z_1 \end{bmatrix} = \begin{bmatrix} \cos \psi & \sin \psi & 0 \\ -\sin \psi & \cos \psi & 0 \\ 0 & 0 & 1 \end{bmatrix} \begin{bmatrix} x_0 \\ y_0 \\ z_0 \end{bmatrix} \quad (\text{B.1})$$

- Rotate the F_1 axis system about the Y_1 -axis by the pitch angle θ , to create a new axis system $F_2(X_2Y_2Z_2)$.

$$\begin{bmatrix} x_2 \\ y_2 \\ z_2 \end{bmatrix} = \begin{bmatrix} \cos \theta & 0 & -\sin \theta \\ 0 & 1 & 0 \\ \sin \theta & 0 & \cos \theta \end{bmatrix} \begin{bmatrix} x_1 \\ y_1 \\ z_1 \end{bmatrix} \quad (\text{B.2})$$

- Rotate the F_2 axis system about the X_2 -axis by the roll angle ϕ , to create a new axis system $F_3(X_3Y_3Z_3)$. The vector \bar{V} , is now coordinated in F_3 , and can be described by $\bar{V}_3 = [x_3 \ y_3 \ z_3]^T$.

$$\begin{bmatrix} x_3 \\ y_3 \\ z_3 \end{bmatrix} = \begin{bmatrix} 1 & 0 & 0 \\ 0 & \cos \phi & \sin \phi \\ 0 & -\sin \phi & \cos \phi \end{bmatrix} \begin{bmatrix} x_2 \\ y_2 \\ z_2 \end{bmatrix} \quad (\text{B.3})$$

The axis system F_3 coincides with the aircraft fixed body axis system F_B . The transformation from Equations (B.1), (B.2) and (B.3) can now be rewritten as

$$\bar{V}_3 = [T_\phi^k \quad T_\theta^j \quad T_\psi^i] \bar{V}_0 \quad (\text{B.4})$$

or equivalently

$$\bar{V}_B = [DCM^{BF}] \bar{V}_F \quad (\text{B.5})$$

The superscript in each transformation matrix element T , in Equation B.4, indicates the axis about which axis system F has been rotated relative to B . The subscript parameterises the rotation. The direction cosine matrix can be written as follows:

$$[DCM^{BF}] = \begin{bmatrix} C_\psi C_\theta & S_\psi C_\theta & -S_\theta \\ C_\psi C_\theta S_\phi - S_\psi C_\phi & S_\psi S_\theta S_\phi + C_\psi C_\phi & C_\theta S_\phi \\ C_\psi C_\theta C_\phi + S_\psi S_\phi & S_\psi S_\theta C_\phi - C_\psi S_\theta & C_\theta C_\phi \end{bmatrix} \quad (\text{B.6})$$

The inverse of the direction cosine matrix can be used to transform a vector coordinated in the body-fixed axis system to the inertial axis system.

BIBLIOGRAPHY

- [1] I.K. Peddle, *Acceleration Based Manoeuvre Flight Control System for Unmanned Aerial Vehicles.*: PhD thesis, Stellenbosch University, 2008, vol. 103.
- [2] Jackie Northam. (2012, August) NPR. [Online].
<http://www.npr.org/2011/07/11/137710942/popularity-of-drones-takes-off-for-many-countries>
- [3] Sharon Weinberger. (2012, May) Popular Mechanics. [Online].
<http://www.popularmechanics.com/technology/military/planes-uavs/darpas-uav-crowd-sourcing-contest#slide-1>
- [4] Draganfly News. (2012, August) Draganfly. [Online].
<http://www.draganfly.com/news/2008/08/24/introduction-to-unmanned-aerial-vehicles-uavs/>
- [5] Andrew Callam. (2012, August) International Affairs Review. [Online]. <http://www.iar-gwu.org/node/144>
- [6] The General Atomics Predator. (2012, August) Vectorsite. [Online].
http://www.vectorsite.net/twuav_07.html
- [7] Jeff Schogol. (2009, April) Stars and Stripes. [Online]. <http://www.stripes.com/news/official-air-force-losing-more-drones-than-army-1.90858>
- [8] Andrew Tarantola. (2012, August) Gizmodo, the Gadget Guide. [Online].
<http://gizmodo.com/5932530/the-x+47b-doesnt-need-a-pilot-to-land-on-an-aircraft-carrier>
- [9] I.K Peddle, *Autonomous Flight of a Model Aircraft.*: Master's dissertation, Stellenbosch University, 2005.
- [10] Jan-Cor Roos, *Autonomous Take-Off and Landing of a FixedWing.*: Master's dissertation, Stellenbosch University, 2006.
- [11] B Visser, *The precision landing of an UAV.*: Master's Dissertation, University of Stellenbosch, 2008.
- [12] R. D. Hart, *Advanced Take-off and Flight Control Algorithms for Fixed Wing Unmanned Aerial Vehicles.*: Master's Dissertation, Stellenbosch University, 2010.
- [13] C Haiyang, W Cao, and Y Chen, *Autopilots for small fixed-wing unmanned air vehicles: a survey.*: IEEE, 2007.
- [14] Leong Woei, *Computer Aided Landing Control System Design For A Fixed Wing UAV.*: Master's dissertation, National Cheng Kung University, 2006.
- [15] K. Senthil Kumar, C. Sudhir Reddy, and J Shanmugam, "Design and Simulation of Blending Function for Landing Phase of a UAV," *Defence Science Journal*, vol. 58, no. 3, pp. 315-

326, May 2008.

- [16] M. I. Lizarraga, *Autonomous Landing System of a UAV.*: Naval Postgraduate School, Monterey California, 2004.
- [17] S Padhi and R Singh, "Automatic Path Planning and Control Design for Autonomous Landing of UAVs using Dynamic Inversion," in *American Control Conference*, St. Louis, MO, USA, 2009, pp. 2409-2414.
- [18] A Cho et al., "Fully Automatic Taxiing, Takeoff and Landing of a UAV only with a Single-Antenna GPS Receiver," in *Proceedings of the 21st International Technical Meeting of the Satellite Division of The Institute of Navigation (ION GNSS 2008)*, Savannah, GA, 2008, pp. 1174 - 1181.
- [19] D Blaauw, *Flight Control System for a Variable Stability Blended-Wing-Body.*: Master's dissertation, Stellenbosch University, 2008.
- [20] R. D. Gaum, *Aggressive Flight Control Techniques for a Fixed-Wing Unmanned Aerial Vehicle.*: Master's dissertation, Stellenbosch University, 2009.
- [21] S Park, *Avionics and Control System Development for Mid-Air Rendezvous of Two Unmanned Aerial Vehicles.*: PhD thesis, Massachusetts Institute of Technology, 2004.
- [22] NASA. (2011, January) Introduction to the Aerodynamics of Flight. [Online]. <http://history.nasa.gov/SP-367/appendc.htm>
- [23] W. H. Pietersen, *System Identification for Fault Tolerant Control of Unmanned Aerial Vehicles.*: Master's dissertation, Stellenbosch University, 2010.
- [24] J.L Meriam and L.G. Kraige, *Engineering mechanics dynamics*, 5th ed.: John Wiley and Sons, 2003.
- [25] P.H. Zipfel, *Modelling and Simulation of Aerospace Vehicle Dynamics.*: AIAA Education Series, 2000.
- [26] B Etkin and L. D. Reid, *Dynamics of Flight, Stability and Control*, 3rd ed.: John Wiley & Sons, 1996.
- [27] J. H. Blakelock, *Automatic Control of Aircraft and Missiles*, 2nd ed. New York: John Wiley & Sons, Inc, 1991.
- [28] Joao P. Hespanha, LQG/LQR controller design notes, 2007.
- [29] W. J. Hough, *Autonomous Aerobatic Flight of a Fixed Wing Unmanned Aerial Vehicle.*: Master's dissertation, Stellenbosch University, 2007.
- [30] Federal Aviation Administration, *Airplane Flying Handbook.*: U.S. Department of Transportation, 2004.
- [31] Jeff Scott. (2003, June) Aerospaceweb. [Online]. <http://www.aerospaceweb.org/question/aerodynamics/q0130.shtml>
- [32] G. D. P. Worthington, *The Private Pilot's Handbook*, 13th ed.: W.J. Flesch & Partners, 1998.
- [33] D. K. Tasoulis, N. M. Adams, and D. J. Hand, "Should Delayed Measurements Always be Incorporated in Filtering?," in *Digital Signal Processing 15th International Conference*, London, United Kingdom, 2007, pp. 264 - 267.

- [34] C Dole and J. E. Lewis, *Flight theory and aerodynamics.*: John Wiley & Sons, 2000.
- [35] G.F. Franklin, J. D. Powell, and M. L. Workman, *Digital Control of Dynamic Systems.*: Addison Wesley Longman, 1998.
- [36] M. V. Cook, *Flight Dynamics Principles.*: Elsevier Butterworth-Heinemann, 1997.
- [37] S. C. Kriel, *A Comparison of Control Systems for the Flight Transition of VTOL.*: Master's dissertation, Stellenbosch University, 2008.
- [38] R. Beard, D. Kingston, M. Quiley , and D. Snyder , "Autonomous Vehicle Technology's for Small Fixed-Wing UAVs," in *AIAA-2003-6559*, vol. II, 2003.
- [39] I.K Peddle, Flight Mechanics Cours Material, 2012.